Plasmonic-organic and silicon-organic hybrid modulators for high-speed signal processing

Zur Erlangung des akademischen Grades eines

DOKTORS DER INGENIEURWISSENSCHAFTEN
(Dr.-Ing.)

von der KIT-Fakultät für
Elektrotechnik und Informationstechnik
des Karlsruher Instituts für Technologie (KIT)

genehmigte

DISSERTATION

von

Sandeep Ummethala, M. Sc.
geboren in
Hyderabad, Indien

Tag der mündlichen Prüfung:	28.01.2021
Hauptreferent:	Prof. Dr.-Ing. Christian Koos
Korreferent:	Prof. Dr.-Ing. Dr. h. c. Wolfgang Freude
	Prof. Dr.-Ing. Thomas Zwick

Table of Contents

Zusammenfassung

Die Photonikindustrie ist einer der schnellst wachsenden Wirtschaftszweige mit einem geschätzten weltweiten Umsatz von 282 Milliarden US-Dollar im Jahr 2018 und einer anhaltenden Wachstumsrate von 7,6 % [1]. Dieses Wachstum wird wesentlich vom Kommunikationssektor vorangetrieben, in dem die Photonik die Schlüsseltechnologie darstellt, mit der man den stetig wachsenden Anforderungen an die Energieeffizienz und Leistungsfähigkeit der Kommunikationsnetzwerke begegnet [2]. Schätzungsweise 77 % des gesamten Datenverkehrs fallen innerhalb der Rechenzentren an [3]. Diese internen Verbindungen verwenden meist direkt modulierte Laser und erreichen dadurch schnell ihre maximale Übertragungskapazität. Eine Möglichkeit weitaus größere Datenraten zu erzielen bieten elektro-optische (EO) Modulatoren, die eine externe Modulation der Laser erlauben. Da in Datenzentren eine hohe Anzahl solcher extern modulierter Laserverbindungen notwendig ist, sind EO-Modulatoren mit niedrigem Energieverbrauch, geringer Größe und niedrigen Herstellungskosten entscheidend.

Photonisch integrierte Schaltungen (engl. photonic integrated circuits, PIC) auf Siliziumbasis erweisen sich als vielversprechende Technologie, um die Bedürfnisse der Kommunikationsindustrie zu erfüllen. Hierbei macht sich die Silizium-Photonik etablierte Fertigungsverfahren elektronischer CMOS-Chips zu Nutze und ermöglicht somit die Herstellung von PICs auf großflächigen Wafern mit geringem Ausschuss. Im Laufe der Jahre wurde von kommerziellen Foundry-Unternehmen ein umfangreiches Portfolio an fortschrittlichen photonischen Bauelementen und standardisierten Prozessdesign-Kits zur Verfügung gestellt. Während bereits eine umfangreiche Bibliothek verlustarmer passiver Bauelemente auf Siliziumbasis verfügbar ist, stellt die Realisierung aktiver Elemente wie Laser oder Modulatoren nach wie vor eine Herausforderung dar. Insbesondere die Realisierung von Modulatoren auf Silizium ist auf Grund des fehlenden linear elektrooptischen Effekts (Pockels-Effekt) problematisch. Hybride Integrationskonzepte, die die jeweiligen

Vorteile von Silizium und zusätzlichen Materialien verbinden, erlauben dennoch schnelle und energieeffiziente EO-Modulatoren.

Diese Arbeit befasst sich mit EO-Hochgeschwindigkeitsmodulatoren, die passive photonische Siliziumkomponenten mit effizienten organischen EO-Materialien kombinieren. Dabei liegt der Fokus auf zwei unterschiedlichen hybriden Integrationskonzepten: den silizium-organischen Hybrid-Modulatoren (SOH-Modulatoren) und den plasmonisch-organischen Hybrid-Modulatoren (POH-Modulatoren). Beide Technologien verwenden organische EO-Materialien für die Modulation, unterscheiden sich jedoch in der Führung des Lichts. In SOH-Modulatoren werden photonische Schlitzwellenleiter verwendet, während die POH-Modulatoren plasmonische Strukturen nutzen. Die Herstellung dieser Bauelemente erfordert spezielle Prozesse, die im Rahmen dieser Arbeit entwickelt wurden.

Kapitel 1 stellt siliziumphotonisch integrierte Schaltkreise vor und diskutiert unterschiedliche hybride Integrationskonzepte.

Kapitel 2 liefert theoretische Hintergründe und erörtert verschiedene Konfigurationen von EO-Modulatoren auf Basis organischer Materialien. Darüber hinaus wird der Herstellungsprozess dieser Modulatoren vorgestellt.

In Kapitel 3 werden die Ultrabreitband-Eigenschaften von POH-Modulatoren mit einer Rekord-Bandbreite von mehr als 360 GHz vorgestellt. Des Weiteren wird die Anwendung solcher breitbandigen EO-Modulatoren in der drahtlosen Terahertz-Kommunikation vorgestellt und erstmals die direkte Umwandlung von Terahertz-Signalen in optische Signale demonstriert. In einer drahtlosen Übertragungsstrecke wurden dabei Datenraten von bis zu 50 Gbit/s erzielt.

In Kapitel 4 wird ein neuartiger Aufbau von POH-Modulatoren vorgestellt, der auf horizontal ausgerichteten plasmonischen Schlitzwellenleitern beruht und dadurch die Anforderungen an die Fertigungstoleranzen stark reduziert. Gezeigt wird ferner, dass die horizontal ausgerichtete Schlitzwellenleiter-Konfiguration von POH-Modulatoren zu einer 25-prozentigen Steigerung der Modulationseffizienz führt.

Kapitel 5 stellt neuartige kapazitiv gekoppelte (engl. capacitivly-coupled) SOH-Modulatoren vor, die große Bandbreiten bieten und gleichzeitig die optischen Verluste gering halten. Durch die Fertigung eines Bauteils mit amorphem Bariumtitanat wird gezeigt, dass die CC-SOH-Modulatoren äußerst effizient sind und eine hohe EO-Bandbreite von 76 GHz aufweisen. Dies ist die höchste Bandbreite die jemals auf der Silizium-Plattform demonstriert wurde. Darüber hinaus wird die Leistungsfähigkeit des CC-SOH-Modulators in optischen Kommunikationsverbindungen gezeigt, indem 4-Zustands-Pulsamplituden-modulierte (PAM4) Signale mit Datenraten von bis zu 200 Gbit/s erzeugt wurden.

Kapitel 6 fasst die Arbeit zusammen und gibt einen Ausblick auf weitere mögliche Verbesserungen der Leistungsfähigkeit der Hochgeschwindigkeits-EO-Modulatoren.

Preface

The photonic industry is one of the fast growing industrial sectors with an estimated global revenue of $282 billion in 2018 and a persistent growth rate of 7.6 % [1]. A substantial part of this growth is driven by the optical communication industry where photonics is a key enabling technology to meet the energy efficiency demands, and the ever-growing capacity challenges of optical networks [2]. With an estimated 77 % [3] of the total data center traffic accounting to within the data center, current optical links with directly modulated lasers are soon reaching their maximum capacity. These links must be replaced with high-capacity networks relying on lasers that are externally modulated using high-speed electro-optic (EO) modulators. In order to deploy hundreds and thousands of such externally modulated laser links in a data centre, it is imperative that the EO modulators should feature low energy consumption as well as small footprint thus allowing low-cost high-density integration.

Photonic integrated circuits (PIC) in silicon emerged as a promising technology to fulfil the demands of the communication industry. Silicon photonics exploits highly mature complementary metal-oxide-semiconductor (CMOS) fabrication processes and offers PICs that can be realized with high yield on large-area wafers. Over the years, a rich portfolio of advanced photonic devices were made available by commercial foundry services together with well-developed process design kits. While an extensive library of low-loss passive elements are currently available in the silicon photonic platform, challenges still remain to be addressed in bringing active elements such as lasers and modulators to the silicon photonics platform. The absence of linear electro-optic effect (Pockels effect) in silicon forced the researchers towards hybrid integration concepts, which combine the complementary strengths of different material systems, to realize high-speed and energy-efficient EO modulators.

In this work, we rely on a hybrid integration platform that combines passive silicon photonic components with efficient organic EO materials to realize high-speed EO modulators. This thesis is focused on two different hybrid integration concepts – the silicon-organic hybrid (SOH) modulators and the plasmonic-organic hybrid (POH) modulators. While both technologies use organic

EO materials for modulation, the SOH modulators confine light using silicon photonic slot waveguides whereas the POH modulators use plasmonic structures for light confinement. The fabrication of these devices required dedicated processes which are developed in the framework of this thesis. The structure of this thesis is summarized as follows:

Chapter 1 introduces silicon photonic integrated circuits and discusses different hybrid integrated platforms.

Chapter 2 provides a brief theoretical background and presents different configurations of EO modulators based on organic materials. Further, the fabrication processes of these modulators is also presented.

Chapter 3 presents the ultra-broadband characteristics of POH modulators with a record-high bandwidth of more than 360 GHz. We highlight the application of such broadband EO modulators in THz wireless communications with the very first demonstration of direct terahertz-to-optical conversion of wireless signals on a carrier at 0.288 THz.

Chapter 4 presents a novel architecture of POH modulators relying on horizontal plasmonic slot waveguides, which greatly relaxes the required fabrication tolerances of POH modulators. We further show that the horizontal-slot configuration of POH modulators results in a 25 % increase in the modulation efficiency.

Chapter 5 presents a novel architecture of capacitively-coupled SOH (CC-SOH) modulators that offer large bandwidths while keeping the optical losses low. Using a proof-of-concept device with amorphous $BaTiO_3$, we show that the CC-SOH modulators are very efficient and feature a record-high EO bandwidth of 76 GHz that has ever been demonstrated in a silicon photonic platform. Furthermore, we show the viability of the CC-SOH modulator in optical communication links by generating 4-state pulse amplitude modulated (PAM4) signals with data rates up to 200 Gbit/s.

Chapter 6 summarizes the work of this thesis and provides an outlook for further improvements in the performance parameters of high-speed EO modulators.

Achievements of the present work

In this doctoral thesis, novel electro-optic (EO) modulators are investigated with the goal to realize a large EO bandwidth as well as high efficiency. The EO modulators rely on organic electro-optic (OEO) materials to achieve efficient EO modulation. Two different device concepts – plasmonic-organic hybrid (POH) and capacitively-coupled silicon-organic hybrid (CC-SOH) – are pursued in this thesis to realize modulators that are capable of high-speed modulation. Furthermore, the applicability of ultra-broadband POH modulators for direct terahertz-to-optical conversion of data signals in a THz wireless communication link is investigated. Such implementations allow to greatly simplify the receiver systems for future wireless communication links.

Apart from the development of dedicated fabrication processes for realizing these high-speed EO modulators, the scientific achievements of this work are summarized as follows:

First demonstration of an electro-optic modulator with a 3dB bandwidth extending into the THz spectrum: We demonstrate that a compact POH modulators with a footprint of about 600 μm^2 has an ultra-wide modulation bandwidth with a flat frequency response of more than 0.36 THz. This work has been published in Nature Photonics [J3].

First demonstration of a THz link that is seamlessly integrated into a fibre-optic network using direct THz-to-optical (T/O) conversion at the wireless receiver: Using an ultra-broadband POH modulator, we show that a THz communication link can be seamlessly integrated into a fiber-optic network by directly modulating the THz data signals onto an optical carrier at the wireless receiver. In a proof-of-principle demonstration, we transmitted data signals up to 50 Gbit/s on a 0.288 THz carrier over a distance of 16 m and converted the data signals directly into the optical domain using POH modulator. This result is also part of the previously mentioned publication in Nature Photonics [J3].

Demonstration of horizontal-slot POH modulator: We propose and demonstrate POH modulators with horizontal plasmonic slot waveguides to improve

the π-voltage-loss product of POH modulators. Using a proof-of-concept device, we show that the π-voltage-loss product of horizontal-slot POH modulators can be improved by 25 % in comparison to conventional vertical-slot POH modulators [C1].

First demonstration of a capacitively-coupled SOH (CC-SOH) modulator, offering the largest 3dB bandwidth so far achieved by a silicon photonic modulator: We propose a CC-SOH modulator relying on a high-k radio frequency (RF) slotline that can overcome the bandwidth limitations of conventional resistively-coupled SOH devices. In a proof-of-concept experiment, we show that a CC-SOH modulator using $BaTiO_3$ features a 3dB EO bandwidth beyond 75 GHz, the largest bandwidth so far achieved with silicon photonic modulators based on dielectric waveguides. This work has been published in Optica [J1].

First demonstration of four-state pulse amplitude modulation (PAM4) signals generated with a modulator on the silicon photonic platform at data rates of 200 Gbit/s: We prove the capability of the novel CC-SOH modulators by generating the PAM4 signals with data rates up to 200 Gbit/s which were at the time the highest data rate that is demonstrated with silicon photonic modulators. This result is also part of the previously mentioned publication in Optica [J1].

1 Introduction

Communication with light has come a long way from the centuries old light beacon systems to today's complex network of submarine optical communication systems that juggle a few terabits/s between the continents. With the advent of cloud-based services, content streaming and the internet of things (IoT), the number of devices connected to the communication networks would reach 3 times the global population by 2022 [2]. It is estimated that the global internet traffic is rising by 26 % every year [2] with a large fraction of data that is processed within the data centers. To sustain this explosive growth in data rates, the capacity of short-reach optical links needs to be increased while reducing their energy consumption. A key component of an optical communication link is an electro-optic (EO) modulator that converts the information from the electrical to the optical domain by controlling either one or more physical properties of light – the intensity, the phase, or the polarization. EO modulators based on lithium niobate ($LiNbO_3$) [4] has long been the workhorse of optical communication systems. But they are rather bulky and are not well suited for short-reach links where integration density, size and power consumption are crucial parameters. Since the inception in early 90's, photonic integrated circuit (PIC) [5] technology has considerably matured, providing advanced photonic functionalities on a compact chip with an exponential increase in their integration density [6].

A plethora of material platforms have been investigated to realize photonic integrated circuits – polymers, silica-on-silicon, indium phosphide (InP), and silicon to name a few. Of these, the semiconductor material platforms stand out as they leverage on the well-developed semiconductor processing technology from the electronic IC industry and also provide to a path for compact photonic circuits (owing to a high index contrast between the waveguide core and the cladding). InP has a dominating presence in the PIC market due to the broad portfolio of functional elements such as laser diodes, semiconductor optical amplifiers, photodetectors, electro-absorption modulators and electro-optic modulators [7]. However, the early InP technology relied on expensive fabrication processes that are limited to relatively small wafer sizes (< 75 mm) hence

resulting in high manufacturing cost and low-throughput [8]. Despite the recent advantages in cost and performance made possible with the availability of 150 mm InP wafers, many optical equipment vendors find the silicon photonic platform more attractive [9]. This is because of the ability to leverage the ecosystem of advanced CMOS foundries to produce low-cost, high-volume PICs, thereby facilitating a quick market entry [9]. An additional advantage of silicon photonics is the possibility for seamless co-integration of electronic controllers and drivers on a photonic integrated circuit, leading to co-integration of electronic and photonic circuits on the same die [10]. A recent demonstration of such technologies has gained much attention [11].

One of the key elements of a PIC transmitter is an optical modulator that provides an interface between the electrical and the optical circuits. An attractive approach for optical modulators is based on the Pockels effect that provides pure phase modulation with large electro-optic (EO) bandwidths. However, the Pockels effect is absent in bulk silicon due to inversion symmetry of the underlying crystal lattice. Instead, state-of-the-art all-silicon modulators rely on the plasma-dispersion effect [12] where the refractive-index of silicon is modulated through a change in the carrier density. Although some silicon depletion-type modulators [13] have been demonstrated with reasonably large EO bandwidths of 48 GHz, the weak plasma-dispersion effect leads to cm-scale device lengths making it difficult to achieve high integration density. Furthermore, a carrier-induced refractive index modulation is associated with a change in optical loss [14] and poses a challenge for implementation of complex modulation formats. A way to circumvent this problem is to bring the Pockels effect onto silicon through a hybrid integration. A recent breakthrough in bonding and nano-structuring lithium niobate (LN) thin films [15], [16] on oxidized silicon wafers led to the demonstration of modulators with EO bandwidths up to 100 GHz [17] on the lithium niobate on insulator (LNOI) platform [18], [19]. However, due to the weak EO activity of lithium niobate (r_{33} ~ 30 pm/V), the modulator lengths typically range in the order of a few centimeters. An alternative material for hybrid integration on silicon is crystalline $BaTiO_3$ (barium titanate, BTO) [20]–[22] offering very attractive EO coefficients (r_{42} ~ 920 pm/V) [23]. However, the bandwidth of these devices is rather small and so far limited to only 20 GHz

[24]. It is to be noted that the hybrid platforms with LN and BTO involve technologically demanding processes for bonding, integration, and etching, which are not part of commercial CMOS foundries.

An alternative approach to realize efficient EO modulators on silicon is to combine passive silicon photonic circuits with organic EO (OEO) materials. With a theory-based design and targeted chemical synthesis, OEO materials can be synthesized to maximize their EO activity while being resilient against harsh environmental conditions [25]. An additional advantage is the ease of processing where the OEO materials can be spin-coated, dispensed, or printed in a back-end-of-line post-processing step, and are thus compatible with any platform of photonic integrated circuits. By combining low-loss silicon slot waveguides with efficient organic materials having large EO coefficients (r_{33} ~ 390 pm/V), the so-called silicon-organic hybrid (SOH) modulators were demonstrated with ultra-low voltage-length products down to 0.32 V mm [26] and EO bandwidths up to 100 GHz [27]. The SOH concept thus opens a path towards compact devices with sub-1mm device lengths and sub-1 V operation voltages [28], [29] that can be directly driven by highly scalable CMOS circuits without the need for a separate electrical amplifier [30]. However, without a supporting gate voltage [27], the EO bandwidth of highly efficient slot-waveguide SOH modulators is limited to, e.g., 25 GHz or less [31]. This is due to the intrinsic *RC* time constant associated with the capacitance of the slot and the resistance of the adjacent silicon (Si) slabs [32] of conventional resistively-coupled SOH (RC-SOH) modulators. In order to avoid this bandwidth limitation, the Si slot waveguides can be replaced by metal-insulator-metal (or plasmonic slot) waveguides in the so-called plasmonic-organic hybrid (POH) technology [33]–[36]. Owing to the high conductivity of the metals, the theoretical bandwidth of POH modulators is expected to extend up to 1 THz [36]. However, the high optical absorption of metals results in a rather large insertion loss of POH modulators. In order to achieve a large EO bandwidth as well as a small insertion loss simultaneously, the resistive slabs of a conventional RC-SOH modulator can be replaced by a high-k dielectric material, resulting in a capacitively-coupled SOH (CC-SOH) modulator.

This thesis investigates two novel device concepts and architectures to overcome the bandwidth limitation of conventional RC-SOH modulators – POH and

CC-SOH. Chapter 2 presents the theoretical background of electro-optic Mach-Zehnder modulators (MZM) and provides insights into the bandwidth limitation of RC-SOH modulators. Furthermore, the concepts of plasmonic-organic hybrid (POH) modulators and capacitively-coupled SOH (CC-SOH) modulators are introduced along with insights into the fabrication processes of these modulators. In Chapter 3, we experimentally verify the broadband characteristics of POH MZM and show that the EO modulation bandwidth of these modulators extends beyond 360 GHz. Leveraging the broadband nature of the POH modulators, we perform proof-of-principle experiments that seamlessly integrate a wireless THz communication link into a fiber-optic network. This experiment highlights the very first demonstration of terahertz-to-optical (T/O) conversion of wireless signals on a 0.288 THz carrier. In this demonstration, data rates up to 50 Gbit/s were reached. In Chapter 4, a novel architecture of POH modulators with horizontal plasmonic slot waveguides is presented. We show that these horizontal-slot POH (HS-POH) modulators are robust to fabrication tolerances and offer larger modulation efficiencies in comparison with their counterparts with vertical plasmonic slot waveguides. Through experiments, we demonstrate a 25 % improvement in the modulation efficiency of POH modulators by adopting horizontal plasmonic slot waveguides. Chapter 5 presents the novel concept of CC-SOH modulators, in which the doped silicon slabs of RC-SOH modulators are replaced with a material having large relative permittivity (high-k dielectric). Using a proof-of-concept device with amorphous $BaTiO_3$, we show that the CC-SOH modulator has a very small π-voltage-length product of 1.3 V mm with a 3dB EO bandwidth of 76 GHz. This demonstration corresponds to the highest bandwidth so far achieved with a silicon photonic modulators, without employing plasmonic structures. Based on simulations, we estimate that the EO bandwidth of an optimized CC-SOH modulator can extend far beyond 100 GHz. Furthermore, we show the viability of the CC-SOH modulator in optical communication links by generating signals with data rates up to 200 Gbit/s. The work presented in this thesis demonstrates the enormous potential of high-speed EO modulators for application in optical communications, optical metrology, ultra-fast signal processing and in disruptive technologies such as THz communications.

2 Electro-optic modulators for high-speed signal processing

This chapter covers the theoretical and the technological background related to the work presented in this thesis. Section 2.1 begins with fundamentals of the Pockels effect and presents theoretical background of electro-optic (EO) Mach-Zehnder modulators and digital modulation techniques used in modern communication systems. Section 2.2 introduces various configurations of hybrid modulators using OEO materials along with their bandwidth limitations. Finally, Section 2.3 gives some insights into the fabrication techniques developed for realizing high-speed EO modulators.

2.1 Theoretical background

Electro-optic (EO) modulators rely on the Pockels effect that influences the refractive index of a second-order nonlinear material. This section presents the fundamentals of nonlinear electric polarization and the Pockels effect, followed by the principle of a Mach-Zehnder modulator. Towards the end of this section, a brief introduction to the modulation formats used in digital communication systems is presented.

2.1.1 Nonlinear electric polarization

An externally applied electric field $\vec{E}$ induces a polarization $\vec{P}$ in a dielectric medium by altering its dipole moment. The overall polarization of the medium is given by

$$\vec{P} = \vec{P}^{(1)} + \vec{P}^{(2)} + \vec{P}^{(3)} + ..., \tag{2.1}$$

where $\vec{P}^{(1)}$ denotes the linear polarization that depends linearly on the electric field, while $\vec{P}^{(2)}$ and $\vec{P}^{(3)}$ represent the second-order and third-order contributions of the electric field, respectively. In the following, we limit the description until the second-order polarization only.

Assuming a dielectric material which is time-invariant, local in space, and homogenous, the time-dependent vector components $i \in \{x, y, z\}$ of the electric polarization $\vec{P}$ can be expanded in a Volterra series of the applied electric field $\vec{E}$,

$$\begin{aligned} P_i(t) &= \varepsilon_0 \int_{-\infty}^{+\infty} \chi_{ij}^{(1)}(\tau_1) E_j(t-\tau_1) \mathrm{d}\tau_1 \\ &+ \varepsilon_0 \int_{-\infty}^{+\infty} \int_{-\infty}^{+\infty} \chi_{ijk}^{(2)}(\tau_1, \tau_2) E_j(t-\tau_1) E_k(t-\tau_2) \mathrm{d}\tau_1 \mathrm{d}\tau_2, \end{aligned} \tag{2.2}$$

where ε_0 is the vacuum permittivity, $\tau_{1,2}$ are time integration variables. The Volterra kernels $\chi_{ij}^{(1)}$ and $\chi_{ijk}^{(2)}$ with $i, j, k \in \{x, y, z\}$ represent the linear and the second-order nonlinear response functions with tensor ranks of 2 and 3, respectively. Since the polarization response of the medium is causal, the tensor component $\chi^{(n)} = 0$ for $(\tau_1, \tau_2) < 0$. The second-order polarization of Eq. (2.2) can also be expressed in short-form notation as

$$\vec{P}^2(t) = \varepsilon_0 \int_{-\infty}^{+\infty} \int_{-\infty}^{+\infty} \chi^{(2)}(\tau_1, \tau_2) : \vec{E}(t-\tau_1) \vec{E}(t-\tau_2) \mathrm{d}\tau_1 \mathrm{d}\tau_2, \tag{2.3}$$

where the double multiplication sign ":" indicates component-by-component multiplication. The electric field $\vec{E}$ can be expressed as a superposition of L different monochromatic waves ω_l and their corresponding complex time domain amplitudes $\underline{\vec{E}}(\omega_l)$ as

$$\vec{E}(t) = \frac{1}{2} \sum_{l=-L}^{L} (1 + \delta_{l0}) \underline{\vec{E}}(\omega_l) e^{\mathrm{j}\omega_l t}, \tag{2.4}$$

where δ_{ij} is the Kronecker delta defined by

$$\delta_{ij} = \begin{cases} 1 \text{ for } i = j \\ 0 \text{ for } i \neq j \end{cases}. \tag{2.5}$$

Note that the fore factor $(1 + \delta_{l0})$ is introduced to avoid a situation in which a zero-frequency (DC) electric field is associated with an amplitude of $\underline{\vec{E}}(\omega_0) / 2$.

By substituting Eq. (2.4) in Eq. (2.3), we find that the second-order polarization is given by

$$\vec{P}^{(2)}(t) = \frac{1}{4}\epsilon_0 \sum_{l_1,l_2=-L}^{L} (1+\delta_{l_1 0})(1+\delta_{l_2 0})\chi^{(2)}(\omega_\Sigma : \omega_{l_1}, \omega_{l_2}) : \underline{\vec{E}}(\omega_{l_1})\underline{\vec{E}}(\omega_{l_2})\mathrm{e}^{\mathrm{j}(\omega_{l_1}+\omega_{l_2})t}, \tag{2.6}$$

where $\chi^{(2)}(\omega_\Sigma : \omega_{l_1}, \omega_{l_2})$ corresponds to the two-dimensional Fourier transform of $\chi^{(2)}(\tau_1, \tau_2)$ given by

$$\chi^{(2)}(\omega_\Sigma : \omega_{l_1}, \omega_{l_2}) = \int_{-\infty}^{\infty}\int_{-\infty}^{\infty} \chi^{(2)}(\tau_1, \tau_2)\mathrm{e}^{-\mathrm{j}\omega_{l_1}\tau_1}\mathrm{e}^{-\mathrm{j}\omega_{l_2}\tau_2}\mathrm{d}\tau_1\mathrm{d}\tau_2. \tag{2.7}$$

In this relation, the argument $\omega_\Sigma = \omega_{l_1} + \omega_{l_2}$ denoted the sum frequency generated by nonlinear interaction of monochromatic waves at ω_{l_1} and ω_{l_2}. Similar to Eq. (2.4), the electric polarization $\vec{P}^{(2)}$ can also be expressed as a sum of M monochromatic waves with various sum frequencies $\omega_p = \omega_\Sigma$ and corresponding complex time-domain amplitudes $\underline{\vec{P}}(\omega_m)$ as

$$\vec{P}(t) = \frac{1}{2}\sum_{p=-M}^{M} (1+\delta_{p0})\underline{\vec{P}}(\omega_p)e^{\mathrm{j}\omega_p t}. \tag{2.8}$$

From Eqs. (2.6) and (2.8), the complex time-domain amplitudes for which the sum frequencies corresponds to ω_p is given by

$$\underline{\vec{P}}^{(2)}(\omega_p) = \frac{1}{2}\epsilon_0 \sum_{\mathbb{S}(\omega_p)} \frac{(1+\delta_{l_1 0})(1+\delta_{l_2 0})}{(1+\delta_{p0})}\chi^{(2)}(\omega_p : \omega_{l_1}, \omega_{l_2}) : \underline{\vec{E}}(\omega_{l_1})\underline{\vec{E}}(\omega_{l_2}), \tag{2.9}$$

where the quantity $\mathbb{S}(\omega_p)$ indicates a summation over all permutations of frequencies $\omega_{l_1}, \omega_{l_2}$ which amount in sum to ω_p.

2.1.1.1 Pockels effect

The Pockels effect is a second-order nonlinear process that occurs in materials that lack inversion symmetry. It describes the linear modulation of the refractive index by an applied electric field that is used to modulate the phase of an optical

carrier at frequency ω_c. The applied electric field may be static or slowly varying with a modulation frequency $\omega_m \ll \omega_c$ such that we can assume $\omega_m = 0$ in this quasi-static case. In such a case, the Eq. (2.9) can be simplified as

$$\underline{\vec{P}}^{(2)}(\omega_c) = 2\epsilon_0 \chi^{(2)}(\omega_c : \omega_c, \omega_m) : \underline{\vec{E}}(\omega_c)\underline{\vec{E}}(\omega_m), \tag{2.10}$$

with the vectorial components given by

$$\underline{P}_i^{(2)}(\omega_c) = 2\epsilon_0 \chi_{ijk}^{(2)}(\omega_c : \omega_c, \omega_m)\underline{E}_j(\omega_c)\underline{E}_k(\omega_m), \tag{2.11}$$

By describing the electric displacement field $\vec{D}(t) = \epsilon_0 \vec{E}(t) + \vec{P}(t)$ as a superposition of monochromatic waves with complex amplitudes, we find that

$$\begin{aligned} \underline{D}_i(\omega_c) = \varepsilon_0 \Big(\delta_{ij} + \chi_{ij}{}^{(1)}(\omega_c) \Big) \underline{E}_j(\omega_c) \\ + 2\varepsilon_0 \chi_{ijk}^{(2)}(\omega_c : \omega_c, \omega_m)\underline{E}_j(\omega_0)\underline{E}_k(\omega_m), \end{aligned} \tag{2.12}$$

where δ_{ij} is the Kronecker delta as defined in Eq. (2.5). From Eq. (2.12), the radio-frequency (RF) dependent optical permittivity can be expressed as

$$\varepsilon_{ij} = \varepsilon_0 \Big(\delta_{ij} + \chi_{ij}^{(1)} + 2\chi_{ijk}^{(2)} \underline{E}_k(\omega_m) \Big). \tag{2.13}$$

Historically, the Pockels effect is described in terms of the impermeability tensor η_{ij}, which is defined as the inverse of the permittivity $\eta_{ij} = \epsilon_{ij}^{-1}$. Assuming that the optical carrier ω_c is far away from the material resonances, then ϵ_{ij} is real and symmetric [37]. Limiting to the second-order nonlinearity, the impermeability tensor can be expressed in the strength of the low-frequency electric field $\underline{E}_k(\omega_m)$ as

$$\eta_{ij} = \eta_{ij}{}^{(0)} + r_{ijk}(\omega_c)\underline{E}_k(\omega_m), \tag{2.14}$$

where $\eta_{ij}{}^{(0)}$ is the case when no external electric field is applied, and r_{ijk} is the EO tensor, which is used to quantify the strength of the nonlinearity of a Pockels-type material. The EO tensor r_{ijk} and the second-order susceptibility tensor $\chi_{ijk}^{(2)}$ is given by

$$\chi_{ijk}^{(2)}(\omega_c : \omega_c, \omega_m) = -\frac{1}{2} n_i^2(\omega_c) n_j^2(\omega_c) r_{ijk}(\omega_c), \tag{2.15}$$

where n_i and n_j denote the refractive indices along the principal axes of the indicatrix for the case when no external electric field is applied. Since η_{ij} is real and symmetric, it follows that r_{ijk} is thus symmetric in its first two indices. The third-rank EO tensor r_{ijk} can therefore be represented as a two-dimensional matrix r_{hk} using a contracted notation [37],

$$h = \begin{cases} 1 \text{ for } ij = 11 \\ 2 \text{ for } ij = 22 \\ 3 \text{ for } ij = 33 \\ 4 \text{ for } ij = 23 \text{ or } 32 \\ 5 \text{ for } ij = 13 \text{ or } 31 \\ 6 \text{ for } ij = 12 \text{ or } 21 \end{cases} \tag{2.16}$$

Although the EO tensor has 18 components, some of r_{hk} are restricted by any rotational symmetry properties that the medium may possess [37]. In most practical cases, e.g., for lithium niobate and OEO materials, a single element of the EO tensor dominates. In such cases, this direction can be chosen to be along the 3 axis, such that the component r_{33} of the EO tensor dominates. The induced change in refractive index along the main principal axis of the optical indicatrix is then given by

$$\Delta n_3(\omega_c) = -\frac{1}{2} n_3^3 r_{33}(\omega_c) \underline{E}_3(\omega_m). \tag{2.17}$$

2.1.2 Mach-Zehnder modulator (MZM)

To take advantage of the dominant EO coefficient r_{33} of most materials, both the modulating field E_m and the optical field are oriented along the *z*-axis. The change in the refractive index is therefore given by

$$\Delta n = \frac{1}{2} n^3 r_{33} E_m. \tag{2.18}$$

The phase shift φ experienced by the optical carrier while traversing a modulator of length L is given by

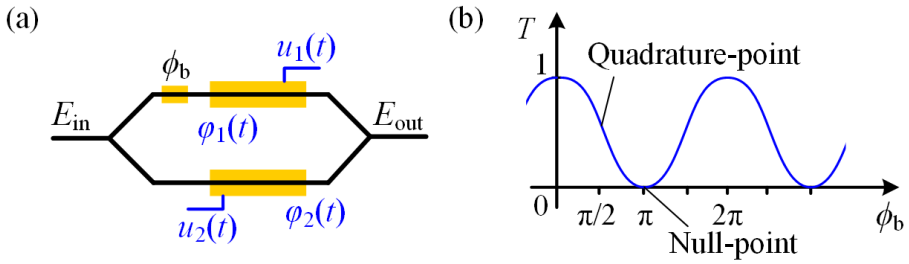

Figure 2.1: Schematic and characteristics of an electro-optic Mach-Zehnder modulator (MZM). **(a)** Schematic of a MZM where the incoming light E_{in} is split in two arms, each of which contains a phase modulator. The top MZM arm has an additional bias phase ϕ_b that defines the operating point of the MZM by adjusting the relative phase difference between the two MZM arms. Two RF modulating signals $u_1(t)$ and $u_2(t)$ in the upper and lower arm of the MZM result in a modulation of $\varphi_1(t)$ and $\varphi_2(t)$, respectively. After modulation, the light from the two arms is coherently combined at the output E_{out} of the MZM. **(b)** Intensity transfer function T of a push-pull MZM as a function of the relative bias phase ϕ_b between the phase modulating arms. A relative phase difference $\phi_b = \pi/2$ results in a quadrature operating point of the MZM, where the intensity modulation varies linearly for a small RF modulation signal. For $\phi_b = \pi$, the MZM is said to be operating at the its null-point where the optical carrier is suppressed.

$$\varphi = -\Delta n k_0 L = \frac{1}{2} n^3 r_{33} E_m k_0 L, \tag{2.19}$$

where $k_0 = 2\pi/\lambda_0$ is the vacuum wavenumber and λ_0 is the vacuum wavelength of the optical carrier. The phase modulation of the optical carrier can be transformed into an intensity modulation by using an interferometric waveguide structure such as a Mach-Zehnder interferometer, resulting in the so-called Mach-Zehnder modulator (MZM).

A schematic representation of an MZM is depicted in Fig. 2.1(a) where an optical carrier with the complex electric field $E_{in}(t)$ is fed to the input. The carrier is split into two arms with each arm featuring a phase modulator. A bias phase shift ϕ_b is introduced in one of the arms which allows for adjustment of the operating point of the MZM. An RF voltage $u_{1,2}(t)$ applied to each phase modulator produces a phase shift $\varphi_{1,2}(t)$ of the optical carrier that is proportional to the applied voltage. Assuming that the splitters/combiners do not introduce any phase shift, the interference signal at the output of the MZM is given by

$$E_{out}(t) = \frac{1}{2} E_{in}(t)\left(e^{j\varphi_1(t)} + e^{j\varphi_2(t)+j\phi_b}\right). \tag{2.20}$$

Such an operation of the MZM, in which the individual phase shifters in the two arms can be driven independently, is called a dual-drive operation. The MZM is said to be operated in push-push mode when both the phase shifters induce an equal phase shift, $\varphi_1 = \varphi_2 = \varphi$, thereby modulating only the phase of the output signal. A push-pull operation is obtained when the phase shifts induced in both arms is equal but have an opposite sign, i.e., $\varphi_1 = -\varphi_2 = \varphi$. The electric field transfer function of a push-pull MZM is given by

$$\frac{E_{\text{out}}}{E_{\text{in}}} = \frac{1}{2}\left(e^{\mathrm{j}\varphi(t)} + e^{-\mathrm{j}\varphi(t)+\mathrm{j}\phi_{\text{b}}}\right) = e^{\mathrm{j}\phi_{\text{b}}/2}\cos\left(\varphi(t) - \frac{\phi_{\text{b}}}{2}\right). \tag{2.21}$$

The MZM is said to be balanced when both the arms have the same length such that there is no bias phase shift between the MZM arms, i.e., $\phi_{\text{b}} = 0$. For a different lengths of the MZM arms, i.e., $\phi_{\text{b}} \neq 0$, the MZM is unbalanced and the intensity transfer function, see Fig. 2.1(b), of a push-pull MZM is given by,

$$T = \left|\frac{E_{\text{out}}}{E_{\text{in}}}\right|^2 = \frac{1}{2}(1+\cos\Delta\theta), \quad \Delta\theta = 2\varphi(t) + \phi_{\text{b}}. \tag{2.22}$$

The bias phase shift ϕ_{b} determines the operating point of the unbalanced MZM. For $\phi_{\text{b}} = \pi/2$, i.e., for the so-called quadrature-point, the output of the MZM results in a linear intensity modulation when driven by an RF signal with small amplitude. In order to supress the optical carrier, the MZM is set for operation at its null-point where $\phi_{\text{b}} = \pi$. The π-voltage U_π of a push-pull MZM is defined as the drive voltage required to achieve a relative phase difference of π between the two arms of the MZM, thus driving the intensity transfer function from its maximum value to the minimum.

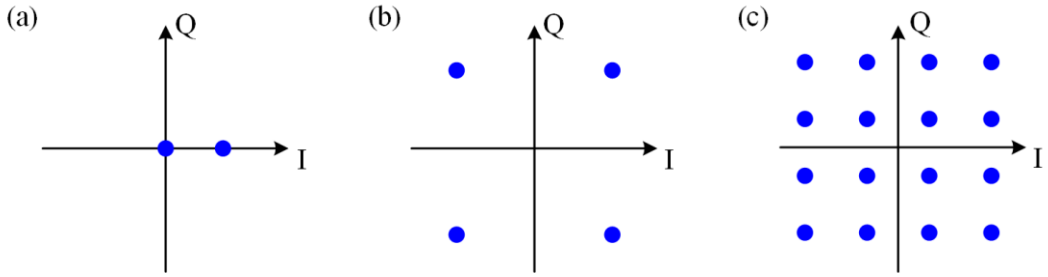

Figure 2.2: Exemplary constellation diagrams for advanced digital modulation formats. **(a)** Constellation diagram for on-off keying (OOK) modulation format showing two states of carrier intensity. **(b)** For a quadrature phase shift keying (QPSK) format, both the in-phase (I) and the quadrature-phase (Q) components are modulated with a binary signal and hence allows to transmit 2 bits/symbol. **(c)** Constellation diagram of 16-state quadrature amplitude modulation (16QAM) format that allows transmission of 4 bits/symbol.

2.1.3 Digital communications

In digital communication systems, the information is encoded into a sequence of binary digits where a logical "0" is represented by "low" intensity signal (symbol) of light or "light off" and a logical "1" corresponds to a "high" intensity signal of light or "light on". However, to make efficient use of the available spectrum, quadrature amplitude modulation (QAM) formats are used where each symbol transmits more than one bit [38]. This is possible using two MZMs nested in a Mach-Zehnder interferometer, the so-called in-phase and quadrature-phase (IQ) modulator, which can address arbitrary phase and amplitude states in a complex plane. Using an IQ modulator, the binary information is mapped to one of M symbols. Each symbol can be represented in complex notation as $\underline{b}_k = b_{k,\mathrm{I}} + \mathrm{j}b_{k,\mathrm{Q}}$, where $k = 1,2,3...M$. The carrier then transports $\log_2 M$ bits of information. The rate at which the symbols are transmitted is called the symbol rate R_s, also referred to as symbol rate or *Baud* (Bd). The number of bits transmitted per second, R_b, is connected to the symbol rate and is given by $R_\mathrm{b} = R_\mathrm{s} \log_2 M$. The in-phase component $b_{k,\mathrm{I}}$ and the quadrature-phase component $b_{k,\mathrm{Q}}$ of each symbol can be represented graphically in the complex plane in a so-called constellation diagram, see Fig. 2.2. In the simplest case of on-off keying (OOK) as shown in Fig. 2.2(a), the amplitude of the optical carrier has two allowed states. This modulation format is also called two-level pulse amplitude modulation (PAM2) and carries 1 bit per symbol. The

number of bits can be increased by using more amplitude levels, for example, a four-level pulse amplitude modulation (PAM4) signal contains four amplitude levels and hence carries 2 bits per symbol. However, the noise tolerance is reduced as the number of amplitude levels is increased. The OOK and PAM4 formats are prominent for short-reach communication links as the intensity-encoded information is recovered using a simple photodiode and hence keeps the receiver architecture simple. The number of transmitted bits per symbol can be increased by using more advanced modulation formats where information is encoded onto both the in-phase and the quadrature-phase components of the carrier. Quadrature phase shift keying (QPSK), also called 4-state quadrature amplitude modulation (4QAM) is the most basic modulation format using I and Q components of the carrier. As shown in Fig. 2.2(b), QPSK modulation allows a transmission of 2 bits per symbol. The most common way of generating a QPSK signal is by driving an IQ modulator with two streams of binary signals. By using multi-level drive signals for the I and Q components of the IQ modulator, higher-order QAM signals such as 16QAM, see Fig. 2.2(c), or 64QAM can be generated.

In a digital communication system, the received data stream is influenced due to various phenomena such as noise, interference, dispersion, or other distortions. A measure of the transmission performance of a digital communication system is bit error probability or bit error ratio (BER), a dimensionless quantity. BER is the ratio of number of bit errors to the total number of bits transmitted during a particular interval of time. A BER of 10^{-6} states that the transmission has a probability of 1 bit error per 1 million transmitted bits.

2.2 Silicon photonic modulators based on organic EO materials

The silicon-on-insulator (SOI) platform has gained prominence over the past years due to the mature semiconductor fabrication technology, and because it offers the possibility to co-integrate electronic and photonic circuits. Although a large library of photonic building blocks are currently available, the silicon photonic platform lacks efficient electro-optic modulators. This is because of the absence of the linear Pockels effect in silicon owing to its centro-symmetric

crystal structure. To overcome these limitations, state-of-the-art silicon photonic modulators [39] rely on plasma-dispersion effect [40] in a reverse-biased *pn*-junction integrated into in a silicon strip waveguide. A modulating electric field applied across the *pn*-junction changes the width of the depletion region. Due to the change in the density of the free carriers in the depletion region, the refractive index is altered, thereby resulting in a phase modulation of the optical carrier. However, the plasma-dispersion effect is weak, and the modulators relying on this effect have modulator lengths up to a few centimetres [13], making their on-chip integration expensive. An efficient way to overcome these limitations is to combine passive silicon slot waveguides or plasmonic slot waveguides with organic electro-optic materials [41], in a silicon-organic hybrid (SOH) or plasmonic-organic hybrid (POH) integration respectively [36], [42]. EO modulators based on the integration of ultra-efficient organic EO materials into passive waveguiding structures open a path for compact, high-speed devices.

2.2.1 Resistively-coupled silicon-organic hybrid (RC-SOH) modulator

Over the previous years, the viability of SOH modulators has been demonstrated in a series of experiments [43]–[45]. These devices consist of a silicon slot waveguide which is coupled to a metal transmission line via doped resistive silicon slabs. While such resistively-coupled SOH (RC-SOH) modulators can be readily realized using state-of-the-art silicon photonic fabrication process flows, they suffer from an inherent bandwidth limitation. The cross-section of a resistively-coupled SOH (RC-SOH) Mach-Zehnder modulator on the SOI platform is depicted in Fig. 2.3(a). A pair of silicon rails (green) confine the light to a silicon slot waveguide [46] having a typical slot width in the order of $w = 100\,\text{nm}$. A buried oxide (BOX) acts as a lower cladding material, and a spin-coated EO material as an upper cladding material. The modulating signal is carried by an RF transmission line (yellow) arranged in a ground-signal-ground (GSG) configuration, see Fig. 2.3(a). The silicon rails are connected to the metal transmission line using *n*-doped silicon slabs (dark green) having a height in the order of 70 nm. The doped silicon slabs provide a resistive connection between the electrodes and the silicon rails, hence the name resistively-

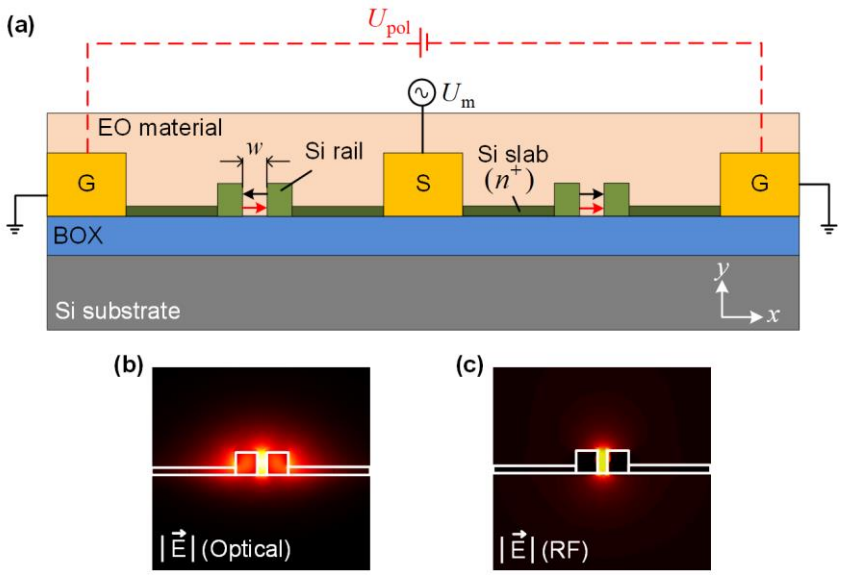

Figure 2.3: Resistively-coupled silicon-organic hybrid (RC-SOH) modulator. (a) Cross-section of RC-SOH Mach-Zehnder modulator (MZM) on the silicon-on-insulator platform. The slot waveguide consists of two silicon rails separated by a slot of width *w*. The slot waveguide is electrically connected to the RF transmission line arranged in ground-signal-ground (GSG) configuration via thin lightly doped silicon slabs. The upper cladding is formed by the organic electro-optic (EO) material which also fills the slot. The chromophores of the EO material are aligned (depicted along the red arrows) in a poling process, where a poling voltage U_{pol} (in red) is applied across the floating ground terminals at elevated temperatures. After cooling down and removing the voltage, the chromophores are locked in this orientation. An RF modulating signal U_{m} applied to the GSG terminals of the RC-SOH MZM drops predominantly in the slot. The modulating electric field (depicted along the black arrows) is oriented parallel to orientation of the EO chromophores in one arm, and is anti-parallel in the other arm, thus resulting in a push-pull operation of the MZM. **(b)** Plot of the field profile of the quasi-TE optical mode that is confined to the silicon slot waveguide. The discontinuity at the interface between silicon and the organic material leads to an enhancement of the electric field in the slot. **(c)** Plot of the field profile of the RF modulation signal. An RF voltage applied across the transmission line drops predominantly in the slot region leading to a large overlap between the optical and the RF fields.

coupled SOH modulator. Figure 2.3(b) shows the field profile of the quasi-transverse electric (quasi-TE) mode confined to the silicon slot waveguide. The electric field inside the silicon slot experiences a strong enhancement along the *x*-axis [46] due to the discontinuity of the normal electric field component at the interface of the silicon rail $(n_{\mathrm{Si}} = 3.5)$ to the EO material $(n_{\mathrm{EO}} \approx 1.7)$. The fundamental quasi-TE mode is fed in and out of the slot waveguides using standard silicon strip waveguide and mode converters [47]. A modulating voltage U_{m}

applied to the metal transmission line predominantly drops across the slot region, see Fig. 2.3(c). This results in a strong interaction of the modulating field with the optical mode in the slot, leading to an efficient phase modulation of the optical carrier.

To achieve a high modulation efficiency, an organic material with a large EO coefficient r_{33} is essential. After deposition of the organic material, the EO coefficient is virtually zero due to the random orientation of the dipolar chromophores. The chromophores of the organic material are aligned in a process called poling, in which dipole orientation is induced by an electric field while heating the material to its glass transition temperature T_g. After aligning the chromophores, the chip is cooled down to room temperature while maintaining the poling electric field, thereby locking the acentric order of the chromophores. In a single-drive MZM poling is accomplished by applying a DC voltage U_{pol} (indicated with a red dashed line) across the floating ground electrodes of the RF transmission line as depicted in Fig. 2.3(a). Consequentially, approximately half of the poling voltage drops across each silicon slot resulting in an antisymmetric alignment of the dipolar chromophores (indicated by red arrows) with respect to the modulation field of the transmission line (indicated by black arrows). The two phase modulators therefore provide a phase shift of equal magnitude φ but opposite in sign, resulting in a push-pull operation of the MZM. The phase shift φ experienced by an optical carrier as it travels through an SOH phase shifter of length L is given by

$$\varphi = \frac{1}{2} n_{EO}^3 r_{33} \frac{U_m}{w} \Gamma k_0 L. \tag{2.23}$$

In the above equation, $k_0 = 2\pi/\lambda_0$ is the vacuum wavenumber of the optical carrier having a wavelength λ_0, and Γ is the field interaction factor that quantifies the overlap of the optical and RF fields confined to the slot region. Assuming a parallel-plate approximation, the modulating electric field $E_m = U_m/w$ is assumed to be constant in the slot region A_{slot} which is defined by the width $w = 100\,\text{nm}$ of the slot and the height $h = 220\,\text{nm}$ of the silicon rails. The field interaction factor Γ is evaluated by an overlap integral of the vectorial electric and magnetic mode fields $\underline{E}_0(x,y)$ and $\underline{H}_0(x,y)$ of the quasi-TE mode with the slot region and is given by [36]

$$\Gamma = c\varepsilon_0 n_{\mathrm{EO}} \frac{\iint_{A_{\mathrm{slot}}} \left|\underline{E}_0(x,y)\right|^2 \mathrm{d}x\mathrm{d}y}{\iint \mathrm{Re}\left\{\underline{E}_0(x,y) \times \underline{H}_0^*(x,y)\right\} \cdot e_z \mathrm{d}x\mathrm{d}y}, \tag{2.24}$$

where c is the vacuum speed of light and ε_0 is the vacuum permittivity. The π-voltage $U_{\pi,\mathrm{PM}}$ of the SOH phase modulator is defined as the modulating voltage required to achieve a phase shift $\varphi = \pi$ and is given by

$$U_{\pi,\mathrm{PM}} = \frac{w\lambda}{\Gamma n_{\mathrm{EO}}^3 r_{33} L}. \tag{2.25}$$

For a push-pull MZM, the modulating voltage $U_{\pi,\mathrm{MZM}}$ required to achieve a π phase difference between the output fields of the two arms is halved with respect to the π-voltage $U_{\pi,\mathrm{PM}}$ of a pure phase modulator due to the opposite signs of the phase imparted in the each arm of the MZM,

$$U_{\pi,\mathrm{MZM}} = \frac{1}{2} \frac{w\lambda}{\Gamma n_{\mathrm{EO}}^3 r_{33} L}. \tag{2.26}$$

From Eq. (2.26), it can be noticed that $U_\pi \propto 1/L$, meaning that the U_π of a modulator can be reduced by increasing the length L of the modulator. Therefore, the π-voltage-length product $U_\pi L$ is regarded as a meaningful figure-of-merit for the modulator efficiency.

2.2.1.1 Bandwidth of an RC-SOH modulator

The operation bandwidth of a modulator ascertains its capability to respond to high-frequency modulation signals. The bandwidth of a RC-SOH modulator is limited by three factors: microwave (RF) propagation loss, beam walk-off, and *RC* cut-off frequency. The microwave propagation loss α reduces the modulation efficiency as it constantly diminishes the available modulation voltage along the length of the modulator. Furthermore, as the frequency increases, the microwave propagation loss $\alpha(\omega)$ increases due to the skin effect, and therefore limits the bandwidth of the modulator. As mentioned in the previous section, the π-voltage U_π of the modulator can be reduced by increasing its length L. However, if the group velocities of the optical and the microwave (RF) signals are not matched, the optical and the RF signals experience a spatial 'walk-

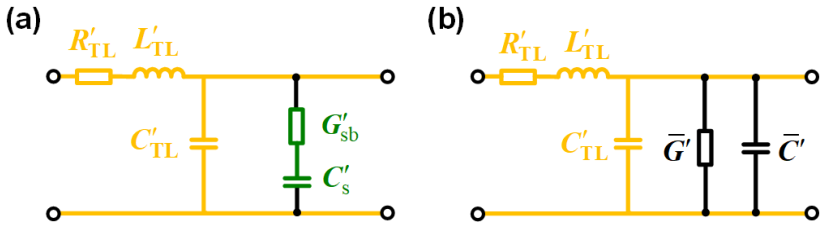

Figure 2.4: Equivalent-circuit models for estimation of EO bandwidth of RC-SOH MZM. All elements represent lumped differential quantities. **(a)** Equivalent-circuit of an infinitesimally short element of the transmission line formed by RC-SOH MZM. The differential elements R'_{TL}, L'_{TL} and C'_{TL} (yellow) correspond to the metal transmission line. The differential elements G'_{sb} and C'_s (green) represent the *RC* shunt load formed by the doped-Si slab and the Si slot waveguide respectively. **(b)** Telegrapher-type equivalent-circuit representation of an MZM transmission-line element. The equivalent-circuit of RC-SOH MZM shown in (a) is transformed into a telegrapher-type model using a frequency-dependent differential shunt conductance $\bar{G}'$ and a frequency-dependent differential shunt capacitance $\bar{C}'$.

off' and result in a reduced bandwidth of the modulator. A significant contribution to the bandwidth limitation is due to the *RC* time constant arising from the finite resistance of the doped silicon slabs and the capacitance of the silicon slot. This *RC* time constant determines the charging and discharging rate of the capacitor that is formed by the silicon slot waveguide.

The equivalent-circuit model of the RC-SOH MZM is depicted in Fig. 2.4(a). The lumped differential elements R'_{TL}, L'_{TL} and C'_{TL} (yellow) represent the equivalent-circuit of the metal transmission line according to the telegrapher's equation. The slot region is represented in the equivalent circuit Fig. 2.4(a) by series-connected differential elements (green) slab conductance G'_{sb} and slot capacitance C'_s. The equivalent-circuit in Fig. 2.4(a) can be transformed into a telegrapher-type equivalent-circuit, see Fig. 2.4(b), where $\bar{G}'(\omega)$ and $\bar{C}'(\omega)$ represent the frequency-dependent conductance and capacitance, respectively of the slot region including the resistive silicon slabs. The complex propagation constant of the loaded transmission line in Fig. 2.4(b) is given by

$$\underline{\gamma} = \alpha + \mathrm{j}\beta = \sqrt{(R'_{TL} + \mathrm{j}\omega_m L'_{TL})(\bar{G}' + \mathrm{j}\omega_m(\bar{C}' + C'_{TL})}, \qquad (2.27)$$

where α and β are the amplitude attenuation constant and phase constant of the RF modulating signal with an angular frequency $\omega_m = 2\pi f_m$.

The frequency-dependent sinusoidal phase modulation φ considering the microwave attenuation and the velocity mismatch of the optical and RF waves is given by [48]

$$\varphi(\omega_{\mathrm{m}},t)=\varphi_0\,\frac{1}{L}\int_0^L \mathrm{e}^{-\alpha z}\cos\left(\omega_{\mathrm{m}}\left(\frac{\Delta t_{\mathrm{o,m}}}{L}z-t\right)\right)\mathrm{dz}, \tag{2.28}$$

where φ_0 corresponds to the phase modulation at an angular frequency $\omega_{\mathrm{m}}=0$, and where $\Delta t_{\mathrm{o,m}}$ is the temporal walk-off between the optical and the electrical waves, described by

$$\Delta t_{\mathrm{o,m}}=\left|\frac{L}{v_{\mathrm{g,o}}}-\frac{L}{v_{\mathrm{g,m}}}\right|=\frac{L}{c}\left|n_{\mathrm{g,o}}-n_{\mathrm{g,m}}\right|. \tag{2.29}$$

In this relation, $v_{\mathrm{g,o}}$ and $v_{\mathrm{g,m}}$ are the group velocities of the modulation signal and the optical signal, respectively. The quantities $n_{\mathrm{g,o}}$ and $n_{\mathrm{g,m}}$ correspond to the group refractive index of the optical and the RF modulating signal, respectively. From Eq. (2.29), the contribution due to the microwave attenuation can be introduced by a frequency-dependent effective device length L_{eff},

$$L_{\mathrm{eff}}(\omega_{\mathrm{m}})=\int_0^L \mathrm{e}^{-\alpha(\omega_{\mathrm{m}})z}\,\mathrm{dz}=\frac{1}{\alpha}\left(1-\mathrm{e}^{-\alpha(\omega_{\mathrm{m}})L}\right). \tag{2.30}$$

The EO frequency response $m(\omega_{\mathrm{m}})$ of a modulator is given by the magnitude of the induced phase shift $\varphi(\omega_{\mathrm{m}})$, normalized to its value at low frequency, i. e., $\omega_{\mathrm{m}}=0$. Neglecting the beam walk-off $\left(n_{\mathrm{g,o}}=n_{\mathrm{g,m}}\right)$, the EO response of a modulator with a geometrical modulator length L is given by [49]

$$\begin{aligned} m(\omega_{\mathrm{m}})&=\frac{\varphi(\omega_{\mathrm{m}})}{\varphi(0)}=\frac{1}{L}H_{\mathrm{RC}}(\omega_{\mathrm{m}})\,L_{\mathrm{eff}}(\omega_{\mathrm{m}}),\\ H_{\mathrm{RC}}(\omega_{\mathrm{m}})&=\frac{1}{1+\mathrm{j}\omega_{\mathrm{m}}C'/G'}, \end{aligned} \tag{2.31}$$

where $H_{\mathrm{RC}}(\omega_{\mathrm{m}})$ is the fraction of the modulation voltage that is effective across the slot capacitance due to the voltage divider formed by the differential shunt conductance G' and the differential shunt capacitance C', see Fig. 2.4(a).

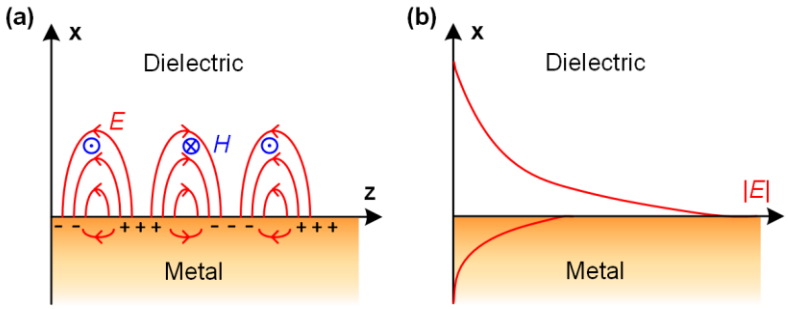

Figure 2.5: **Surface plasmon polariton (SPP) propagating along a metal-dielectric interface. (a)** Schematic of the electric (red) and magnetic (blue) fields of the SPP at the metal-dielectric interface along with the charge oscillations in the metal. **(b)** Plot showing the exponential decay of the electric field further away from the metal-dielectric interface. The electric field decays much stronger in the metal due to the higher optical absorption.

It is evident from Eq. (2.31) that the EO frequency response $m(\omega_m)$ is larger for a smaller C'/G' time constant. This *RC*-time constant of an RC-SOH modulator can be reduced by increasing the doping concentration of the silicon slabs. However, this leads to higher optical losses due to the close proximity of the charge carriers to the silicon slot waveguide.

2.2.2 Plasmonic-organic hybrid (POH) modulator

The bandwidth limitations of the resistively-coupled SOH (RC-SOH) modulator can be overcome by combining organic EO materials with plasmonic waveguides, leading to the so-called plasmonic-organic hybrid (POH) integration concept. This section introduces the fundamentals of plasmonic waveguides and the concept of POH modulators along with their bandwidth capabilities.

2.2.2.1 Plasmonic slot waveguides

Plasmonic waveguides allow confinement of light beyond the diffraction limit [50] and rely on surface plasmon polaritons (SPPs). SPPs are discussed here to an extent that is necessary for the understanding of this thesis. For a deeper understanding of the fundamentals of plasmonics, the reader is referred to the text book of Stefan Maier [51]. Surface plasmon polaritons (SPPs) are electromagnetic waves coupled to electron plasma oscillations at the metal-dielectric interface and decay exponentially away from the interface. Figure 2.5(a)

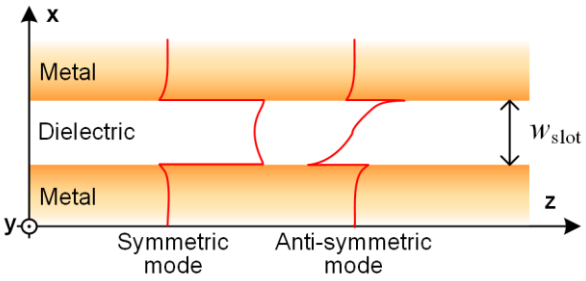

Figure 2.6: Schematic showing a plasmonic slot waveguide with the dielectric and the metal electrodes infinitely extending in *z*- and *y*- direction. The plot shows the electric E_x-field of the symmetric and anti-symmetric modes that can propagate in the metal-insulator-metal (MIM) slot waveguide.

shows the electric and the magnetic fields of a SPP that are coupled to the oscillating charges along a metal-dielectric interface. As shown in Fig. 2.5(b), the SPP is strongly confined to the interface and exponentially decays along the $\pm$x direction.

The optical mode can be squeezed into a much smaller volume by using more than one metal-insulator interface. A plasmonic slot waveguide, also called a metal-insulator-metal (MIM) slot waveguide, consists of two metal layers separated by a dielectric gap having a width w_{slot}, see Fig. 2.6. Each metal-insulator interface supports an SPP mode, and when the two interfaces are brought closer, the SPP modes couple, resulting in a plasmonic slot mode. The coupling of two SPP modes results in two solutions, a symmetric mode and an anti-symmetric mode that propagate along the MIM slot. In the case of the symmetric mode, the E_x-field is strongly confined to the dielectric slot region, and it decays exponentially into the metals along the x-direction. The E_x-field of the anti-symmetric mode changes sign in the dielectric slot region. At telecommunication wavelengths and at technically relevant slot widths the anti-symmetric mode is below its cut-off frequency. A more detailed description of MIM slot waveguides can be found in [52], [53].

2.2.2.2 Principle of operation & bandwidth of POH modulators

The plasmonic-organic hybrid (POH) modulator combines plasmonic MIM slot waveguides with organic EO materials. Figure 2.7(a) depicts the cross-section of a POH Mach-Zehnder modulator (MZM) built on the SOI platform. Each

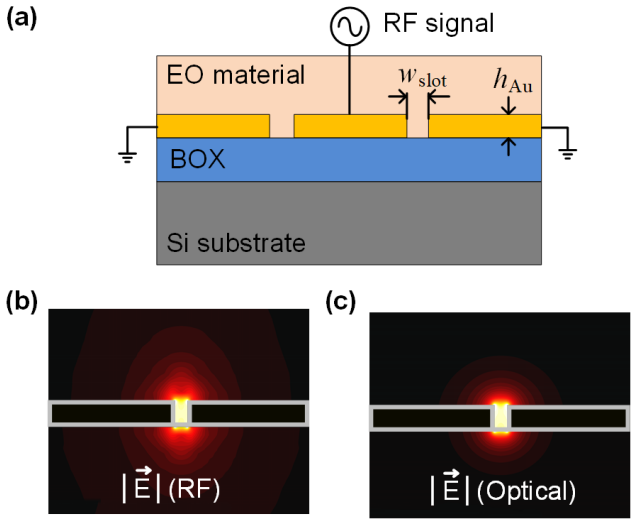

Figure 2.7: Plasmonic-organic hybrid modulator. (a) Cross-section of POH Mach-Zehnder modulator (MZM) on the SOI platform. Each MZM arm consists of a plasmonic slot waveguide of width w_{slot} formed by the gold strips. The slots are filled with an organic EO material and the chromophores are aligned in a poling process, see Sec 2.2.1. An RF signal applied to the gold electrodes drops in the slot and modulates the plasmonic mode propagating through it. **(b)** Plot of the electric field profile of the RF modulation field tightly confined to the plasmonic slot. **(c)** Plot of the field profile of the symmetric optical mode that propagates through plasmonic slot waveguide. A high overlap between the optical and the RF fields results in a high efficiency of the POH modulators.

arm of the MZM contains a POH phase modulator section comprising a narrow metallic slot having a typical width $w_{slot} = 75\,\text{nm}...100\,\text{nm}$ between gold electrodes (yellow) with a height $h_{Au} = 150\,\text{nm}$. The slots are filled with an organic EO material, and the chromophores are aligned in a poling process similar to the one explained in Sect. 2.2.1. A modulating RF signal applied to the gold electrodes drops predominantly across the metal slot region, see Fig. 2.7(b). At the same time, the optical mode is also tightly confined to the plasmonic slot

waveguide, see Fig. 2.7(c), leading to a strong overlap between the optical and the RF electric fields. The POH MZM is configured to be operated in push-pull mode by appropriately choosing the poling field and the RF field, see Sect. 2.2.1. POH modulators are more efficient than SOH modulators due to the much larger field interaction factor Γ, see Eq. (2.24). For a similar slot width, the field interaction factor can be up to 3 times larger than for SOH devices [36], see Fig. 2.8. This is due to both the tight confinement of the plasmonic mode to the slot region, and the reduced group velocity of the plasmonic slot waveguide

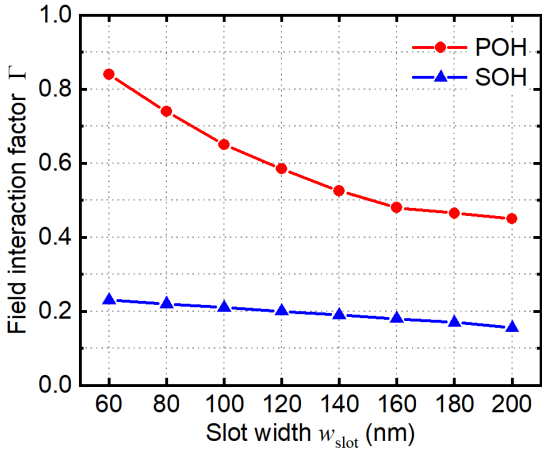

Figure 2.8: Field interaction factor Γ of the optical mode with the EO cladding material in the slot region as a function of slot width w_{slot} for both POH and SOH waveguides at a wavelength of 1550 nm. For the SOH modulator, a slot waveguide having a height of 220 nm, a Si rail width of 240 nm and a Si slab of 70 nm are chosen for the calculations. The POH devices considered for the calculations have a gold thickness of 150 nm. In general, POH devices feature a 2.5 – 3.5 times larger field interaction factor than SOH devices due to the tight confinement of the plasmonic mode to the slot region and due to a reduced group velocity of the plasmonic slot mode. Figure and caption adapted from [36].

mode. As a consequence, record-low voltage-length products down to $U_\pi L = 0.05\ \text{Vmm}$ were demonstrated with POH devices [54]. This leads to device lengths as small as few tens of microns, which makes POH devices suitable to high-density on-chip integration. However, the high propagation loss of SPPs in a plasmonic slot waveguide leads to a rather large insertion loss of POH devices. For 150 nm thick gold layers separated by a 75 nm wide plasmonic slot, the insertion loss amounts to about 0.8 dB/µm [55] resulting in an insertion loss of 16 dB for a 20 µm long POH modulator.

The RF bandwidth of the POH modulator is limited by the *RC* cut-off frequency only. The bandwidth limitation due to the microwave loss and the walk-off between optical and the microwave signals is negligible because the POH device lengths are much shorter than the RF wavelength. In fact, POH devices do not have any intrinsic bandwidth limitations, since the slot capacitance is connected to the driving source by a highly conductive $(R \to 0)$ metal film. The ultra-small slot capacitance $C_s = 3\text{fF}$ of a POH modulator permits a theoretical *RC* cut-off frequency in excess of 1 THz [34], [36] when connected to a driving

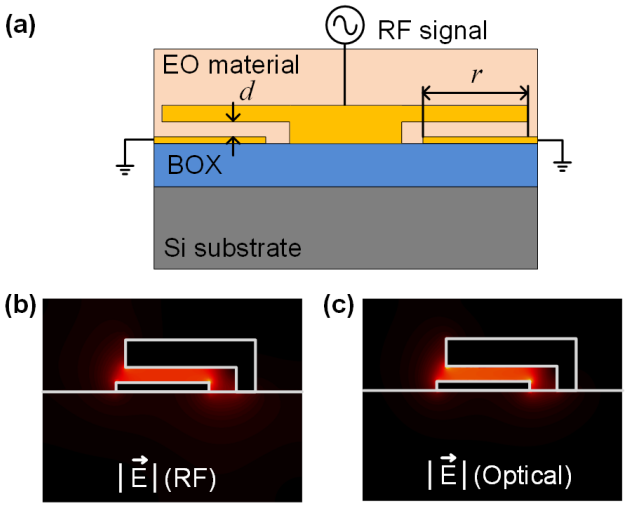

Figure 2.9: Horizontal-slot POH (HS-POH) modulator. **(a)** Cross-section of HS-POH Mach-Zehnder modulator (MZM) on the SOI platform. The horizontal slot configuration of POH modulators relaxes the alignment tolerances of conventional POH modulators and allows fabrication of high aspect ratio plasmonic slot waveguides. **(b)** Plot of the electric field profile of the RF modulation field tightly confined to the plasmonic slot. **(c)** Plot of the field profile of the symmetric optical mode confined to the plasmonic slot waveguide.

source with a 50 Ω internal impedance. The broadband characteristics of the POH modulator have been experimentally verified in Sect. 3.3.

Horizontal-slot plasmonic-organic hybrid (HS-POH) modulator

Plasmonic-organic hybrid modulators offer extremely high operating bandwidths, however, their fabrication requires lithographic techniques with very strict alignment tolerances. Furthermore, the field interaction factor of conventional POH modulators is limited due to the process-imposed restrictions that limit the aspect ratio of the plasmonic slot waveguides, see Sect. 2.3.2. The aspect ratio r/d . of a plasmonic slot waveguide is defined as the ratio of the width r of the metal rails to the distance d between the metal rails. The POH modulators presented in the previous section feature a vertical plasmonic slot and have a maximum possible aspect ratio $r/d = h_{\mathrm{Au}}/w_{\mathrm{slot}} = 3$ that is limited due to the fabrication process, see Sect. 2.3.2. On the contrary, the horizontal-slot POH (HS-POH) modulator, shown in Fig. 2.9(a), relaxes the fabrication process for realizing plasmonic slot waveguides with aspect ratios larger than 12. HS-POH modulators with high-aspect ratio plasmonic slot waveguides lead to a larger

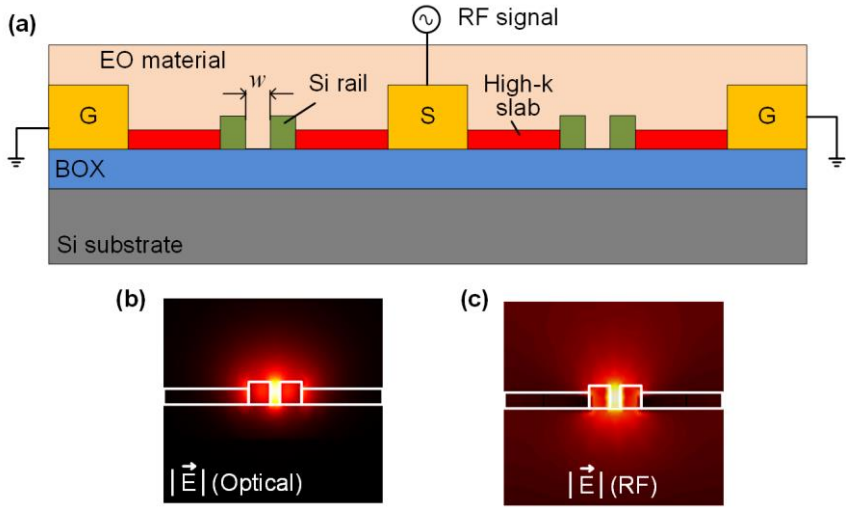

Figure 2.10: Capacitively-coupled silicon-organic hybrid (CC-SOH) modulator. (a) Cross-section of CC-SOH Mach-Zehnder modulator (MZM) on the silicon-on-insulator platform. Each MZM arm comprises a silicon slot waveguide having a slot width *w*. The slot waveguide is electrically connected to the RF electrodes arranged in ground-signal-ground (GSG) configuration via high-k dielectric slabs. The upper cladding is formed by the organic electro-optic (EO) material that also fills the slot. **(b)** Plot of the field profile of the quasi-TE optical mode that is confined to the silicon slot waveguide. The discontinuity at the interface between silicon and the organic material leads to an enhancement of the field in the slot. **(c)** Plot of the electric field profile of the RF mode confined to the slot region. The modulating RF field drops predominantly in the slot region and experiences a strong field enhancement due to the large difference in the relative permittivity of high-k dielectric slab with respect to the silicon rail as well as the organic EO material.

field interaction factor, see Sect. 4.2, and thereby increase the modulation efficiency. Figure 2.9(b) and (c) show the electric field profiles of the RF modulating field and the quasi-TE optical mode confined to the plasmonic slot waveguide, respectively.

2.2.3 Capacitively-coupled SOH (CC-SOH) modulator

Although POH devices offer a solution to overcome the bandwidth limitation of RC-SOH modulators, they are limited in application due to high insertion losses. In contrast, capacitively-coupled SOH (CC-SOH) modulators offer large bandwidths while simultaneously keeping the insertion loss tolerable. The cross-section CC-SOH Mach-Zehnder modulator (MZM) on the SOI platform is depicted in Fig. 2.10(a), in which the doped silicon slabs in the RC-SOH

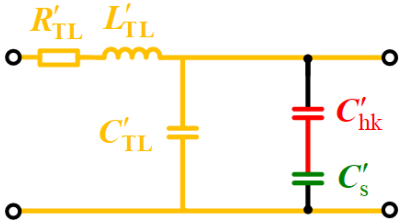

Figure 2.11: Equivalent-circuit of an infinitesimally short element of the transmission line formed by CC-SOH MZM. The differential elements R'_{TL}, L'_{TL} and C'_{TL} (yellow) correspond to the metal transmission line. The elements C'_{hk} (red) and C'_{s} (green) represent the shunt load formed by the high-k dielectric slab and the Si slot waveguide respectively. All elements represent lumped differential quantities.

MZM, see Fig. 2.3(a), are replaced by high-k dielectric slabs. A pair of silicon slot waveguides having a slot width *w* confine the light along the length of the device, a buried oxide (BOX) acts as a lower cladding material, and an EO material that infiltrates the slot acts as an upper cladding material. The modulating signal is carried by an RF transmission line (depicted in yellow) arranged in a ground-signal-ground (GSG) configuration. If the high-k dielectric has a relative permittivity ε_r much larger than that of Si and the EO polymer, the RF voltage drops predominantly across the slot region. The high-k dielectric is chosen such that its refractive index for optical wavelengths is smaller than n_{Si} such that the confinement of the optical mode to the slot region is not impaired. Figures 2.10(b) and (c) show the electric field profiles of the RF mode and the optical quasi-TE mode of the CC-SOH phase modulator, respectively. Since the relative permittivity of the high-k dielectric is much larger than the relative permittivity of the Si or of the EO polymer, the RF field in the slot region is strongly enhanced [56]. The CC-SOH modulator thus combines a silicon photonic slot waveguide for optical frequencies with a high-k dielectric slot waveguide for RF frequencies [57]. The strong confinement of both the optical and RF fields to the EO material of the slot region ensures an efficient modulation, without the need for doping the Si rails.

The equivalent-circuit model of the CC-SOH MZM is depicted in Fig. 2.11. The lumped differential elements R'_{TL}, L'_{TL} and C'_{TL} represent the equivalent-circuit of the metal transmission line according to the telegrapher's equation. The slot region is represented in the equivalent circuit Fig. 2.11 by series-connected element high-k capacitance C'_{hk} (red) and slot capacitance C'_{s} (green). In analogy

to Eq. (2.31), the EO frequency response $m(\omega_\mathrm{m})$ of the CC-SOH MZM is given by

$$\begin{aligned} m(\omega_\mathrm{m}) &= \frac{\varphi(\omega_\mathrm{m})}{\varphi(0)} = \frac{1}{L} H_\mathrm{CC}(\omega_\mathrm{m})\, L_\mathrm{eff}(\omega_\mathrm{m}), \\ H_\mathrm{CC}(\omega_\mathrm{m}) &= \frac{1}{1+\dfrac{\mathrm{j}\omega_\mathrm{m} C'_\mathrm{s}}{\mathrm{j}\omega_\mathrm{m} C'_\mathrm{hk}}}, \end{aligned} \tag{2.32}$$

where $H_\mathrm{CC}(\omega_\mathrm{m})$ is the fraction of the modulation voltage that is effective across slot capacitor due to the voltage divider formed by the high-k capacitance C'_hk and the slot capacitance C'_s. For high-k dielectric materials satisfying the relation $C'_\mathrm{hk} \gg C'_\mathrm{s}$, it follows that $H_\mathrm{CC}(\omega_\mathrm{m}) \approx 1$. Thus, the CC-SOH modulator overcomes the *RC* limited bandwidth of the conventional resistively-coupled SOH devices.

2.3 Fabrication processes for high-speed EO modulators

The high-speed EO modulators presented in this thesis were fabricated in clean-room facilities of the Institute of Microstructure Technology (IMT) and the Karlsruhe Nano Micro Facility at Karlsruhe Institute of Technology (KIT). This section briefly describes the processes that were developed for the fabrication of POH and CC-SOH modulators. The detailed fabrication recipes can be found in Appendix C. The manufacture of both types of modulators begins with the fabrication of the respective passive silicon structures.

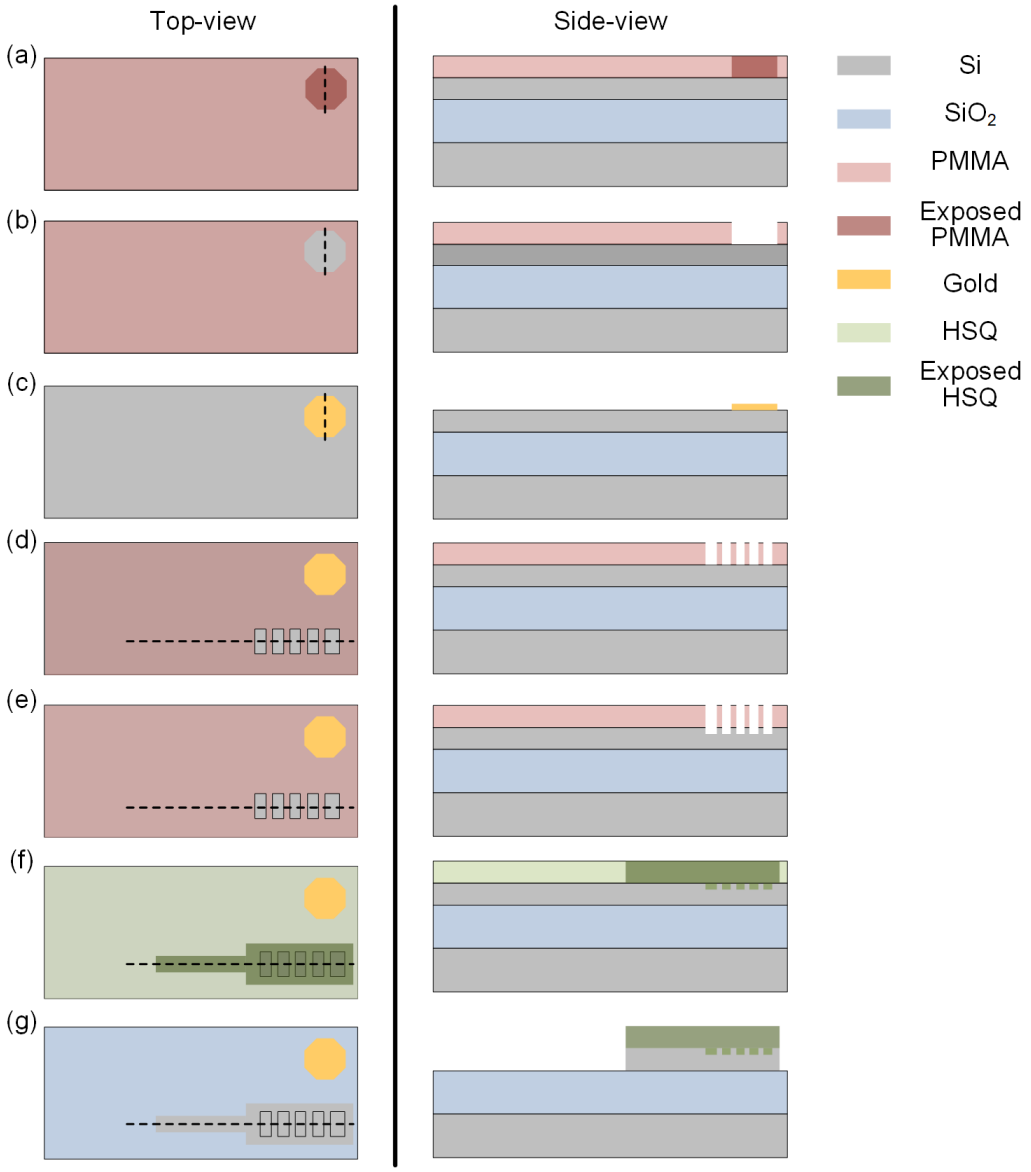

Figure 2.12: **Fabrication process flow for passive silicon structures on SOI substrates.** The cross-section shown in the side-view corresponds to the dashed line shown in the top-view. **(a)** Patterning of octagonal marker into the PMMA resist. **(b)** Development of PMMA resist to reveal the silicon device layer in the exposed regions. **(c)** Evaporation of gold onto the PMMA mask followed by the stripping of the resist. The steps from (a) – (c) form the so-called 'lift-off' process. **(d)** Patterning and development of PMMA resist to create a mask for shallow-etch of silicon, e.g., for shallow-etched grating couplers. **(e)** Reactive-ion-etching of silicon to fabricate shallow-etch structures followed by stripping of the PMMA resist. **(f)** Patterning and development of the HSQ resist for fully-etched structures in silicon. **(g)** Reactive-ion-etching of silicon to realize fully etched structures.

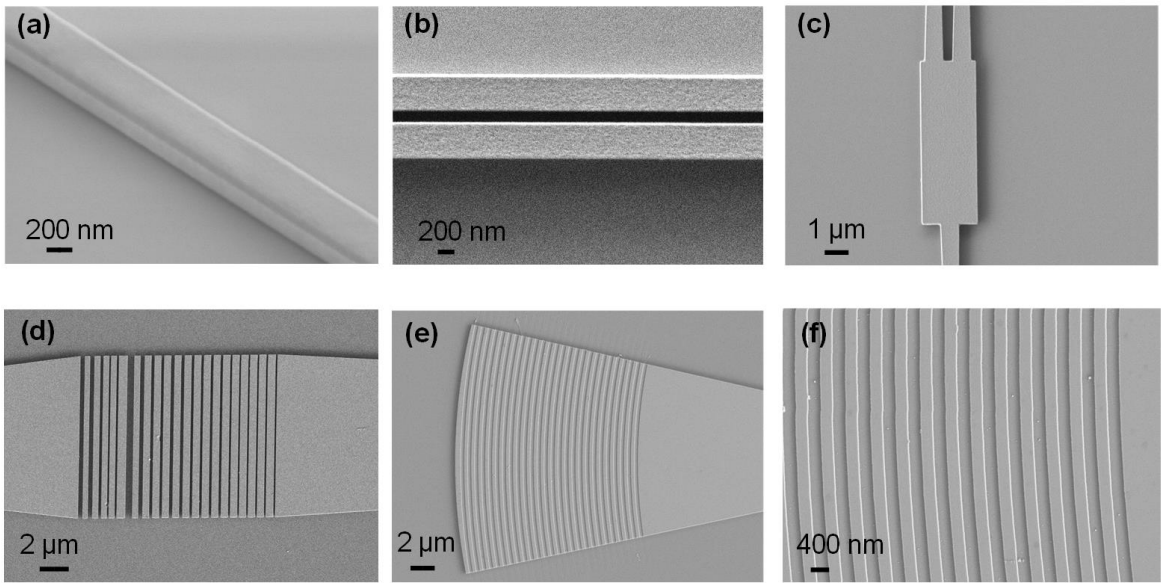

Figure 2.13: Scanning electron microscope (SEM) images of passive silicon structures fabricated on an SOI chip. (a) Tilted view of a silicon strip waveguide with HSQ resist on top. **(b)** Silicon slot waveguide. **(c)** Multi-mode interference (MMI) coupler. **(d)** Fully etched grating coupler (FEGC). **(e)** Partially etched grating coupler (PEGC). **(f)** Zoom-in of the PEGC structure showing the shallow etch regions.

2.3.1 Fabrication of passive silicon structures

The POH and CC-SOH modulators are fabricated on silicon-on-insulator (SOI) substrates consisting of a 220 nm thick silicon device layer and a buried silicon dioxide (SiO_2; BOX) with a thickness of 2 µm on a 725 µm thick silicon handle wafer. Before fabrication, a 200 mm SOI wafer is diced into 2 cm × 2 cm large chips. The structures are patterned using two different electron beam (e-beam)

resists – a positive-tone polymethyl methacrylate (PMMA) resist and a negative-tone hydrogen silsesquioxane (HSQ) resist. The patterns are exposed into the resist layers using a Raith EBPG5200 e-beam lithography system. The underlying processes to realize passive silicon structures are summarized in Fig. 2.12.

For the multi-step lithographic process, a set of gold markers is fabricated at the four corners of the chip to enable an alignment accuracy down to 20 nm between different lithography steps. The markers are fabricated in a lift-off process,

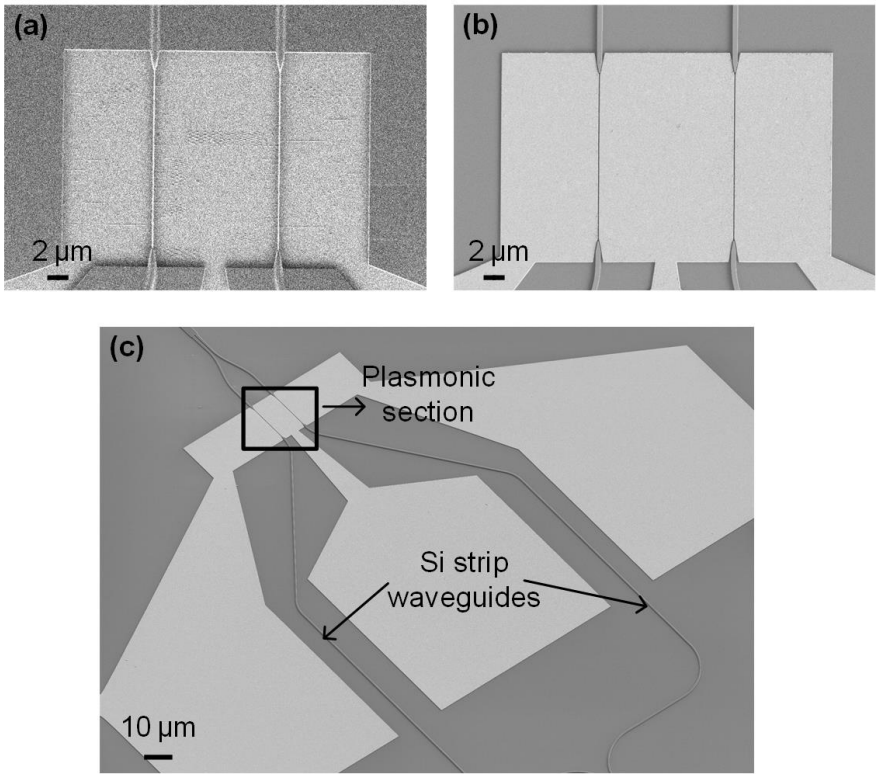

Figure 2.14: SEM images of plasmonic slot waveguide and contact pads of POH modulator. **(a)** Before lift-off: Patterns exposed and developed in the PMMA resist. **(b)** After lift-off: Gold pads forming plasmonic slot waveguides of a POH Mach-Zehnder modulator. **(c)** Tilted view of a POH MZM before the deposition of organic EO material, showing the silicon feed waveguides and the plasmonic section along with the RF contact pads.

where an exposed and developed octagonal pattern in PMMA resist is deposited with 50 nm gold, followed by a subsequent removal of the PMMA resist in acetone from the unexposed regions, see Fig. 2.12(a)-(c). In some device generations, partially etched grating couplers (PEGC) are used for improved fiber-to-chip coupling efficiency. The PEGC are fabricated in a two-step lithographic process. In the first step, PMMA resist is patterned and developed to define the shallow etch regions which are subsequently etched into the silicon device layer using an inductively-coupled-plasma reactive-ion-etching (ICP-RIE) tool. For better control of the etch depth, the partial silicon etch is carried out by using a chemistry of SF_6 and CHF_3 gases at room temperature, see Fig. 2.12(d) and (e). The passive silicon structures such as strip waveguides, multi-mode interference (MMI) couplers, and fully etched grating couplers (FEGC), that require a full etch of the silicon device layer, are fabricated using an HSQ mask. The

patterns are exposed into the HSQ resist and developed using a 25 % aqueous solution of tetra-methyl ammonium hydroxide (TMAH). The exposed resist patterns are then transferred to the silicon device layer by ICP-RIE. To achieve a 90° sidewall for the silicon waveguides and to attain a good etch selectivity with the HSQ mask, silicon is etched at a cryogenic temperature of −110°C using a chemistry of SF_6 and O_2 gases, see Fig. 2.12(d) and (e). Figure 2.13 shows scanning electron microscope (SEM) images of some passive silicon structures fabricated on the SOI chip.

2.3.2 Fabrication of POH modulator

Following the fabrication of the passive silicon structures as described in Sect. 0, the core structures of the POH modulator comprising the plasmonic slot waveguides and the RF contact pads are realized in an additional lithography step. Both structures are fabricated using a lift-off process with PMMA resist, see Fig. 2.12(a)-(c). The process parameters, i.e., the resist thickness, the development time, and the evaporation rate of gold, are carefully optimized to obtain plasmonic slot waveguides with slot widths down to 50 nm. Figures 2.14(a) and (b) show the SEM images of plasmonic slot waveguides before and after the lift-off process, respectively. The POH Mach-Zehnder modulator along with the silicon waveguides and the RF contact pads is shown in Fig. 2.14(c).

For the vertical slot POH modulators, an optimal gold thickness of 150 nm is chosen as a trade-off between the performance of the POH modulator and the reliability of the lift-off process. This limitation arises due to the stability of the developed PMMA structures that are required to be undistorted at an elevated temperature during the evaporation of gold. Therefore, the height-to-width ratio of vertical plasmonic slot waveguides is limited to a maximum value of 3, which restricts the field interaction factor that can be attained with vertical plasmonic slot waveguides, see Sect. 2.2.2.

Fabrication of horizontal-slot POH (HS-POH) modulator

The HS-POH modulator described in Sect. 2.2.2 allows increasing the field interaction factor, and thereby the efficiency of POH modulators, by overcoming the aspect-ratio limitations of the vertical-slot plasmonic waveguides. After the

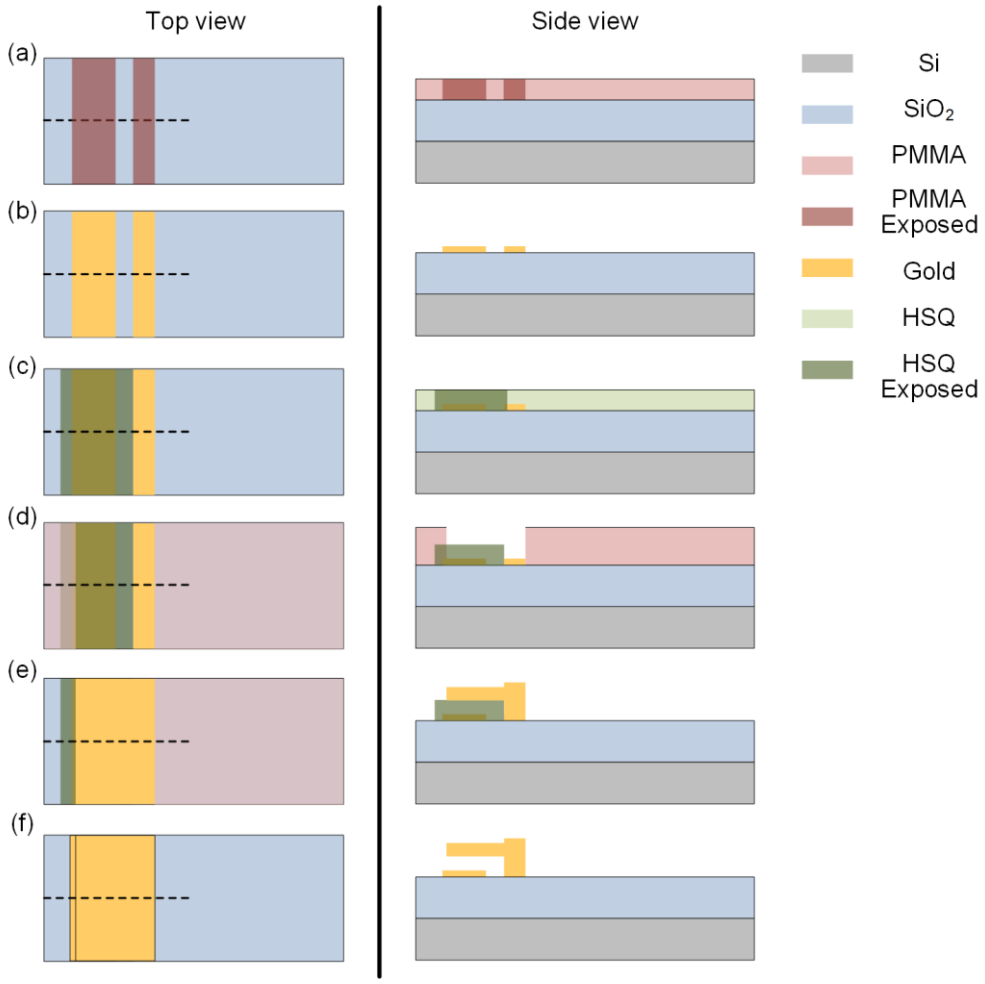

Figure 2.15: Fabrication process flow for horizontal-slot plasmonic waveguides. **(a)** Patterning of the bottom metal layer in PMMA resist. **(b)** Evaporation of gold for the bottom metal layer, followed by lift-off of PMMA resist. **(c)** Exposure of HSQ resist to define the region that forms the horizontal slot. **(d)** Patterning and development of PMMA resist to create a mask for the top metal layer. **(e)** Evaporation and subsequent lift-off that forms the top metal layer. **(f)** Sacrificial wet-etch of HSQ resist to form the horizontal plasmonic slot waveguide.

fabrication of passive silicon structures as described in Sect. 0, the fabrication of HS-POH modulator requires three additional lithography steps. The fabrication process flow is summarized in Fig. 2.15. In the first lithography step, the bottom gold layer is fabricated by defining the patterns in PMMA resist followed by a lift-off of the resist after gold evaporation, see Fig. 2.15(a) and (b). The second lithography step in HSQ resist then defines the slot region of the horizontal plasmonic slot waveguide, see Fig. 2.15(c). The height of the plasmonic slot can be defined very precisely by controlling the spin parameters

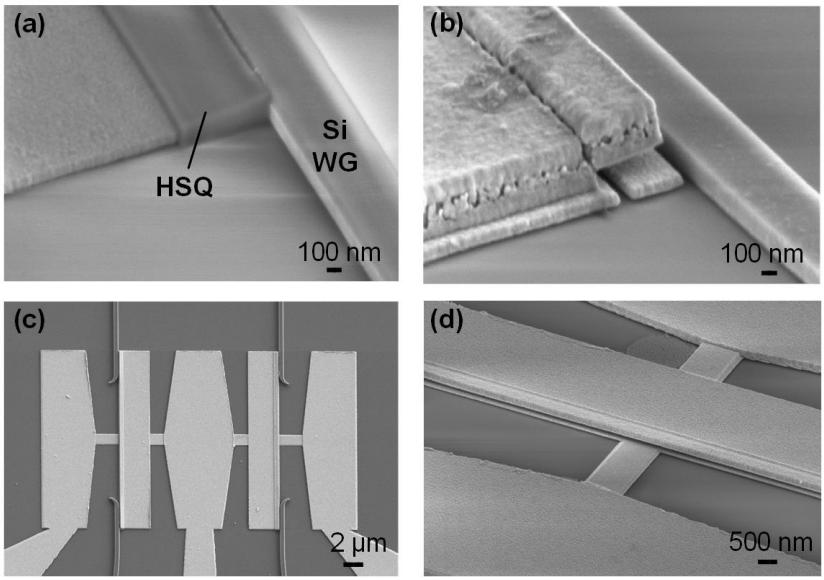

Figure 2.16: Horizontal-slot POH (HS-POH) modulator. **(a)** Patterning of the HSQ resist to define the slot region of the HS-POH modulator, see Fig. 2.15(c). The horizontal plasmonic slot is fabricated adjacent to the silicon waveguide (Si WG) to enable photonic-to-plasmonic coupling. **(b)** Horizontal plasmonic slot waveguide after lift-off and sacrificial removal of the HSQ resist. **(c)** Top-view of the HS-POH Mach-Zehnder modulator (MZM). (d) 10-µm-long horizontal plasmonic slot waveguide of one of the MZM arms.

of the HSQ resist, see SEM in Fig. 2.16(a). The last lithography step in PMMA resist defines the regions for the deposition of the top metal layer, which after lift-off forms a gold bridge structure, see Fig. 2.15(d) and (e). The sacrificial HSQ resist that fills the horizontal plasmonic slot waveguide is removed by a wet-etch process using hydrofluoric (HF) acid, thus forming a free-standing horizontal plasmonic slot waveguide, see Fig. 2.15(f) and SEM in Fig. 2.16(b). After the sacrificial removal of the HSQ resist, the sample is dried using a critical-point dryer (CPD) in order to avoid a collapse of the top gold layer due to the surface tension. The micrographs in Fig. 2.16(c) and (d) show the top-view of the fabricated HS-POH MZM and a horizontal plasmonic slot waveguide, respectively.

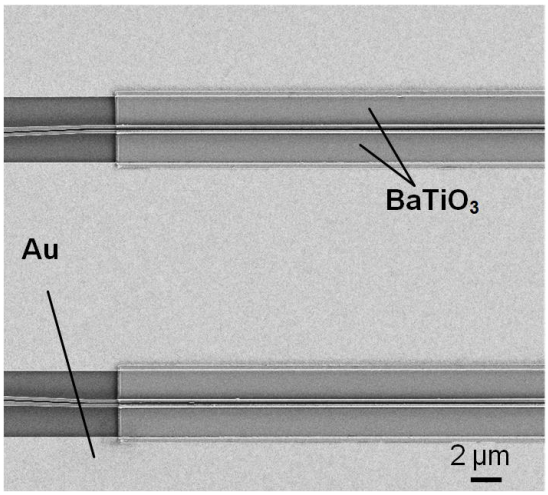

Figure 2.17: SEM image of the CC-SOH Mach-Zehnder modulator after the lift-off of gold strips and the $BaTiO_3$ slabs on either side of the silicon slot waveguide.

2.3.3 Fabrication of CC-SOH modulator

After the fabrication of the passive silicon structures described in Sect. 0, the CC-SOH modulator is realized with two additional lithography steps in combination with lift-off processes. In the first lift-off process, the RF transmission lines and the contact pads of the CC-SOH MZM are realized using PMMA resist and a 150 nm thick layer of gold. The high-k dielectric material, in this case amorphous $BaTiO_3$ (BTO), is deposited and structured via a second lift-off process. The CC-SOH devices investigated in this thesis are realized using a 150 nm thick BTO film that is deposited using room-temperature RF magnetron sputtering with Ar. For a better lift-off of the BTO films, it is important that the sample temperature remains below the glass transition temperature $T_g \sim 110\,°C$ of the PMMA resist during the sputtering process. To ensure this, a sufficient pause is introduced between the deposition cycles to cool the samples. Because of the room-temperature sputter deposition, the BTO films are expected to be amorphous in nature. Figure 2.17 shows a scanning electron microscope (SEM) image of the fabricated CC-SOH MZM depicting the gold (Au) transmission lines and the $BaTiO_3$ slabs.

3 Ultra-broadband POH modulator

The current chapter discusses the broadband characteristics of POH modulators and demonstrates application of POH modulators as direct terahertz-to-optical converters for future THz wireless communication links. The chapter is taken from a publication [J3] in Nature Photonics. The contents of the journal publication are adapted to fit the structure and layout of this thesis. Methods and Supplementary Information associated with the publication can be found in Appendix A.

For this publication, Sandeep Ummethala (S.U.), Tobias Harter (T.H.), Wolfgang Freude (W.F.) and Christian Koos (C.K.) developed the concept and designed the experiment. S.U. and Zheng Li designed the modulators and fabricated them with support from Kira Koehnle, Sascha Mühlbrandt, Suresh K. Garlapati, Andreas Bacher and Lothar Hahn. S.U. and T.H. performed the transmission experiments and analyzed the data together with Juned Kemal, Jochen Schaefer and Pablo Marin-Palomo. Yasar Kutuvantavida developed the poling procedure for the POH modulators and formulated the organic EO material. Axel Tessmann and Martin Walther developed and provided the THz MMIC amplifiers. The work was supervised jointly by Thomas Zwick. Sebastian Randel, W.F., and C.K. S.U., W.F., and C.K. wrote the paper. All authors revised the paper.

[Start of paper [J3]]

THz-to-Optical Conversion in Wireless Communications Using an Ultra-broadband Plasmonic Modulator

Nature Photonics, 13(8), pages: 519-524
DOI: 10.1038/s41566-019-0475-6

S. Ummethala[1,2], T. Harter[1,2], K. Koehnle[1,2], Z. Li[1], S. Muehlbrandt[1,2], Y. Kutuvantavida[1,2], J. Kemal[1], P. Marin-Palomo[1], J. Schaefer[4], A. Tessmann[5], S. K. Garlapati[3], A. Bacher[2], L. Hahn[2], M. Walther[5], T. Zwick[4], S. Randel[1], W. Freude[1], C. Koos[1,2]

[1] Institute of Photonics and Quantum Electronics (IPQ), Karlsruhe Institute of Technology (KIT), 76131 Karlsruhe, Germany
[2] Institute of Microstructure Technology (IMT), Karlsruhe Institute of Technology (KIT), 76334, Eggenstein-Leopoldshafen, Germany
[3] Institute of Nanotechnology (INT), Karlsruhe Institute of Technology (KIT), 76334, Eggenstein-Leopoldshafen, Germany
[4] Institute of Radio Frequency Engineering & Electronics (IHE), Karlsruhe Institute of Technology (KIT), 76131 Karlsruhe, Germany
[5] Fraunhofer Institute for Applied Solid State Physics (IAF), 79108 Freiburg, Germany

Future wireless communication networks need to handle data rates of tens or even hundreds of Gbit/s per link, requiring carrier frequencies in the unallocated terahertz (THz) spectrum [58], [59]. In this context, seamless integration of THz links into existing fiber-optic infrastructures [60] is of great importance to complement the inherent portability and flexibility advantages of wireless networks by the reliable and virtually unlimited capacity of optical transmission systems. On the technological level, this requires novel device and signal processing concepts for direct conversion of data streams between the THz and the optical domains. Here, we report on the first demonstration of a THz link that is seamlessly integrated into a fiber-optic network using direct terahertz-to-optical (T/O) conversion at the wireless receiver. We exploit an ultra-broadband silicon-plasmonic modulator having a 3 dB bandwidth in excess of 0.36 THz for T/O conversion of a 50 Gbit/s data stream that is transmitted on a 0.2885 THz carrier over a 16 m-long wireless link. Optical-to-terahertz (O/T) conversion at the wireless transmitter relies on photomixing in a uni-travelling-carrier photodiode.

3.1 Introduction

Data traffic in wireless communication networks is currently experiencing explosive growth [61] and will account for more than 60 % of the overall internet traffic by 2021. In order to cope with the associated capacity challenges, wireless communication networks need to exploit frequency windows of low atmospheric attenuation in the unallocated THz spectrum beyond [58] 0.275 THz.

Moreover, future wireless links have to be intimately integrated into the fiber-optic infrastructures, for example in terahertz-over fiber (ToF) [60] or fiber-to-the-antenna (FTTA) [62] architectures. This requires seamless connection of optical fibers to THz transmitter (Tx) and receiver (Rx) front-ends.

At the THz Tx, optoelectronic down-conversion of data streams from the optical to the THz domain has been demonstrated to offer a variety of advantages [58] over conventional all-electronic approaches. These advantages include wide-band tunability of the THz carrier frequency and the ability to capitalize on advanced optical circuitry for generation and multiplexing of data streams prior to conversion to the THz domain. Wireless transmission with data rates of 100 Gbit/s or more have previously been demonstrated [63]–[65] by direct optical-to-THz (O/T) conversion of a wavelength-division multiplexing signal in an ultra-fast uni-travelling-carrier [66] (UTC) photodiode. In contrast to that, direct conversion of data signals from the THz-to-optical (T/O) domain at the receiver has not yet been demonstrated, and previous transmission experiments [63]–[65], [67]–[69] still rely on all-electronic down-conversion [58] of the signals to the baseband using, e.g., sub-harmonic mixers [70] or Schottky diodes [71].

In this letter, we report on the first demonstration of a THz wireless link that is seamlessly integrated into a photonic network, complementing direct O/T conversion at the THz Tx by direct T/O conversion at the THz Rx. The wireless link operates at a carrier frequency of 0.2885 THz with a maximum line rate of 50 Gbit/s and bridges a distance of 16 m. The THz signal is generated by O/T conversion in a UTC photodiode. At the receiver, the THz signal is converted to the optical domain by using an ultra-broadband plasmonic-organic hybrid (POH) modulator. The POH modulator features a flat frequency response [72], [73] up to 0.36 THz along with small footprint of about 600 μm^2, thus lending itself to high-density photonic integration. To the best of our knowledge, this is the first demonstration of direct conversion of a THz wireless data signal to the optical domain without prior down-conversion to the baseband or to an intermediate frequency. We expect that the combination of direct O/T and T/O conversion in ultra-compact devices has the potential to greatly accelerate THz communications and to advance the integration of THz wireless links into fiber-optic infrastructures.

3.2 Integration of THz links with fiber-optic infrastructures

The concept, presented in Fig. 3.1(a), relies on distributed THz transceiver (TRx) front-ends that are connected to powerful centralized digital signal processing (DSP) sites through widely deployed fiber-optic network infrastructures that exploit optical carriers to efficiently carry data signals over large distances. The architecture relies on direct O/T and T/O conversion at the TRx front-end, which is key to efficiently interface optical fibers to THz antennae. Direct conversion between analogue optical signals and THz waveforms considerably reduces complexity at the antenna site and improves scalability to a large number of geographically distributed high-performance THz links or cellular networks.

Similarly, the concept of moving computationally expensive digital processing of baseband (BB) signals to centralized sites such as large-scale data centers offers unprecedented network scalability, flexible and efficient sharing of crucial resources as well as improved network resilience. Seamless combination of short-reach THz links with long-reach fiber-optic networks may thus represent a key step towards overcoming the capacity bottlenecks in wireless communication infrastructures. Note that the scheme presented here is mainly geared towards wireless THz connections between fixed transmitter and receiver stations rather than towards serving mobile terminals, for which steered THz beams would be required.

At its heart, the architecture depicted in Fig. 3.1(a) relies on THz transmitter (Tx) and receiver (Rx) front-ends that allow for direct conversion between optical and THz signals. The underlying concepts are illustrated in Fig. 3.1(b) and (c). After generating the analogue baseband waveform of the data signal at the DSP site, it is modulated onto an optical carrier at frequency f_0 by an optical transmitter (Opt. Tx) and then sent to the THz Tx through a fiber-optic network. At the THz Tx, see Fig. 3.1(b), the optical signal is then converted to a THz waveform by photomixing with a continuous-wave (CW) local oscillator (LO) tone at frequency $f_{\mathrm{Tx,LO}}$ in a UTC photodiode, see Inset of Fig. 3.1(b). The THz data signal, centered at the difference frequency $f_{\mathrm{THz}} = \left| f_{\mathrm{Tx,LO}} - f_0 \right|$, is then transmitted into free-space by an antenna. At the T/O converter, Fig. 3.1(c), the THz data signal is received by another antenna and fed to a THz amplifier. For

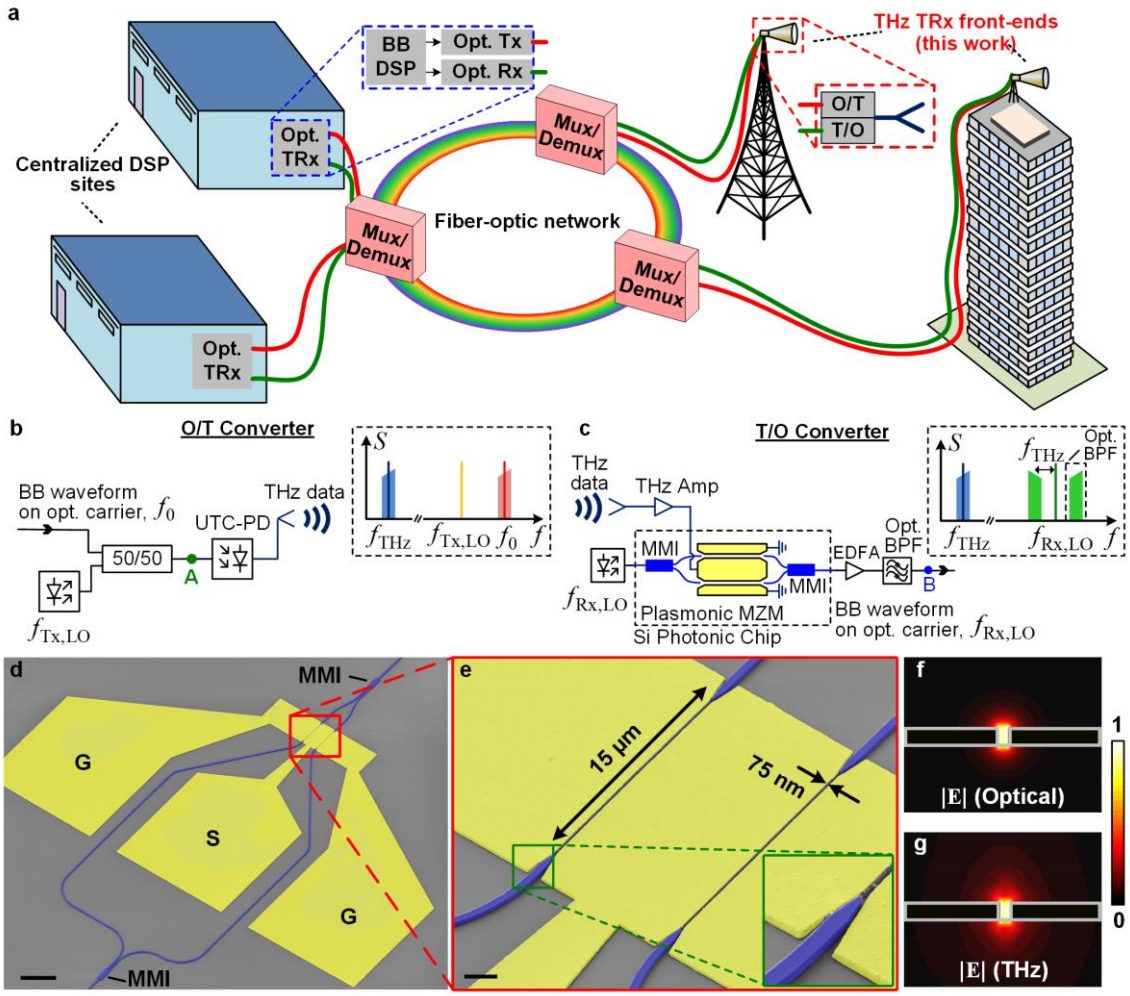

Figure 3.1: Seamless integration of THz wireless links into fiber-optic infrastructures by direct optical-to-THz (O/T) and THz-to-optical (O/T) conversion. **(a)** Vision of a future communication network architecture that combines geographically distributed analogue THz transceiver (TRx) front-ends with powerful centralized digital signal processing (DSP) sites through fiber-optic network infrastructures. Our work focusses on direct T/O and O/T conversion of analogue waveforms at the THz front-end, which allows to efficiently interface optical fibers to THz antennae. This considerably reduces complexity at the antenna site and improves scalability to a large number of THz links or cellular networks. The envisaged concept may thus represent a key step towards overcoming the capacity bottlenecks in wireless communication infrastructures. **(b)** Concept of direct O/T conversion: The baseband (BB) waveform is first modulated onto an optical carrier at frequency f_0 . and sent to the O/T converter. The optical signal is then translated to a THz carrier by photomixing with a continuous-wave (CW) local oscillator (LO) laser tone at a frequency $f_{Tx,LO}$ in an ultra-fast uni-travelling-carrier photodiode (UTC-PD). The THz data signal is radiated into free-space by an antenna. The inset shows the optical data spectrum (center frequency f_0), the LO tone (frequency $f_{Tx,LO}$), and the THz spectrum (center frequency f_{THz}) after O/T conversion. **(c)** Concept of direct T/O conversion: The THz data signal is received by an antenna, amplified by a THz amplifier, and then fed to

a plasmonic Mach-Zehnder modulator (MZM) for modulation onto a CW carrier at optical frequency $f_{\mathrm{Rx,LO}}$. After modulation, the optical signal from the MZM contains an upper and a lower modulation sideband. An optical band-pass filter (BPF) is used to suppress the carrier and to select one of the modulation sidebands. The inset depicts an illustration of the spectrum of the THz signal (carrier frequency f_{THz}) along with the optical LO tone (frequency $f_{\mathrm{Rx,LO}}$) and the optical signal sidebands generated by THz modulation. The BPF is configured to select one of the sidebands (center frequency $f_{\mathrm{Rx,LO}} + f_{\mathrm{THz}}$). **(d)** False-colored scanning electron microscope (SEM) image of a plasmonic MZM with ground-signal-ground (GSG) contact pads (yellow) and integrated silicon photonic waveguides (blue). Scale bar – 20 µm. **(e)** Zoom-in of the plasmonic section of the MZM showing two 15 µm-long phase modulators with photonic-to-plasmonic mode converters (see *Inset*). Scale bar – 2 µm. Each section consists of a plasmonic slot waveguide, featuring a 75 nm-wide gap between two extended gold pads (yellow). (**f, g)** Field profile of the optical quasi-TE mode and the THz field respectively. Both figures indicate the magnitudes of the complex electric field vectors. It can be noticed that the optical and the electronic modes are tightly confined to the slot region, thereby ensuring strong interaction and efficient modulation

conversion to an optical carrier, the amplified signal is then coupled to a plasmonic-organic hybrid [33]–[35], [74]–[77] (POH) Mach-Zehnder modulator (MZM), which is fed by an optical carrier at frequency $f_{\mathrm{Rx,LO}}$. The POH MZM generates an upper and a lower modulation sideband. An optical band-pass filter (BPF) is used to suppress the carrier and to select one of the modulation sidebands, see Inset of Fig. 3.1(c). This scheme allows for operation over a wide range of THz frequencies, and does not require any down-conversion to an intermediate frequency before encoding the data onto an optical carrier, and hence considerably reduces the complexity at the THz front-end. After T/O conversion, the analogue signal is sent back through fiber-optic network to an optical receiver (Opt. Rx) in the centralized DSP site. The scheme illustrated in Fig. 3.1(c) crucially relies on ultra-broadband electro-optic modulators, offering modulation bandwidths that extend into the THz spectrum.

3.3 Bandwidth measurement of POH MZM

High-speed MZM have previously been demonstrated using lithium niobate as the electro-optic medium – either as bulk material [78] or as thin films on silicon [17] or quartz [79] substrates. However, these devices are usually realized in travelling-wave configuration with typical device lengths on the millimeter or

centimeter scale, which is not well suited for high-density integration. Moreover, while some lithium niobate devices show measureable sidebands up to modulation frequencies [79] of 0.5 THz, the underlying 3 dB bandwidths [17], [78], [79] are so far limited to approximately 0.1 THz. These bandwidth limitations can be overcome by plasmonic-organic hybrid modulators [33]–[35], [74]–[77] that combine organic electro-optic (EO) materials with ultra-compact plasmonic slot waveguides [80]–[82]. The POH concept allows to considerably reduce the device footprint and offers a route towards high-density co-integration [76] with advanced silicon photonic circuitry [11], [83]. A fabricated POH MZM is shown in the false-colored scanning electron microscope (SEM) image in Fig. 3.1(d). Light is coupled to the silicon photonic (SiP) chip via on-chip grating couplers (not shown) and propagates in silicon strip waveguides (blue) as a quasi-transverse electric (quasi-TE) mode. A multimode interference (MMI) coupler splits the light from the input waveguide and launches it into the two arms of an unbalanced MZM. An MMI coupler at the other end of the MZM combines the modulated signals into an output waveguide which is connected to another grating coupler. Each arm of the MZM contains a POH phase modulator section comprising a narrow metallic slot (width w = 75 nm) between the gold electrodes (yellow), see Fig. 3.1(e). A pair of tapered silicon waveguides in each arm is used to convert [84] the photonic mode of the silicon strip waveguide to the surface plasmon polariton (SPP) mode in the metallic slot waveguide and vice versa, see Inset of Fig. 3.1(e). The slots are filled with the organic EO material [85] SEO100. A THz signal applied to the ground-signal-ground (GSG) contacts of the POH MZM leads to a THz electric field in the slots of each of the two arms and thus creates an optical phase shift. Fig. 3.1(f) and (g) show that both the optical quasi-TE field and the THz electric field are tightly confined to the metallic slot waveguide, leading to a strong overlap and a high modulation efficiency. The MZM is configured to operate in push-pull mode with phase shifts of equal magnitude but opposite signs in each arm. This is accomplished by an appropriate choice of the poling directions [36] of the EO material with respect to the modulating THz field inside the two slot waveguides.

Due to the strong interaction of the THz field and the optical field in the metallic slot waveguide, POH phase shifters can be very short. This leads to ultra-small parasitic capacitances of the order of a few fF, thereby permitting theoretical

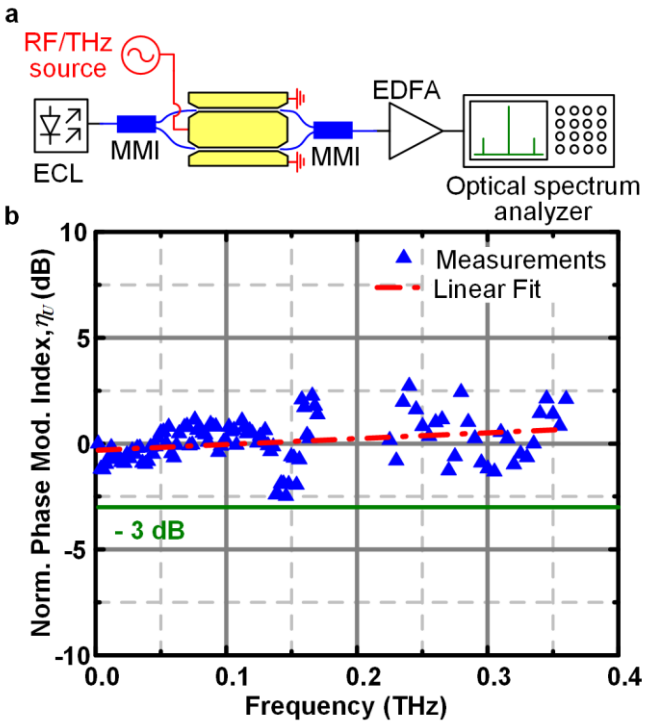

Figure 3.2: Bandwidth measurement of POH modulator. **(a)** Experimental setup for measuring the frequency-dependent phase modulation index η of the POH MZM. CW light from an external-cavity laser (ECL) is coupled to the modulator, which is driven by a RF/THz signal. The resulting optical spectrum is recorded by an optical spectrum analyzer and the phase modulation index is extracted from the power ratio of the modulation sidebands and the CW carrier. **(b)** Frequency dependence of the normalized modulation index η_U according to Eq. (3.1). The POH MZM features an ultra-broad frequency response up to at least 0.36 THz and shows no indication of a bandwidth limitation. The gap around between 0.17 THz and 0.22 THz is due to the lack of a signal source in this frequency range.

RC cutoff frequencies in excess of 1 THz when connected to a signal source with a 50 Ω internal impedance [34], [36]. For our experiments, we fabricated a 15 µm-long POH MZM with a slot width of 75 nm and characterized its response over an extended frequency range of up to 0.36 THz, limited by the signal sources available in our lab. Fig. 3.2(a) shows the basic setup for the bandwidth measurement. The optical CW carrier at a frequency f_c is derived from an external-cavity laser (ECL) and launched into the POH MZM that is driven by a small sinusoidal RF or THz signal with varying drive frequency f_m. The intensity-modulated optical signal is then amplified by an erbium-doped fiber amplifier (EDFA) and detected by an optical spectrum analyzer to evaluate the phase modulation index $\eta(f_m)$. Due to the small electrical drive powers of the

THz sources in combination with the comparatively high insertion loss of the specific POH MZM used in our experiments, an EDFA was necessary to boost the optical output power for these measurements. The EDFA could be omitted for later device generations with reduced insertion loss, see Appendix A.2 for details. For each drive frequency, the optical spectrum exhibits a peak at f_c along with two first-order sidebands at $f_\mathrm{c} \pm f_\mathrm{m}$. Assuming that the MZM is biased at its quadrature (3 dB) point and that both arms of the MZM have the same phase modulation index η, the sideband-to-carrier power ratio $R_{1,0}$ allows to calculate η according to the relation [86] $R_{1,0} \approx \eta^2/4$ for small amplitude of the drive signal $(\eta \ll 1)$, see Appendices A.1 and A.2 for more details. Note that the electric drive power P_e provided by our signal source shows a strong dependency on the modulation frequency f_m. Since the phase modulation index η is proportional to the electric drive voltage U_e, we can eliminate the impact of the frequency-dependent drive power $P_\mathrm{e}(f_\mathrm{m})$ by considering the ratio $\eta(f_\mathrm{m})/U_\mathrm{e}(f_\mathrm{m})$. Normalizing the frequency characteristic of this ratio to its value at a reference modulation frequency of $f_\mathrm{m,ref} = 2\,\mathrm{GHz}$, we obtain the dimensionless normalized phase modulation index

$$\eta_U(f_\mathrm{m}) = 20\log_{10}\left(\frac{\eta(f_\mathrm{m})/U_\mathrm{e}(f_\mathrm{m})}{\eta(f_\mathrm{m,ref})/U_\mathrm{e}(f_\mathrm{m,ref})}\right). \tag{3.1}$$

Raw data and details on the evaluation can be found in the Appendix A.2. The results obtained for our 15 µm-long POH MZM are shown in Fig. 3.2(b). The device features a flat frequency response over the entire measurement range with no indication of any frequency-dependent decay. The noticeable variations of approximately $\pm 2.5\,\mathrm{dB}$ in the frequency response are attributed to uncertainties of our measurement technique and do not represent an intrinsic property of the POH MZM, see Appendix A.2 for details.

The experimental results hint to a 3 dB bandwidth that is significantly larger than the highest measured frequency of 0.36 THz. To the best of our knowledge, this represents the fastest EO modulator that has so far been published. Our findings are well in line with earlier demonstrations of POH modulators, where operation up to frequencies of 0.17 THz has been shown [77]. Note that POH devices are not limited to gold as a plasmonic material, but may also be realized

by employing CMOS compatible materials [87], which would allow for co-integration with silicon-based electronics.

3.4 Direct THz-to-optical conversion

For the THz wireless transmission experiments, we use a second-generation device with slightly longer phase shifter sections (20 µm instead of 15 µm) featuring a slot width of 75 nm and the same electro-optic material (SEO100) as the cladding. For this device, we measure an EO figure-of-merit (FoM) of $n_{\mathrm{EO}}^3 r_{33} = 315\,\mathrm{pm/V}$, leading to an estimated EO coefficient of $r_{33} = 64\,\mathrm{pm/V}$. Note that there is vast room to further improve the EO FoM and to hence reduce the drive voltage requirement by using more efficient EO materials. As an example, EO FoM values of $n_{\mathrm{EO}}^3 r_{33} = 1990\,\mathrm{pm/V}$ (calculated for $n_{\mathrm{EO}} = 1.83$ and $r_{33} = 325\,\mathrm{pm/V}$) have been previously demonstrated in POH devices [88], and even higher values of $n_{\mathrm{EO}}^3 r_{33} = 2300\,\mathrm{pm/V}$ ($r_{33} = 390\,\mathrm{pm/V}$ for $n_{\mathrm{EO}} = 1.81$) have been recently achieved in silicon-organic hybrid (SOH) modulators [28]. Moreover, the plasmonic losses of the modulator can be greatly reduced by, e.g., using silver for the plasmonic slot waveguide. Together with the highly efficient EO polymers, this may lead to more than a 25-fold improvement in the π-voltage-loss product of the POH MZM, see Appendices A.6 and A.7 for more details.

Figure 3.3(a) shows photographs of the experimental setups used for the transmission experiment. The THz Tx comprises a high-speed UTC photodiode with a horn antenna to generate the THz signal as well as a plano-convex polytetrafluoroethylene (PTFE) lens that collimates the THz beam. After travelling over a free-space distance of approximately 16 m, the THz signal is coupled to the POH MZM (not shown) through a second lens, a horn antenna, and a two-stage THz amplifier. A more detailed description of the THz components and a technical sketch of the experimental setup can be found in Appendices A.3 and A. respectively. In the transmission experiment, a quadrature phase-shift keying (QPSK) data stream at a symbol rate of 15 GBd is encoded on an optical carrier at $f_0 = 193.3\,\mathrm{THz}$ and superimposed with a CW LO tone at $f_{\mathrm{Tx,LO}}$. Photomixing in the UTC photodiode is used to transfer the optical data stream to a THz

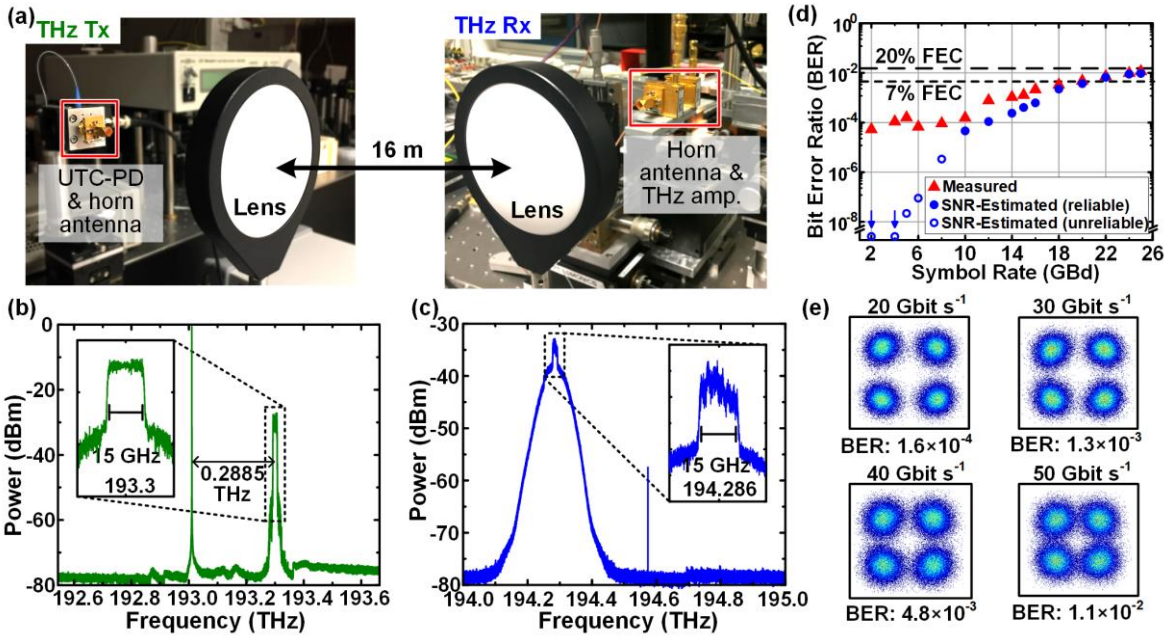

Figure 3.3: Demonstration of THz wireless data transmission using direct O/T and T/O conversion. (a) Photograph of the THz transmitter (Tx) and receiver (Rx) setup, separated by a distance of 16 m. The THz Tx comprises a high-speed UTC photodiode (UTC-PD), a horn antenna, and a plano-convex polytetrafluoroethylene (PTFE) lens that collimates the THz beam. After travelling over a free-space distance of approximately 16 m, the signal is coupled to the POH MZM through a second lens, a horn antenna, and a two-stage THz amplifier. A more detailed description and a technical sketch of the data transmission setup can be found in Appendix A.4 and in Fig. A.7. **(b)** Optical spectrum measured at position 'A' of the THz Tx shown in Fig. 3.1(b). The spectrum consists of a 15 GBd QPSK data signal (inset) at a carrier frequency of 193.3 THz and a CW tone, detuned from the carrier of the data signal by the targeted THz carrier frequency of 0.2885 THz. The THz signal is generated by photomixing in an UTC photodiode. **(c)** Filtered optical spectrum measured at position 'B' of the THz Rx, see Fig. 3.1(c). Upon modulating the THz signal onto the optical carrier, the upper sideband and the carrier are suppressed by an optical band pass filter such that only the lower sideband and the residual carrier are visible. The lower sideband contains a 15 GBd QPSK signal (inset) centered at 194.286 THz. **(d)** Bit error ratios (BER) of QPSK signals at different symbol rates upon T/O conversion and coherent intradyne detection. Red triangles represent measured BER obtained from 10^5 symbols of the received signal. Filled blue circles represent the BER estimated from the signal-to-noise power ratio (SNR) in the signal bandwidth. For $\mathrm{BER} < 10^{-5}$ this estimate becomes increasingly unreliable – the associated BER values are indicated by blue open circles. The measured BER for higher symbol rates $(> 8\,\mathrm{GBd})$ fit well to the estimations. For lower symbol rates, the measured BER differs strongly from the (unreliable) estimations due to phase noise of the LO laser in the coherent optical receiver and due to nonlinear distortions caused by the THz amplifiers, see Appendix A.5 for details. The BER stays below the 7 % hard-decision forward error correction (FEC) limit up to a symbol rate of 18 GBd. Higher

symbol rates require 20 % soft-decision FEC. **(e)** Constellation diagrams of the received QPSK signal for data rates of 20 Gbit s^{-1}, 30 Gbit s^{-1}, 40 Gbit s^{-1}, and 50 Gbit s^{-1}.

carrier frequency of $f_{\mathrm{Tx,THz}} = \left| f_0 - f_{\mathrm{Tx,LO}} \right| = 0.2885\,\mathrm{THz}$. Fig. 3.3(b) shows the optical spectrum at the input of the UTC photodiode, marked as position 'A' in Fig. 3.1(b). At the THz Rx, the received signal is boosted by two cascaded THz amplifiers to drive the POH MZM via a ground-signal-ground (GSG) probe with a hollow-core waveguide. The amplifiers are based on millimeter-wave monolithic integrated circuits (MMIC) and feature a total gain of approximately 40 dB for frequencies between 0.270 THz and 0.310 THz, see Appendix A.3 for details. The POH MZM is biased at its quadrature (3 dB) point and hence imposes an intensity modulation on the CW carrier at $f_{\mathrm{Rx,LO}} = 194.57\,\mathrm{THz}$ obtained from another ECL. The optical data signal is amplified by erbium-doped fiber amplifiers (EDFA) and sent through an optical filter which suppresses the carrier at $f_{\mathrm{Rx,LO}}$ along with the upper modulation sideband. The corresponding spectrum taken after the optical filter, i.e., at position 'B' in Fig. 3.1(c), is displayed in Fig. 3.3(c). The optical QPSK signal is detected and evaluated using an optical modulation analyzer with an in-built optical LO for coherent intradyne reception. Note that intensity-modulating a THz QPSK signal onto an optical carrier and selective filtering of one of the sidebands generates an optical QPSK signal even though the THz Rx contains only a simple MZM. Note also that, due to the limited tuning range of the optical filter, we chose to isolate the lower sideband of our optical signal rather than the upper one, as sketched in Fig. 3.1(c).

The QPSK data signal is analyzed offline using standard DSP techniques and the bit error ratio (BER) is extracted. Fig. 3.3(d) shows the BER as a function of the QPSK symbol rate, where the red triangles indicate the measured BER, while the filled blue circles correspond to the estimated BER from the signal-to-noise power ratio (SNR) of the T/O converted signal. This estimate becomes unreliable for $\mathrm{BER} < 10^{-5}$ which are represented by blue open circles, see Appendix A.5 for more details. Up to 18 GBd (line rate 36 Gbit s^{-1}), the BER stays below the 7 % hard-decision forward error correction (FEC) limit [89], while we have to resort to a 20 % soft-decision FEC for higher data rates. For higher symbol rates, the BER agrees well with estimations from the SNR, and is mainly limited by the amplified spontaneous emission (ASE) noise of the first EDFA

after the POH MZM [EDFA 1 in Appendix A Fig. A.7(b)]. For smaller symbol rates, however, the measured BER differs greatly from the SNR-based (unreliable) estimations due to phase noise of the LO laser in the coherent optical receiver and due to nonlinear distortions caused by the THz amplifiers, see Appendix A.5 for a detailed analysis. Fig. 3.3(e) shows the QPSK constellations for line rates of 20 Gbit s^{-1}, 30 Gbit s^{-1}, 40 Gbit s^{-1} and, 50 Gbit s^{-1} respectively. To the best of our knowledge, this experiment corresponds to the first demonstration of data transmission using direct THz-to-optical conversion.

3.5 Summary

In summary, we have demonstrated an optical-wireless-optical link with purely optoelectronic frequency conversion both at the THz transmitter and the THz receiver. The link spans a distance of 16 m and is operated at a carrier frequency of 0.2885 THz. Key for this demonstration is a compact ultra-broadband POH modulator offering an ultra-high modulation bandwidth of at least 0.36 THz. With a 20 % soft-decision FEC, we achieve a fiber-to-fiber line rate of 50 Gbit s^{-1}. In our current experiments, the transmission distance is limited to 16 m due to the width of our building. Further device improvements will allow to extend the scheme to transmission distances of 1 km or more, while still maintaining a reasonable loss margin, see Appendix A.7 for more details. These results demonstrate the prospects of POH modulators as powerful subsystems for THz receiver front-ends. Such devices lend themselves to co-integration with the full portfolio of silicon photonic components that have emerged over recent years[83], possibly complemented by silicon-based nano-electronic devices[11]. We believe that direct T/O conversion at the Rx can boost terahertz wireless links to data rates of hundreds of gigabit per second.

[End of paper [J3]]

4 Horizontal-slot POH modulator

This chapter presents a novel architecture of POH modulators with horizontal plasmonic slot waveguides to improve the fabrication tolerance as well as the efficiency of conventional POH modulators. The chapter is taken from a conference publication [C1] presented in CLEO 2020. The contents of the conference publication is modified and adapted to fit the structure and layout of this thesis.

For this publication, Sandeep Ummethala (S.U.) developed the concept and designed the modulators with support from Venkata Anirudh Pammi and Ahsan H. M. Uddin. S.U. fabricated the devices with support from Lothar Hahn. S.U. performed the experiments and analyzed the data. The work was supervised jointly by Wolfgang Freude (W.F.) and Christian Koos (C.K.). S.U., W.F., and C.K. wrote the paper. All authors revised the paper.

[Start of paper [C1]]

Horizontal-Slot Plasmonic-Organic Hybrid (POH) Modulator

Conference on Lasers and Electro-Optics (CLEO) 2020,

S. Ummethala[1,2], V. A. Pammi[1], A. H. M. Uddin[1], L. Hahn[2], W. Freude[1], C. Koos[1,2]

[1] Institute of Photonics and Quantum Electronics (IPQ), Karlsruhe Institute of Technology (KIT), 76131 Karlsruhe, Germany

[2] Institute of Microstructure Technology (IMT), Karlsruhe Institute of Technology (KIT), 76334, Eggenstein-Leopoldshafen, Germany

We demonstrate horizontal-slot plasmonic-organic hybrid (HS-POH) modulators and show that the π-voltage-loss product $aU_{\pi}L$ is by 25 % better than for conventional vertical-slot devices. The slot is realized by a sacrificial layer, thereby relaxing extreme lithography-resolution requirements.

4.1 Introduction

Plasmonic-organic hybrid (POH) electro-optic modulators combine plasmonic slot waveguides with highly efficient organic electro-optic (EO) materials [90] to achieve high modulation efficiencies. The devices offer ultra-small footprint and lend themselves to co-integration with low-loss silicon photonic circuits [75]. As a prominent feature, POH modulators provide unprecedented EO bandwidths of hundreds of GHz [55], [91], thereby opening a route towards seamless conversion of data signals from THz carriers to optical carriers [55]. However, the practical application of POH modulators is still subject to various limitations. POH devices suffer from comparatively high propagation losses of the plasmonic slot waveguides, thereby limiting the interaction length and increasing the required modulation voltage. This effect is quantified by the π-voltage-loss product $aU_\pi L$, i. e., by the product of required π-voltage U_π measured in V and the phase-shifter insertion loss aL in dB. Moreover, conventional POH modulators rely on precise fabrication of high aspect-ratio plasmonic slot waveguides using high-resolution lithography in combination with a sensitive lift-off process. Mitigation of these challenges would be an important step towards practical application of POH devices.

In this chapter, we demonstrate a novel structure for POH electro-optic modulators, exploiting a horizontally oriented plasmonic slot. In contrast to lithographically defined conventional vertical-slot plasmonic waveguides, the basic structure of horizontal-slot POH (HS-POH) modulators is realized by spin-coating a thin sacrificial layer which allows to precisely adjust the slot dimensions, even without using high-resolution lithography. We demonstrate HS-POH modulators with slot aspect ratios of more than 5, which allows decreasing the π-voltage-length product $U_\pi L$ by more than 40 % in comparison to the vertical-slot structures. Based on electro-magnetic simulations, we show that the HS-POH configuration can reduce the π-voltage-loss product $aU_\pi L$ by more than 25 %. In addition, because the plasmonic section is side-coupled to silicon photonic strip waveguides, alignment tolerances can be relaxed without significantly affecting the coupling efficiency.

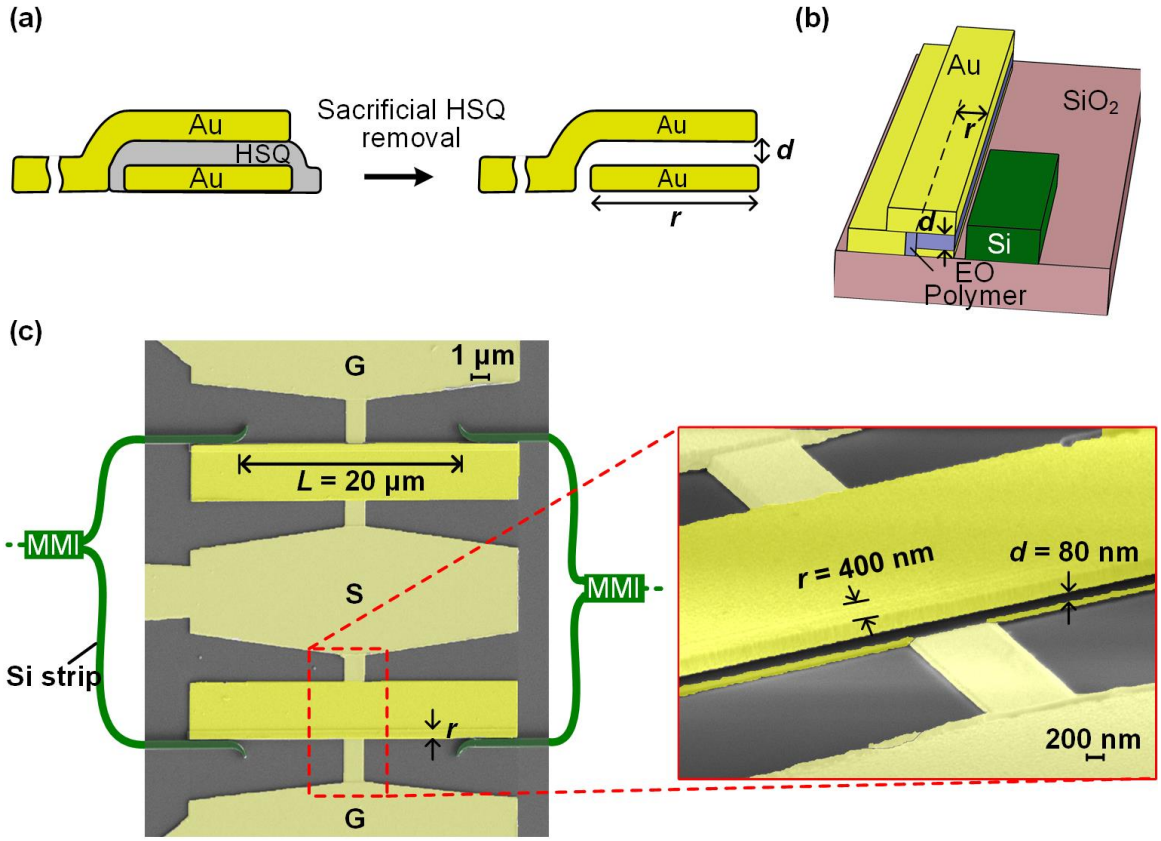

Figure 4.1: **(a)** Horizontal-slot plasmonic waveguide fabricated by using a sacrificial layer of HSQ resist. **(b)** Photonic-to-plasmonic converter with directional coupler comprising a Si strip and a horizontal-slot plasmonic waveguide. **(c)** False-colored micrograph of HS-POH MZM showing GSG contact pads. The inset shows the gold rails with r = 400 nm separated by d = 80 nm.

4.2 Horizontal-slot POH (HS-POH) Mach-Zehnder modulator

The cross-section of a horizontal plasmonic waveguide, see Fig. 4.1(a), shows a sacrificial layer of patterned hydrogen silsesquioxane (HSQ) resist between two gold (Au) rails. When the HSQ layer is removed, the rails form a horizontal plasmonic slot waveguide. The use of HSQ allows for precise control of the spacing d between the metal rails (width r) that form the horizontal plasmonic slot. In contrast to conventional vertical-slot POH (VS-POH) modulators, where the slot is defined by lithographic structuring and subsequent lift-off using a

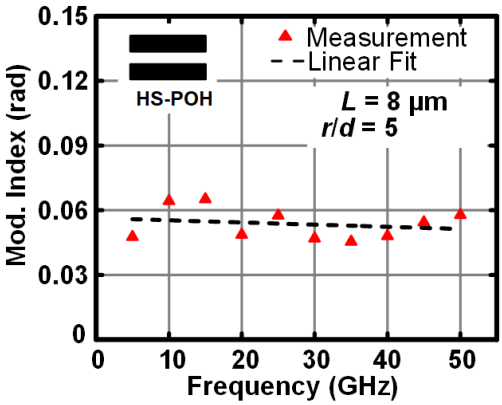

Figure 4.2: Frequency response of the modulation index of the horizontal-slot plasmonic-organic hybrid (HS-POH) MZM.

poly-methyl methacrylate (PMMA) mask, the HS-POH structure gives better control over the metal spacing *d* and the flatness of the metal rails. Specifically, this configuration allows realizing plasmonic slot waveguides having significantly larger aspect ratios *r* / *d* than those that are possible with conventional VS-POH devices where the aspect ratio is limited to about 3. In the case of horizontal-slot plasmonic waveguides, the maximum possible aspect ratio is limited only by the stability of the mechanical structure; an aspect ratio of 12 is feasible.

The plasmonic slot is filled with an EO polymer and guides a surface plasmon polariton (SPP). Light is coupled into the slot waveguide using a directional coupler section comprising a silicon (Si) strip waveguide in close proximity to the horizontal plasmonic slot, see Fig. 4.1(b). The Si waveguide carries a quasi-transverse-magnetic (TM) mode. By appropriately choosing the length of the directional coupler, a coupling efficiency of up to 90 % is possible [92]. Such a side-coupling scheme for photonic-to-plasmonic mode conversion relaxes the alignment tolerances greatly. A false-colored micrograph of an HS-POH Mach-Zehnder modulator (MZM) is shown in Fig. 4.1(c). Light is coupled in and out of the on-chip silicon photonic waveguides (green, width 500 nm, height 220 nm) via grating couplers (not shown), and a multi-mode interference (MMI) coupler is used to split the light to the two arms of the MZM. A geometrical path length difference of 80 µm between the MZM arms allows for the

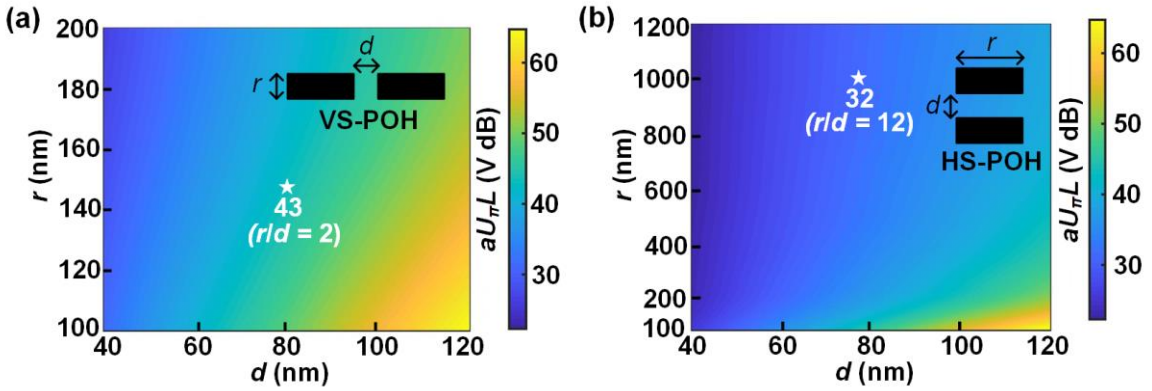

Figure 4.3: Color-coded π-voltage-loss product $aU_\pi L$ (in V dB) of **(a)** vertical-slot POH modulator and **(b)** horizontal-slot POH modulators as a function of *d* and *r*.

selection of the operating point by tuning the wavelength. The RF signal is applied across the metal pads (dark yellow) with a ground-signal-ground (GSG) probe. Each arm of the MZM contains a phase-shifter section comprising two gold electrodes (bright yellow) with a rail width r = 400 nm, which are separated by a distance d = 80 nm, see Fig. 4.1(c) and inset. After fabrication of the HS-POH MZM, the metal slots are filled with an organic EO polymer (SEO100) having a bulk EO coefficient r_{33} of 166 pm/V. For an L = 20 µm long HS-POH MZM, we measure an insertion loss of 31 dB and an extinction ratio of more than 20 dB. From dedicated cut-back measurements, we calculate a plasmonic loss of 1 dB/µm, a loss of 3.2 dB per mode converter, and a loss of 4.5 dB for the passive waveguides and MMIs.

For a VS-POH modulator with d = 80 nm and an aspect ratio r / d = 1.9, see inset Fig. 4.3(a), we measure $U_\pi = 12.6\,\mathrm{V}$, which reduces by 40 % to $U_\pi = 7.6\,\mathrm{V}$ for an HS-POH modulator with the same d but an aspect ratio of r / d = 5, see inset Fig. 4.1(e). Figure 4.2 shows a flat frequency response of an L = 8 µm long HS-POH MZM up to 50 GHz (limited by the presently available equipment), emphasizing the broadband characteristics of POH modulators. Using an electro-magnetic simulation tool, we calculate $aU_\pi L$ values for different geometrical variations of VS-POH and HS-POH modulators, see Figs. 4.3(a) and (b). For d = 80 nm, the π-voltage-loss product can be reduced by 25 % from 43 V dB to 32 V dB by increasing the aspect ratio r / d from 2 for a vertical slot to 12 for a horizontal slot. The values of the $aU_\pi L$ products specified here are limited by the rather moderate EO coefficient r_{33} = 160 pm/V assumed in the

calculations. By using more efficient EO materials [28] with r_{33} values of 390 pm/V, $aU_{\pi}L$ products down to 13 V dB can be achieved.

4.3 Summary

We realized a novel structure for POH electro-optic modulators, exploiting a horizontally oriented plasmonic slot. The concept stands out due to the significantly simplified fabrication process that requires neither high-resolution lithography nor a sensitive lift-off process. HS-POH modulators can be realized with large slot aspect ratios, thereby strongly reducing the π-voltage-loss product. We believe this robust design for POH modulators is a key step towards practical application of the devices.

[End of paper [C1]]

5 Capacitively-coupled SOH modulator

The current chapter discusses the novel concept of capacitively-coupled SOH (CC-SOH) modulators and presents a proof-of-concept CC-SOH Mach-Zehnder modulator that overcomes the bandwidth limitations of the conventional resistively-coupled SOH (RC-SOH) modulators. This chapter is taken from an article [J1] published in Optica. The contents of the journal submission are adapted to fit the structure and layout of this thesis. The associated Supplementary Information of the article can be found in Appendix B.

For this publication, Sandeep Ummethala (S.U.), Matthias Lauermann, Wolfgang Freude (W.F.) and Christian Koos (C.K.) developed the concept and designed the experiment. S.U. and Ahmed Shariful Alam designed the modulators and fabricated them with support from Sree Harsha Nandam and Lothar Hahn. S.U. performed the experiments and analyzed the data together with Juned Kemal and Artem Kuzmin. S.U. developed the poling procedure with support from Yasar Kutuvantavida. Delwin L. Elder and Larry R. Dalton developed the EO material. The work was supervised jointly by Thomas Zwick. Sebastian Randel, W.F., and C.K. S.U., W.F., and C.K. wrote the paper. All authors revised the paper.

[Start of paper [J1]]

Hybrid Electro-Optic Modulator Combining Silicon Photonic Slot Waveguides with High-k Radio-Frequency Slotlines

Optica, 8(4), 2021, pages: 511-519
DOI: 10.1364/OPTICA.411161

S. Ummethala[1,2], J. N. Kemal[1], A. S. Alam[1], M. Lauermann[1], Y. Kutuvantavida[1,2], A. Kuzmin[3], S. H. Nandam[4], L. Hahn[2], D. L. Elder[5], L. R. Dalton[5], T. Zwick[6], S. Randel[1], W. Freude[1], C. Koos[1,2]

[1] Institute of Photonics and Quantum Electronics (IPQ), Karlsruhe Institute of Technology (KIT), 76131 Karlsruhe, Germany

[2] Institute of Microstructure Technology (IMT), Karlsruhe Institute of Technology (KIT), 76334, Eggenstein-Leopoldshafen, Germany

[3] Karlsruhe Institute of Technology (KIT), Laboratory for Applications of Synchrotron Radiation (LAS), 76131 Karlsruhe, Germany
[4] Institute of Nanotechnology (INT), Karlsruhe Institute of Technology (KIT), 76334, Eggenstein-Leopoldshafen, Germany
[5] University of Washington, Department of Chemistry, Seattle, Washington 98195, USA
[6] Institute of Radio Frequency Engineering & Electronics (IHE), Karlsruhe Institute of Technology (KIT), 76131 Karlsruhe, Germany

Electro-optic (EO) modulators rely on the interaction of optical and electrical signals with second-order nonlinear media. For the optical signal, this interaction can be strongly enhanced by using dielectric slot-waveguide structures that exploit a field discontinuity at the interface between a high-index waveguide core and the low-index EO cladding. In contrast to this, the electrical signal is usually applied through conductive regions in the direct vicinity of the optical waveguide. To avoid excessive optical loss, the conductivity of these regions is maintained at a moderate level, thus leading to inherent *RC*-limitations of the modulation bandwidth. In this chapter, we show that these limitations can be overcome by extending the slot-waveguide concept to the modulating radio-frequency (RF) signal. Our device combines an RF slotline that relies on $BaTiO_3$ as a high-k dielectric material with a conventional silicon photonic slot waveguide and a highly efficient organic EO cladding material. In a proof-of-concept experiment, we demonstrate a 1 mm-long Mach-Zehnder modulator that offers a 3 dB-bandwidth of 76 GHz and a 6 dB-bandwidth of 110 GHz along with a small π-voltage of 1.3 V ($U_\pi L$ = 1.3 V mm). We further demonstrate the viability of the device in a data transmission experiment using four-state pulse-amplitude modulation (PAM4) at line rates up to 200 Gbit/s. Our first-generation devices leave vast room for further improvement and may open an attractive route towards highly efficient silicon photonic modulators that combine sub-1 mm device lengths with sub-1 V drive voltages and modulation bandwidths of more than 100 GHz.

5.1 Introduction

High-speed electro-optic (EO) modulators are key devices for optical communications [93]–[95], optical metrology[96], microwave photonics [97], or ultra-broadband signal processing at THz bandwidths [55]. Ideal modulators should combine small π-voltages U_π, low insertion losses a, and short device lengths L with large modulation bandwidths, while offering a path to cost-efficient mass production and monolithic co-integration with advanced photonic circuitry. In practice, however, it is challenging to fulfill all these requirements simultaneously. When it comes to scalability and high-density integration, the silicon photonic (SiP) platform would be the technology of choice, exploiting highly mature CMOS processes and offering a rich portfolio of advanced photonic devices that can be realized with high yield on large-area wafers [98]. However, due to the absence of the Pockels effect in silicon, conventional SiP modulators rely on carrier injection or depletion in *p*-*n* junctions that are integrated into the optical waveguides [99]. This leads to an inherent trade-off between device efficiency and modulation bandwidth. As an example, depletion-type SiP modulators were demonstrated with bandwidths of 48 GHz, but the efficiency of these devices was rather low with $U_\pi L$ products of 7.4 V mm [13]. The efficiency of SiP modulators can be greatly improved by combining low-loss slot waveguides on silicon-on-insulator (SOI) with optimized organic electro-optic materials in a hybrid approach [36], [100]. These so-called silicon-organic hybrid (SOH) devices can benefit from ultra-high in-device electro-optic coefficients of, e.g., 390 pm/V, leading to ultra-low voltage-length products down to $U_\pi L$ = 0.32 V mm [28]. However, without a supporting gate voltage [27], the EO bandwidth of experimentally demonstrated slot-waveguide SOH modulators is limited [32] to, e.g., 25 GHz or less [31] due to the *RC* time constant associated with the capacitance of the slot and the resistance of the adjacent doped Si slabs [32]. Plasmonic-organic hybrid (POH) MZM [34], [36], [55], [91], [101] can overcome these limitations by replacing the silicon slabs with highly conductive gold pads and by exploiting surface plasmon polaritons in the resulting metallic slot waveguide. This, however, comes at the price of substantial optical losses a, leading to rather high loss-efficiency products [36] $aU_\pi L$ of more than 10 V dB [55], [88] as compared to 1 V dB for SOH devices [28], [29]. Other integration platforms such as thin-film lithium-niobate have

shown impressive modulation bandwidths of up to 100 GHz [17], but their efficiency is limited by rather high voltage-length-products $U_\pi L$ in excess of 20 V mm [17], and monolithic co-integration with other devices is difficult. Modulators based on indium-phosphide (InP) can also offer large bandwidths of, e.g., 80 GHz [102], but the voltage length-products of more than 6 V mm are still comparatively high, and fabrication relies on rather expensive processes that cannot compete with the scalability and maturity of the silicon photonic platform. Thus, a scalable approach to realize highly efficient and low-loss modulators with large electro-optic bandwidth is still lacking.

Here, we report on a novel concept for hybrid silicon photonic modulators that allows combining the high efficiency of organic electro-optic materials with large modulation bandwidths without the need for lossy plasmonic structures. The device overcomes the *RC* limitations of conventional SOH slot-waveguide modulators by replacing resistive coupling through the doped Si slabs with capacitive coupling via high-k dielectric material [103]. In a proof-of-concept experiment, we demonstrate a 1 mm-long capacitively-coupled SOH (CC-SOH) Mach-Zehnder modulator that exploits barium titanate ($BaTiO_3$) as high-k dielectric and simultaneously offers a large EO bandwidth of 76 GHz and a small π-voltage of 1.3 V ($U_\pi L$ = 1.3 V mm). To validate the viability of the device, we generate a 4-state pulse-amplitude modulation (PAM4) signals at symbol rates (line rates) up to 100 GBd (200 Gbit/s) with bit-error ratios (BER) below the threshold for soft-decision forward-error correction. As our first-generation devices are not yet optimized and leave vast room for further improvement, we believe that the CC-SOH concept opens an attractive route towards highly efficient silicon photonic modulators that combine sub-1 mm device lengths with sub-1 V drive voltages, sub-1 dB phase-shifter losses, and modulation bandwidths of 100 GHz or more.

5.2 SOH modulator: resistive coupling vs capacitive coupling

The concept of capacitively-coupled silicon-organic hybrid (CC-SOH) modulators and their advantages over resistively-coupled SOH (RC-SOH) devices are explained in Fig. 5.1. Figure 5.1(a) shows the cross section of a conventional

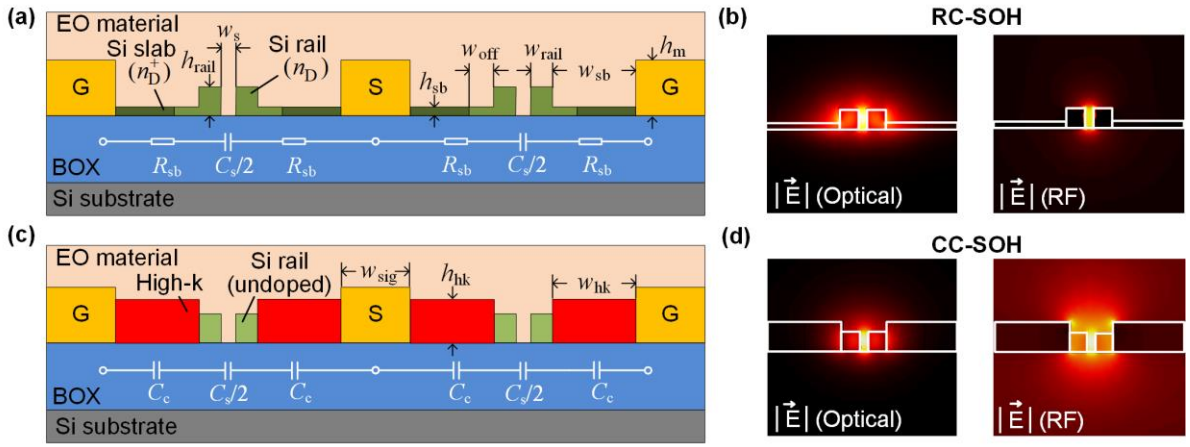

Figure 5.1: Resistively-coupled vs. capacitively-coupled silicon-organic hybrid (SOH) modulator. (a) Cross-section of a conventional resistively-coupled SOH (RC-SOH) Mach-Zehnder modulator (MZM) on the silicon-on-insulator (SOI) platform. The phase modulator in each arm of the MZM comprises a silicon slot waveguide formed by two silicon (Si) rails (green) with typical heights $h_{\mathrm{rail}} = 200\ldots400\,\mathrm{nm}$ and widths $w_{\mathrm{rail}} = 150\ldots200\,\mathrm{nm}$, which are separated by a gap of width $w_{\mathrm{s}} = 80\ldots200\,\mathrm{nm}$. The device is covered by an organic EO material (light orange), which also fills the slot. The Si rails are connected to the metal strips of the ground-signal-ground (GSG) transmission line (yellow) through doped Si slabs (green) such that, at low frequencies, the RF modulating voltage drops predominantly in the slot region. To reduce optical loss, a smaller doping concentration n_{D} is used in the rails and in the directly adjacent slab regions of width w_{off} (light green), whereas the slab regions further away from the optical slot waveguide (dark green) are subjected to a higher doping concentration n_{D}^{+} [32]. A simplified equivalent-circuit model of the RC-SOH MZM is depicted as a white overlay. In this model, the slot waveguide of each phase modulator is represented by a capacitance $C_{\mathrm{s}}/2$, which is connected to the ground and the signal strip of the transmission line through a total slab resistance $2R_{\mathrm{sb}}$. **(b)** Electric-field profiles of the optical quasi-TE mode and the RF mode of the RC-SOH phase modulator. Both figures indicate the magnitudes of the complex electric field vectors. The optical and the RF field show strong a field overlap within the slot, resulting in a high modulation efficiency. **(c)** Cross-section of capacitively-coupled SOH (CC-SOH) MZM, where the doped Si slabs in (a) are substituted by a high-k dielectric material (red), thus replacing the resistive coupling by a capacitive coupling. As depicted in the simplified equivalent circuit, the slot capacitance $C_{\mathrm{s}}/2$ of each MZM arm is now electrically connected to the metal traces of the transmission line through a coupling capacitance C_{c}. The coupling capacitance C_{c} is typically much larger than the slot capacitance $C_{\mathrm{c}} \gg C_{\mathrm{s}}$, such that RF voltage applied to the transmission line drops predominantly across the slot. In contrast to RC-SOH modulators, CC-SOH devices do not suffer from optical loss in the Si rails and from RC time constants associated with resistive coupling. Appendix B.5 provides a more detailed design study of CC-SOH devices and discusses the impact of the high-k slab width w_{hk}, height h_{hk}, and height h_{m} of the metal transmission-line traces **(d)** Electric-field profiles of the optical quasi-TE mode and the RF mode of the CC-SOH phase modulator. Since the relative permittivity of the high-k dielectric is much larger than the relative permittivity of the Si or the EO material, the horizontal component of the RF field in the slot region is locally enhanced. The structure thus combines a silicon photonic slot waveguide for optical frequencies and a high-k dielectric slotline for RF frequencies. The strong confinement of both the optical and RF fields to the EO material

in the slot region ensures strong interaction and leads to efficient modulation, see Appendix B.3A for a quantitative model. The field distributions in subfigures (b) and (d) were calculated using a commercial electromagnetic simulation tool (CST Microwave Studio), see Appendix B.1 details.

RC-SOH MZM [36], realized on a silicon-on-insulator (SOI) substrate. Each arm of the MZM comprises a silicon (Si) slot waveguide formed by two Si rails (green), which typically feature rail widths $w_{\mathrm{rail}} = 150\ldots200\,\mathrm{nm}$ and rail heights $h_{\mathrm{rail}} = 200\ldots400\,\mathrm{nm}$ which are separated by a slot of width $w_{\mathrm{s}} = 80\ldots200\,\mathrm{nm}$. The radio-frequency (RF) modulating signal is carried by a coplanar transmission line (yellow) in ground-signal-ground (GSG) configuration. The Si rails are connected to the metal trace of the transmission line via doped Si slabs (dark green) having typical heights $h_{\mathrm{sb}} = 50\ldots70\,\mathrm{nm}$ and widths $w_{\mathrm{sb}} = 1.2\ldots2.0\,\mu\mathrm{m}$. The slot region is filled with an organic EO material which, at near-infrared telecommunication wavelengths, has a refractive index of $(n_{\mathrm{EO}} \approx 1.6\ldots1.9)$, much smaller than that of Si $(n_{\mathrm{Si}} \approx 3.5)$. This leads to a pronounced field enhancement of the optical quasi-transverse-electric (quasi-TE) mode in the slot region, see Fig. 5.1(b) [46]. At the same time, when operated at sufficiently low modulation frequencies, the voltage applied to the transmission line entirely drops across the narrow slot region. This leads to a tight confinement of the electric RF field to the slot, see Fig. 5.1(b), and ensures strong overlap with the optical mode, which results in high modulation efficiency, see Appendix B.1 for details.

The concept of RC-SOH MZM opens a path towards compact devices with sub-1mm phase shifter lengths and sub-1V operation voltages [28], [29] that can be directly driven by highly scalable CMOS circuits without the need for a separate amplifier [30]. At high operation frequencies, however, the slot capacitance cannot be fully charged and discharged through the resistive slabs during one modulation cycle [32]. For a quantitative description of the RC-SOH MZM dynamics, we use a simple equivalent-circuit model, illustrated as a white overlay in Fig. 5.1(a). Each of the two slot waveguides is represented by a slot capacitance $C_{\mathrm{s}}/2$, which is connected to the metal transmission line through a total slab resistance $2R_{\mathrm{sb}}$. Taking into account the contribution of both arms, this results in an intrinsic *RC*-limited bandwidth $f_{\mathrm{RC}} = 1/(2\pi R_{\mathrm{sb}} C_{\mathrm{s}})$ for the RC-SOH MZM. High-bandwidth RC-SOH devices require low slab resistivity and hence

high doping concentration, which leads to larger optical losses. This trade-off between optical loss and *RC*-limited bandwidth can be avoided by using a tailored doping profile, where the Si rails and the directly adjacent slab regions have a lower doping concentrations n_D while much higher concentrations n_D^+ are used further away from the slot [32], see Fig. 5.1(a). Still, the *RC*-limited bandwidth turns out to be one of the most stringent restrictions of experimentally demonstrated RC-SOH devices [31], [44], [45]. In laboratory experiments, this limitation could only be overcome by applying a relatively high gate voltage U_gate across the buried SiO_2 (BOX) layer [27] to induce a charge accumulation layer in the Si slabs. However, this gate voltage typically exceeds 100 V [27], [31] and is thus not a solution for practical devices.

CC-SOH MZM overcome these limitations by avoiding the resistive slabs altogether and by using capacitive coupling instead. To this end, the doped Si slabs in Fig. 5.1(a) are replaced by a high-k dielectric material, which forms a large coupling capacitor between the optical slot waveguide and the metal traces of the GSG transmission line, see Fig. 5.1(c). The simplified equivalent circuit of this scheme is depicted as a white overlay in Fig. 5.1(c). Each phase modulator of the MZM is modeled by a slot capacitance $C_\mathrm{s}/2$, which is connected to the metal transmission line through a coupling capacitance C_c to each side of the slot. If the high-k dielectric has a relative permittivity ε_r much larger than that of Si and the EO material such that $C_\mathrm{c} \gg C_\mathrm{s}$, then the RF electric field drops predominantly across the slot region. The high-k dielectric is chosen such that the refractive index for optical wavelengths is smaller than n_Si such that confinement of the optical mode to the slot region is not impaired, and thickness of the high-k slabs may be chosen in the range $h_\mathrm{hk} = 150 \ldots 600\,\mathrm{nm}$, see Appendix B.5 which provides a more detailed design study of CC-SOH devices and discusses also the impact of the height h_m and the signal width w_sig of the metal transmission-line traces. Figure 5.1(d) shows the electric-field profiles of the optical quasi-TE mode and RF mode of the CC-SOH phase modulator assuming a refractive index $n_\mathrm{hk} = 1.85$ for the high-k dielectric, see Appendix B.1 for details on the calculation of the optical and RF mode fields. Since the relative permittivity of the high-k dielectric $(\varepsilon_\mathrm{r,hk} \approx 100)$ and of the Si $(\varepsilon_\mathrm{r,Si} \approx 11.7)$ is larger than that of the EO material $(\varepsilon_\mathrm{r,EO} \approx 5.68)$, the electric RF field in the slot region is locally enhanced. The structure thus combines a silicon photonic slot waveguide for optical frequencies with a high-k dielectric slotline for RF

frequencies [57]. This leads to a strong EO interaction of the RF and the optical fields, which can be quantified by a field interaction factor Γ_s that is obtained from an overlap integral of the optical and the RF fields in the slot region, see Appendix B.3A for details. For properly designed CC-SOH devices, these field interaction factors Γ_s can assume values that are on par with those of conventional RC-SOH devices, see Appendix B.5 for more details on advanced CC-SOH device designs. By proper choice of high-k materials with low absorption in the near infrared [57], CC-SOH devices should hence permit simultaneous realization of low-loss and high modulation efficiency. Examples of high-k dielectric materials with $\varepsilon_r > 100$ and refractive indices n_{hk} smaller than n_{Si} are TiO_2, $SrTiO_3$, $BaSrTiO_3$ and $BaTiO_3$. Since the capacitive coupling between the transmission-line electrodes and the slot of an ideal CC-SOH MZM is not associated with a *RC* time constant, the bandwidth is only limited by the frequency-dependent propagation loss of the modulating RF signal, by impedance mismatch, and by the velocity mismatch between the RF and the optical wave. By an optimized travelling-wave design, CC-SOH devices thus offer a route towards low-loss, highly-efficient modulators featuring large electrical bandwidths.

5.3 Bandwidth measurement of CC-SOH MZM

To demonstrate the viability of the CC-SOH concept, we fabricated a 1 mm-long CC-SOH MZM with amorphous $BaTiO_3$ (BTO) as high-k dielectric. The device is realized on an SOI substrate having a 220 nm-thick Si device layer and a 2 µm-thick buried oxide (SiO_2), see Appendix B.2.1 for details. A schematic layout of the MZM is depicted in Fig. 5.2(a). Light is coupled to the SiP chip via an on-chip grating coupler (GC). A multimode interference (MMI) coupler splits the incoming light and launches it into the two arms of an unbalanced MZM. The two arms have a path difference of 80 µm that allows for an adjustment of the operating point by tuning the wavelength. The modulating RF signal is coupled to the MZM through a coplanar transmission line, which is realized in ground-signal-ground (GSG) configuration. A second MMI at the other end of the MZM combines the modulated light and feeds it to an output waveguide, which is connected to another GC. Figure 5.2(b) shows a false-colored scanning electron microscope (SEM) image of a section of the CC-SOH MZM as defined

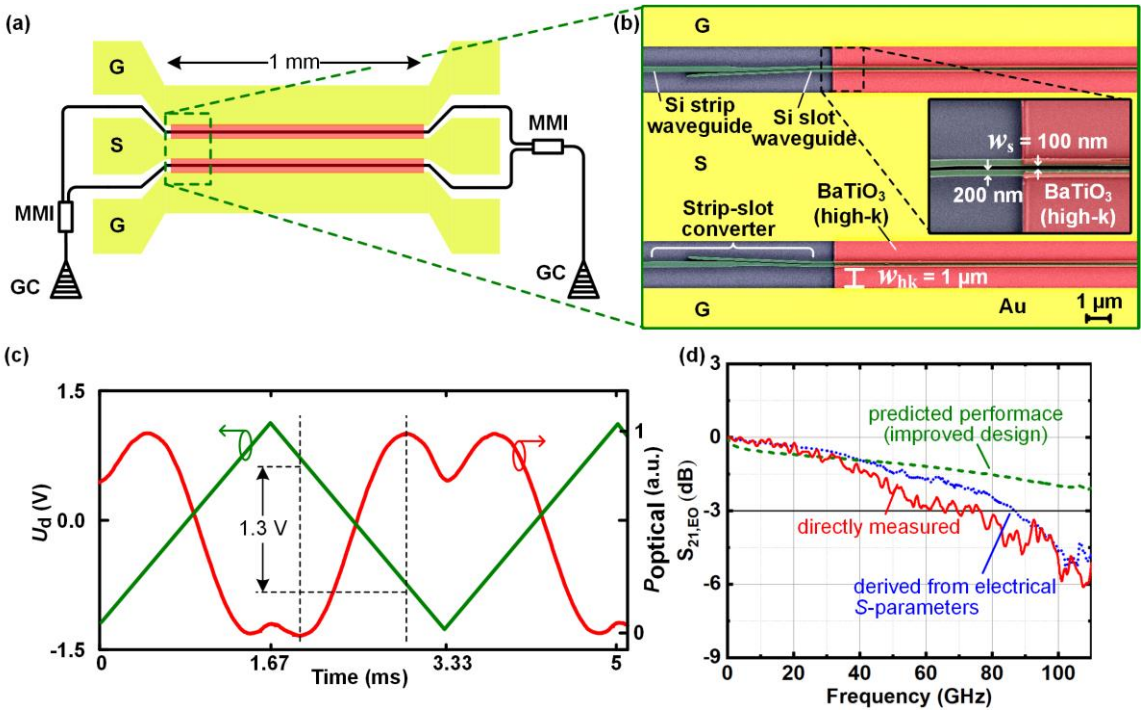

Figure 5.2: Capacitively-coupled SOH MZM using barium titanate ($BaTiO_3$, BTO) as a high-k dielectric. (a) Schematic of a CC-SOH MZM driven by a coplanar ground-signal-ground (GSG) transmission line. Light is coupled in and out of the device via on-chip grating couplers (GC). Multimode interference (MMI) couplers are used to split and recombine the light of the two MZM arms. **(b)** False-colored SEM image of a CC-SOH MZM section, as defined by the dashed green rectangle in (a). Each phase-shifter arm of the MZM comprises a strip-to-slot converter (green) for coupling light from the Si strip waveguide to the Si slot waveguide. A coplanar ground-signal-ground (GSG) transmission line made from gold (yellow) carries the RF signal. Amorphous BTO slabs (red) having a height of 150 nm and a width of $w_{hk} = 1\,\mu m$ are deposited between the Si slot waveguide and the gold strips of the coplanar transmission line. The phase shifter section of each arm is 1 mm long. The inset shows a zoom-in of one of the MZM arms comprising a Si slot waveguide with a slot width $w_s = 100$ nm and between 200 nm-wide Si rails. **(c)** Measurement of the π-voltage of a BTO-based CC-SOH MZM showing the intensity-modulation at the device output (red) for a 0.3 kHz triangular drive signal (green). The π-voltage $U_\pi = 1.3\,V$ can be directly read from the voltage increment needed to drive the intensity modulation from minimum to maximum transmission. **(d)** Dynamic behavior of a 1-mm-long CC-SOH MZM with YLD124 as EO cladding material: The red curve shows the electro-optic (EO) response $S_{21,EO}$ measured using a vector network analyzer (VNA) and a calibrated high-speed photodiode. The measured 3 dB EO bandwidth of the 1 mm-long CC-SOH MZM is 76 GHz. As a reference, we also derive the EO response from the measured electrical *S*-parameters of the device using an analytical model [123], see Appendix B.3C for details. The analytically derived result is indicated by the blue curve and agrees well with the directly measured behavior. The strong frequency-dependent decay of the EO response is mainly caused by the strong RF propagation loss of the modulating signal along the coplanar transmission line having a thickness of only 150 nm. By using thicker gold strips, the bandwidth of the MZM can be significantly increased. This is indicated by the green curve,

which corresponds to the predicted EO response of an improved device design that relies on 600 nm-thick gold strips for the coplanar transmission line, see Appendix B.5 for details. Such a device could offer 3 dB EO bandwidths well beyond 100 GHz.

by the dashed (green) rectangle in the Fig. 5.2(a). Each MZM arm consists of a Si strip waveguide (width $w = 500\,\text{nm}$; height $h = 220\,\text{nm}$), which is transformed into a slot waveguide using a strip-to-slot converter[47]. The slot waveguide comprises two Si rails (green) with widths w_{rail} = 200 nm, which are separated by a slot of width $w_{\text{s}} = 100\,\text{nm}$, see inset in Fig. 5.2(b). A coplanar transmission line made from 150 nm-thick gold electrodes (yellow) in ground-signal-ground (GSG) configuration carries the RF signal. Amorphous BTO slabs (red) having a height $h_{\text{hk}} = 150\,\text{nm}$ and a width $w_{\text{hk}} = 1\,\mu\text{m}$ are deposited between the Si slot waveguide and the metal electrodes using room-temperature RF magnetron sputtering followed by a lift-off process, see Appendix B.2.1 for details.

Note that, for high-performance devices, both the slab width w_{hk} and the height h_{hk} are generally subject to design trade-offs: Reducing the slab width w_{hk} increases the coupling capacitance C_{c} and thus increases the modulation efficiency, but also results in larger interaction of the optical mode with the metal traces of the RF transmission line and therefore results in larger optical losses. For the chosen slab width of $w_{\text{hk}} \geq 1\,\mu\text{m}$, the contribution to the optical loss is of the order of 0.1 dB/mm or less and hence does not play a significant role, see Fig. B.8 and the associated discussion in Appendix B.5 for details. Regarding the slab height, we chose a value of $h_{\text{hk}} = 150\,\text{nm}$ due to limitations of an existing lift-off process that relied on a thin PMMA resist layer and that was used for fabricating our devices. A thorough analysis of the associated design trade-offs reveals that this value is too small and should be increased in future device generations: If the slab is too thin, the coupling capacitance will be small and the RF field does not have an good overlap with the optical mode, resulting in a reduced field interaction factor Γ_{s}. On the other hand, if the BTO slab is too thick, the transverse capacitance of the line will increase and lead to a reduced line impedance below the envisaged 50 Ω, while the field interaction factor saturates and does not increase further, see Appendix B.5 for a detailed analysis. Given the fact that a certain operation voltage of the MZM is dictated by the required phase shift, a lower impedance will increase the power consumption

of the device, which is undesired. A more detailed design study for improved CC-SOH devices shows that BTO films with a height of approximately $h_{\mathrm{hk}} \approx 350\,\mathrm{nm}$ would to a decent trade-off between these competing targets, see Appendix B.5. Similarly, a height of $h_{\mathrm{m}} = 150\,\mathrm{nm}$ was chosen for the metal GSG traces to stay within the limitations of our lift-off-process, which leads to significant RF propagation loss and turned out to be the main limitation of the measured bandwidth. Future device designs should use thicker traces with $h_{\mathrm{m}} \geq 500\,\mathrm{nm}$ that significantly reduce the RF propagation loss, see Appendix B.5. Such improved CC-SOH devices with thicker BTO and metal layers can still be fabricated using lift-off process based on multi-layer resists [104], [105].

In the course of our experiments, we also characterized the optical properties of the deposited amorphous BTO thin films, having a refractive index of $n_{\mathrm{BTO}} = 1.85$ at a wavelength of 1550 nm, see Appendix B.2.3 for details. After fabrication of the device, an organic EO material (YLD124, $n_{\mathrm{EO}} = 1.9$ [54]) is filled into the silicon slots. Note that the refractive indices of the BTO and the EO material are very similar, ensuring a smooth transition of the optical mode without significant reflections. To orient the organic chromophores, the EO material is activated by a one-time poling process [36]. To this end, the chip is heated above the glass transition temperature of the organic EO material, and a DC voltage is applied across the floating ground electrodes to align the dipolar chromophores in the two slots. The orientation of the chromophores is frozen by cooling the chip to room temperature while maintaining the DC poling field. This leads to a configuration where the driving electric RF field applied to the GSG transmission line is parallel to the poling direction in one MZM arm and antiparallel in the other arm, thereby enabling operation of the CC-SOH MZM in push-pull mode [36].

To quantify the modulation efficiency, we measure the π-voltage U_{π} of the MZM by driving it with a 0.3 kHz triangular signal U_{d} as depicted in Fig. 5.2(c), green curve. The intensity-modulated output (red curve) of the MZM is detected by a photodiode and recorded along with the drive signal using an oscilloscope. We measure a voltage difference of $U_{\pi} = 1.3\,\mathrm{V}$ that is needed to drive the transmission of the MZM from its minimum to its maximum by introducing a phase shift of π between the optical signals in the 1 mm-long MZM arms, thus leading to a π-voltage-length product of $U_{\pi}L = 1.3\,\mathrm{V\,mm}$. To

estimate the associated EO coefficient r_{33} of the organic EO material, we calculate the field interaction factor Γ_s for the fabricated CC-SOH structure, see Appendix B.3B. To this end, we first extract the relative permittivity $\varepsilon_{r,BTO} = 18$ and the loss tangent $\tan\delta_{BTO} \approx 0.03$ of the amorphous BTO films from dedicated test structures, see Appendix B.2.4 and B.2.5. Based on this, we calculate the distribution of the RF field using a commercial numerical solver (CST Microwave Studio), and we estimate a field interaction factor of $\Gamma_s = 0.048$ between the RF and the optical fields through electromagnetic simulations. Using Eq. (S11) in Appendix B.3A, we calculate an electro-optic coefficient of $r_{33} \approx 180$ pm/V, which was obtained with a poling field of approximately 450 V/µm in the slot region, see Appendix B.3B for details. The achieved EO coefficient is in fair agreement with previously reported values for the same or for similar materials. Specifically, an EO coefficient of $r_{33} \approx 242(\pm 37)$ pm/V was obtained for pure YLD124 when poling the material through adjacent dielectric layers in a thin-film experiment[106]. Similarly, for conventional RC-SOH MZM with 150 nm-wide slots, in-device EO coefficients r_{33} of approximately 250 pm/V [28] were obtained using poling fields of approximately 400 V/µm in combination with the organic EO material JRD1, that has a chromophore structure similar to that of YLD124 [28]. Note that the slot width $w_s = 100$ nm in our device is smaller, which is known to reduce the poling efficiency [28].

We also measure the optical losses of our current devices. For a 1 mm-long CC-SOH MZM, we obtain a fiber-to-fiber insertion loss of 19 dB, out of which an overall 10 dB are caused by the two on-chip grating couplers while 3 dB originate from other passive on-chip structures such as transport waveguides, strip-to-slot converters, and MMI couplers. The propagation loss in the CC-SOH phase shifter amounts to 6 dB/mm, which we attribute to scattering losses due to surface roughness that results from an imperfect waveguide fabrication process, see Appendix B.2.2 for details. Note that these losses can be greatly reduced by optimized designs and fabrication processes [107]. Specifically, systematic optimization of strip-to-slot converters and MMI couplers may allow to reduce the losses of these building blocks to 0.02 dB and 0.2 dB, respectively [47],[108], leading to an overall loss contribution of less than 0.5 dB. We further expect that propagation losses in the CC-SOH phase shifter section can be reduced to less than 0.2 dB/mm by using highly optimized waveguide fabrication

procedures based on 193 nm deep-UV lithography and dry-etching processes [107]. Note that amorphous and polycrystalline BTO has relatively low absorption losses in the visible and near infrared [109]–[113], such that the BTO slabs directly adjacent to the Si rails should not contribute substantially to the overall propagation loss. Accounting for an additional contribution of 0.1 dB/mm from the interaction of the guided light with the gold traces of the GSG transmission line, we expect that the propagation loss in the CC-SOH phase shifter may eventually be reduced to less than 0.3 dB/mm. Assuming a 1 mm-long CC-SOH phase shifter and taking into account an additional 0.5 dB of loss from the strip-to-slot converters and MMI couplers [47][108], on-chip insertion losses of the order of 1 dB might eventually come into reach, which can very well compete with low-loss RC-SOH devices of much lower bandwidth [29]. Fiber-chip and chip-chip coupling losses can be greatly reduced by using 3D-printed micro-lenses [114] or photonic wire bonds [115], [116].

To measure the frequency response of the CC-SOH MZM, the wavelength is adjusted for operation in the quadrature point. An RF drive signal with frequency in the range between 0.01 GHz and 110 GHz is supplied by a vector network analyzer (VNA, Keysight PNA-X N5247) and is coupled to the GSG transmission line of the MZM using a microwave probe. The other end of the transmission line is connected to another microwave probe, which is terminated by a 50 Ω impedance. The intensity-modulated output of the CC-SOH MZM is received by a calibrated high-speed photodiode (HHI, C05-W36) having a 3 dB bandwidth of 78 GHz, which is connected to second port of the VNA. The measured data is corrected by accounting for the frequency response of the photodiode, the probes, and the RF cables, leading to the electro-optic (EO) response $S_{21,\mathrm{EO}}$ of the CC-SOH MZM, see red curve in Fig. 5.2(d). For a 1-mm-long BTO-based CC-SOH MZM, we measure a 3 dB EO bandwidth of approximately 76 GHz. Note that the 3 dB EO bandwidth corresponds to a frequency at which the phase-modulation index is reduced by a factor of $1/\sqrt{2}$, corresponding to a 3 dB decay in the associated RF power generated by the photodiode. Alternatively, the bandwidth can be specified in terms of the 6 dB bandwidth, which corresponds to a power decay of the associated photocurrent by a factor of four and amounts to approximately 110 GHz for the current device. In the literature [32], [117]–[121] of EO modulators, both conventions of bandwidth are used, often without an explicit mention of the adopted specification.

Note that the bandwidth measured for the current MZM is not limited by the device concept but is a consequence of the non-optimum electrical design of our first-generation structures. Specifically, as described above, the metal transmission line is fabricated using a lift-off process with a thin photoresist, which limited the thickness of the gold layer to a rather small value of approximately 150 nm. This leads to significant RF propagation loss, which increases strongly with frequency. To better understand the underlying bandwidth limitations, we perform a detailed evaluation [122] of the device dynamics. In first step, we measure the electrical *S*-parameters of the CC-SOH modulator, in particular the frequency-dependent complex amplitude reflection factor $\underline{S}_{11}$ at the input and the complex amplitude transmission factor $\underline{S}_{21}$. From the measured *S*-parameters, we then derive the line impedance, the RF propagation loss, and the RF propagation constant, which is associated with the RF effective refractive index $n_{\mathrm{e,RF}}$. Adopting the analytical model described in [123], we predict the EO response of the CC-SOH device which would be expected based on the electrical behavior, see Appendix B.3C for details. This analysis includes the contribution due to the losses of the underlying RF transmission line, impedance mismatch, as well as the walk-off between the RF modulation signal and the optical signal. The results of this analysis, indicated as a blue trace in Fig. 5.2(d), agree well with the directly measured EO response of the device, red trace, and we conclude that the decay of the EO response mainly originates from the electrical behavior of the RF line. We also find that walk-off between the RF signal and the optical signal does not represent a significant limitation of the current devices – based on an optical group refractive index $n_{\mathrm{g,opt}} = 2.8$ at 1550 nm and an RF effective index $n_{\mathrm{e,RF}} = 2.2$, we estimate a walk-off-related 3 dB bandwidth of approximately 220 GHz [124], see Appendix B.3C for details. As a consequence, high RF propagation loss remains as the most important reason for the strong decay in the frequency response of our first-generation CC-SOH devices.

The RF propagation loss has two main contributions – conductor loss and dielectric loss. To investigate the contribution from the dielectric loss of BTO, we analyze the RF properties of our BTO thin films, see Appendix B.2.4 and B.2.5 for details. We determine a frequency-independent relative permittivity $\varepsilon_{\mathrm{r,BTO}} = 18$ and a loss tangent $\tan\delta_{\mathrm{BTO}} = 0.02$, which are in good agreement with previously reported measurements of amorphous BTO films [125]–[128].

At a frequency of 50 GHz, this loss tangent would lead to a dielectric loss less than 0.4 dB/mm in bulk BTO, which is much smaller than the overall RF propagation loss of 4.5 dB/mm measured for the fabricated CC-SOH MZM, see Fig. B.7 in Appendix B.3C . We hence conclude that the ohmic loss of our transmission-line traces dominates the attenuation of the modulating signal, which is confirmed by an electrical simulation (CST Microwave Studio) of a transmission line built from 150 nm-thick gold transmission traces with a conductivity of $2.6\times10^7\,\mathrm{S/m}$, see Appendix B.3C for details. The conductor loss can be significantly reduced by using thicker gold layers for the transmission line electrodes. For such an improved design of a CC-SOH modulator having a 600 nm-thick metal electrodes, the 3 dB bandwidth of the 1 mm-long CC-SOH MZM can be significantly higher than 100 GHz, see green curve in Fig. 5.2(d). Details on the advanced device designs can be found in Appendix B.5 .

Besides increased modulation bandwidth, our first-generation CC-SOH modulators also leave room for improving the modulation efficiency. The $U_\pi L$ product of the devices may be greatly reduced by using polycrystalline BTO layers with relative permittivity $\varepsilon_{\mathrm{r,BTO}} \geq 100$ [126], [128], which is much larger than the value of $\varepsilon_{\mathrm{r,BTO}} = 18$ measured for our current devices. This results in a much better confinement of the modulating RF field to the slot, which, in combination with increased heights of the BTO slabs of $h_{\mathrm{hk}} \geq 400\,\mathrm{nm}$, will to a more than three-fold increase of the field interaction factor from the current value of $\Gamma_s = 0.048$ to values of $\Gamma_s = 0.17$, see Fig. B.10(a) in Appendix B.5 for details. Moreover, the Si rails might be slightly doped to further improve the confinement of the RF field mode to EO material in the slot, allowing for field interaction factors $\Gamma_s > 0.3$, which are comparable to those obtained by conventional RC-SOH devices. A more detailed analysis of these approaches to improve the field interaction factor can be found in Appendix B.5 . In addition to this, we may use more efficient EO materials such as JRD1 [106], for which in-device EO coefficients of 390 pm/V have been demonstrated in conventional RC-SOH devices with 160 nm-wide slots [28]. Combining all these improvements, we would hence expect that the current $U_\pi L$ product of approximately 1.3 Vmm could be reduced by at least factor of three, such that values of less than 0.5 Vmm can be expected. This brings sub-1V drive voltages for sub-1 mm device lengths into reach.

5.4 High-speed signaling experiments

Figure 5.3(a) shows the setup for evaluating the performance of a CC-SOH MZM in high-speed data transmission. The electrical drive signals are synthesized by a 120 GSa/s arbitrary-waveform generator (AWG, Keysight M8194A) with an analog bandwidth of 45 GHz. We use a pseudo-random bit sequence (length $2^{11}-1$) along with pulse shapes featuring a raised-cosine power spectrum to generate two- and four-level electrical signals at symbol rates of 64 GBd and 100 GBd. The drive signals are fed to an RF amplifier (Centellax, UA1L65VM) followed by a 6 dB attenuator before being coupled to the GSG pads of the CC-SOH MZM via a microwave probe (Cascade Microtech, i67A, 67 GHz bandwidth) and a bias-tee. The other end of the GSG transmission line is terminated with a 50 Ω impedance via a second microwave probe. In addition to the wavelength adjustment of the operating point in the unbalanced CC-SOH MZM, a DC voltage U_{bias} is applied via the bias tee for fine-tuning. For generating high-speed optical signals, an optical carrier at a wavelength near 1550 nm with input optical powers between 8 dBm and 10 dBm is provided by an external cavity laser (ECL) and adjusted in polarization using a fiber-based polarization controller (PC). Light is coupled in and out of the CC-SOH MZM via on-chip grating couplers (GC). The intensity-modulated output of the MZM is amplified by an erbium-doped fiber amplifier (EDFA), and the out-of-band amplified spontaneous emission (ASE) noise is suppressed by an optical band-pass filter (Opt. BPF) with a 2 nm passband. The signal is finally fed to a high-speed photodiode having a bandwidth of 70 GHz (Finisar XPDV3120R). The resulting electrical signal is first boosted using an RF amplifier and then recorded by a 100 GHz real-time oscilloscope. For generating the electrical drive signals, we use digital pre-emphasis to compensate for the frequency roll-off of the AWG, of the subsequent RF amplifier, the 6dB attenuator, and of the bias-tee, see Appendix B.4 for details. Note that the pre-emphasis does not correct for the frequency roll-off of the CC-SOH MZM itself. The CC-SOH MZM is biased at the quadrature point such that the modulation loss amounts to approximately 3 dB. The modulated signal is amplified to an average power of about 8 dBm at

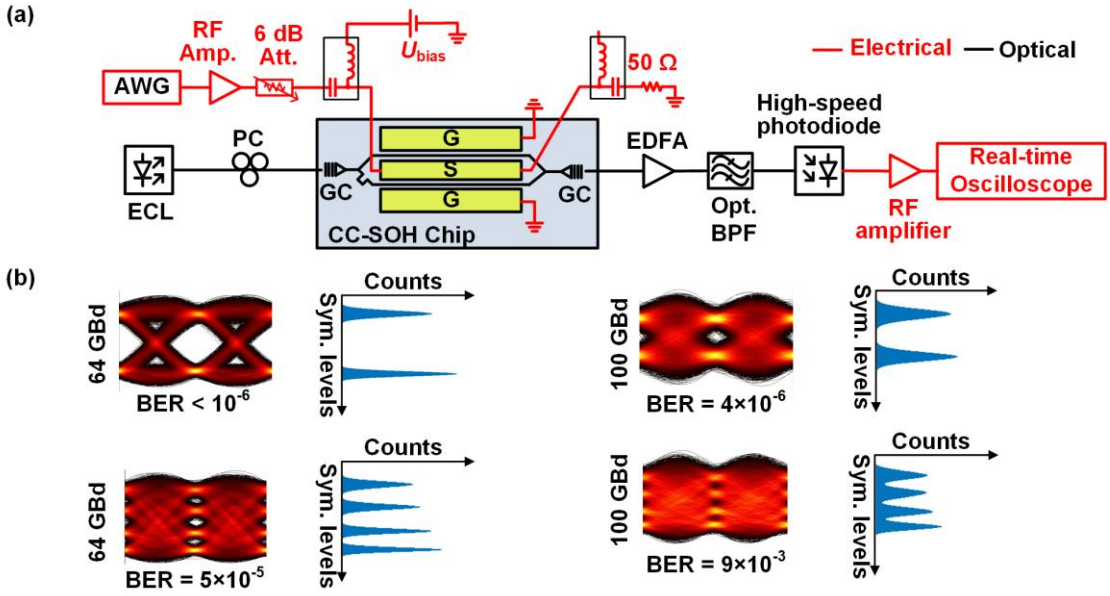

Figure 5.3. High-speed signaling with a CC-SOH MZM using BTO as a high-k dielectric. **(a)** Setup for data signal generation and detection. An arbitrary-waveform generator (AWG) followed by an RF amplifier and a 6dB attenuator are used to drive the modulator. The electrical drive signal is fed to the ground-signal-ground (GSG) coplanar transmission line via a microwave probe (not shown). The operating point of the MZM with un-balanced arm lengths is set by the optical wavelength and fine-tuned by a DC voltage U_{bias} applied through a bias tee. Light from an external-cavity laser (ECL) is coupled to the CC-SOH MZM via a polarization controller (PC) and an on-chip grating coupler (GC). An erbium-doped fiber amplifier (EDFA) is used to amplify the light from the output GC, and a band-pass filter (Opt. BPF) suppresses the amplified spontaneous emission (ASE) noise, before a high-speed photodiode receives the light. The RF signal from the photodiode is amplified and captured by a real-time oscilloscope (RTO) **(b)** Eye diagrams for symbol rates of 64 GBd and 100 GBd along with the histograms of the amplitudes in the sampling point and with measured bit error ratios (BER). At 64 GBd, the BER is below 10^{-6} for on-off keying (OOK) and reaches 5×10^{-5} for four-state pulse amplitude modulation (PAM4). At 100 GBd OOK, a BER of 4×10^{-6} is measured, well below the forward error correction (FEC) limit for 7 % overhead. For 100 GBd PAM4 (line rate 200 Gbit/s), we measure a BER of 9×10^{-3}, which is still below the threshold for soft-decision FEC (SD-FEC) limit with 20 % overhead.

the input of the receiver photodiode. In the transmission experiments, the modulator is driven by a signal with a maximum peak-to-peak voltage swing of approximately 1 V_{pp}, calculated from the RF power at the output of the bias-tee and from the losses of approximately 1.2 dB of the RF probe at 50 GHz.

Figure 5.3(b) shows the eye diagrams and the histograms of the detected amplitudes at the sampling point for symbol rates of 64 GBd and 100 GBd. For

64 GBd on-off keying (OOK), no bit errors could be measured in our 15 µs-long recordings, which contain approximately 10^6 symbols. We hence estimate a bit error ratio (BER) below 10^{-6}. At 100 GBd OOK (100 Gbit/s line rate), a BER of 4×10^{-6} is measured, which is well below the hard-decision forward error correction [89] (HD-FEC) limit with 7 % overhead. For 64 GBd four-state pulse amplitude modulation (PAM4), we measure a BER of 5×10^{-5}, which is also below the FEC hard-decision FEC threshold with 7 % overhead. For 100 GBd PAM4 signaling with a line rate of 200 Gbit/s, we obtain a BER of 9×10^{-3}, which is below the threshold for soft-decision FEC (SD-FEC) limit with 20 % overhead. We find that the rather high BER for 100 GBd PAM4 signaling is mainly caused by the low quality of the electrical drive signal, for which a BER of 1.7×10^{-3} was measured in an electrical back-to-back experiment, in which the output of the RF amplifier was attenuated and then fed directly to the real-time oscilloscope. Still, the demonstrated performance of our first-generation CC-SOH MZM is already on par with that of advanced RC-SOH devices[29], in which the RC time constant has been reduced by applying a gate voltage of approximately 200 V across the 2 µm-thick buried-oxide layer to induce a highly conductive electron accumulation layer that increases the slab conductivity [27].

5.5 Summary

We demonstrated a novel concept for SOH electro-optic modulators that relies on a capacitive coupling scheme to overcome the intrinsic bandwidth limitation of conventional devices with resistively-coupled slot waveguides. In a proof-of-concept experiment using amorphous $BaTiO_3$ as a high-k dielectric for enhanced capacitive coupling, we demonstrated a CC-SOH MZM having a 3 dB EO bandwidth of 76 GHz. The device features a small π-voltage-length-product $U_\pi L = 1.3\,\mathrm{Vmm}$. The viability of the CC-SOH modulator is demonstrated in a high-speed data transmission experiment, in which we generate PAM4 signals at line rates up to 200 Gbit/s. These results are obtained with first-generation devices that leave vast room for further improvements with respect to modulation efficiency, bandwidth, and optical loss. We believe that the CC-SOH con-

cept offers an attractive route towards highly efficient silicon photonic modulators that combine sub-1 mm device lengths with sub-1 V drive voltages, sub-1 dB insertion losses, and modulation bandwidths of 100 GHz or more.

[End of paper [J1]]

6 Summary and Outlook

6.1 Summary

High-speed electro-optic (EO) modulators are key devices for future data-hungry optical communication modules, optical metrology solutions and microwave photonic circuits. Leveraging mature CMOS fabrication technology, silicon-organic hybrid (SOH) modulators can overcome the lack of efficient modulators in the silicon photonic platform. SOH modulators [42] combine silicon photonic slot waveguides with organic EO cladding materials and have been demonstrated with ultra-low drive voltages [26] and record-high data rates up to 400 Gbit/s [44]. However, the underlying bandwidth of these devices is limited due to the intrinsic *RC* time constant. This thesis investigated new concepts to circumvent the bandwidth limitations of conventional SOH modulators. The key accomplishments of this work are summarized as follows:

First demonstration of THz-to-optical (T/O) conversion using an ultra-broadband plasmonic-organic hybrid (POH) modulator: The concept of organic hybrid modulators is extended to plasmonic slot waveguides which have no intrinsic *RC* limitation due to the high conductivity of the metallic structures. Using such plasmonic-organic hybrid (POH) modulators, ultra-compact devices with a footprint of 600 μm^2 and ultra-wide modulation bandwidths larger than 0.36 THz were demonstrated. Furthermore, using such an ultra-broadband POH modulator, we demonstrated seamless integration of a THz communication link into a fiber-optic network by directly modulating the THz data signals onto an optical carrier at the wireless receiver. In a proof-of-principle demonstration, we transmitted data signals up to 50 Gbit/s on a 0.288 THz carrier over a distance of 16 m and converted the data signals directly into optical domain using the POH modulator.

Demonstration of horizontal-slot POH modulator: In order to reduce the fabrication complexity of conventional vertical-slot POH modulators, we proposed and demonstrated POH Mach-Zehnder modulators with horizontal plasmonic slot waveguides. Using electromagnetic simulations and experiments, we

demonstrated that the π-voltage-loss product of POH modulators can be improved by at least 25 % by adopting horizontal plasmonic slot waveguides as opposed to the vertical plasmonic slot structures.

First demonstration of a novel concept of capacitively-coupled SOH (CC-SOH) modulator with the largest 3dB bandwidth in the silicon photonic platform: Though POH modulators offer compact footprints and unprecedented bandwidths, they exhibit a rather large insertion loss owing to the plasmonic nature of the device. In an alternative approach, we proposed a concept of CC-SOH modulator that relies on a high-k radio frequency (RF) slotline and that can overcome the bandwidth limitations of conventional resistively-coupled SOH devices, while still maintaining small insertion losses. In a proof-of-concept experiment, we show that a CC-SOH modulator using $BaTiO_3$ as the high-k material features a 3dB EO bandwidth of 76 GHz, the largest so far achieved with silicon photonic modulators based on dielectric waveguides. Furthermore, we prove the capability of CC-SOH modulators by generating PAM4 signals at record-high data rates of up to 200 Gbit/s.

6.2 Outlook and future work

The high-speed EO modulators investigated in this thesis rely on organic cladding materials. Though these organic materials offer record-high EO coefficients, their long-term stability, in particular their ability to withstand prolonged operation at high temperatures, needs further investigation. According to Telecordia standards [129], optoelectronic devices for telecommunication applications have to reliably operate for 2000 h at a temperature of 85°C. The organic EO materials used in this work do not yet allow for such operation conditions. However, side-chain EO materials with bulky adamantly units with high glass transition temperatures promise the required long-term stability [130] while offering high EO coefficients and thermal stability up to 250°C [131].

The POH modulators presented in this thesis offer great potential for high-speed optical transmitters for next-generation communication networks as well as for receivers for future THz communication networks. The core of the POH modulator technology are plasmonic slot waveguides that are filled with efficient EO materials. Since the metallic slots can be fabricated on different material

platforms, the POH modulator technology is platform-independent, provided that the light can be coupled in and out of the device. To this end, high-speed plasmonic modulators were demonstrated with a total device length of less than 40 µm fabricated in a single metal layer [35]. More recently, a monolithically integrated electro-optical transmitter is reported [132] by co-integrating a plasmonic modulator with high-speed bipolar CMOS electronic elements, offering symbol rates beyond 100 GBd. Apart from applications in communications, ultra-broadband POH modulators can serve as frontends for photonic-based analog-to-digital converters (ADCs) to convert a broadband electrical signal to the optical domain. However, this unprecedented bandwidth of POH modulators comes at a price – high insertion loss. For a slot width of 120 nm, typical propagation losses range in the order of 0.5 dB/µm which results in a rather high insertion loss of about 10 dB even for a phase shifter length of only 20 µm. The propagation loss may be reduced to about 0.2 dB/µm by using optimized metal deposition techniques [133] and by resorting to alternative materials which feature smaller plasmonic losses, for example silver. Nevertheless, for applications that require large bandwidths extending into the THz spectrum, the ultra-broadband nature of POH modulators outweighs their high insertion loss.

The CC-SOH modulator overcomes the intrinsic bandwidth limitation of conventional SOH modulators without use of plasmonic structures and therefore maintains small insertion losses. The CC-SOH modulators presented in this thesis are first-generation proof-of-concept devices and therefore leave vast room for further improvement of the device metrics. The EO bandwidth of 76 GHz of the first-generation devices can be extended beyond 100 GHz by reducing the on-chip RF propagation losses. Additionally, the bandwidth of the modulator can be improved by increasing the capacitance of the high-k layer. By fine-tuning the fabrication process to achieve smooth sidewalls and by using an optimized design of the other passive structures, the current phase shifter loss of 6 dB/mm can be brought down to less than 1 dB/mm. Furthermore, the low in-device EO coefficients of the current generation devices can be improved by at least a factor of 6 by poling the EO material with larger electric fields. This directly translates to a factor-of-six reduction in the π-voltage-length product of the modulator. We therefore believe that the CC-SOH concept opens an attractive route towards highly efficient silicon photonic modulators that combine sub-1 mm device lengths with sub-1 V drive voltages, sub-1 dB phase-shifter

losses, and modulation bandwidths beyond 100 GHz. Consequently, the next steps would be the device packaging and commercialization of the CC-SOH modulators.

Appendices

A. Characterization of ultra-broadband plasmonic modulator

The contents of this appendix is adapted from Methods and Supplementary Information of a publication [J3] in Nature Photonics. The structure and layout is modified to fit this document.

> **S. Ummethala**, T. Harter, K. Koehnle, Z. Li, S. Muehlbrandt, Y. Kutuvantavida, J. Kemal, P. Marin-Palomo, J. Schaefer, A. Tessmann, S. K .Garlapati, A. Bacher, L. Hahn, M. Walther, T. Zwick, S. Randel, W. Freude, C. Koos, "THz-to-optical conversion in wireless communications using an ultra-broadband plasmonic modulator" *Nature Photonics* 13(8), 519-524, (2019).
> DOI: 10.1038/s41566-019-0475-6

[Start of the Methods and Supplementary Information of paper [J3]]

A.1 Methods

Fabrication and characterization of plasmonic-organic hybrid modulators
The plasmonic-organic hybrid (POH) modulators used in our experiments are fabricated on standard silicon-on-insulator (SOI) substrates, featuring a 220 nm-thick silicon (Si) device layer and a 2 µm-thick buried oxide (SiO_2). Structures are defined by high-resolution electron-beam lithography. A partial Si dry etch step followed by a subsequent full etch of the Si layer is used to form the grating couplers and the 500 nm-wide Si nanowire waveguides. The metallic slots of the plasmonic Mach-Zehnder modulator (MZM) are fabricated via a lift-off process where a 150 nm-thick gold layer is thermally evaporated on a sacrificial layer of poly-methyl methacrylate (PMMA). The metallic slots in the two arms of the MZM are designed to be identical, each featuring a width of w = 75 nm, see Fig. 3.1(e). The Si nanowire waveguide, depicted in blue in Fig. 3.1(e), ends at the plasmonic section of the MZM with a taper tip angle of 12°, see inset of Fig. 3.1(e). These tapers enable efficient conversion between the photonic mode in the silicon waveguide and the surface plasmon polariton

(SPP) in the metallic slot with typical conversion losses of only 0.7 dB per transition [33]. The silicon waveguides in the two arms of the MZM have a geometrical length difference of 80 µm to enable adjustment of the MZM operating point by tuning the wavelength. The electro-optic (EO) cladding consists of the commercially available material SEO100, for which an EO coefficient of r_{33} = 160 pm/V has been demonstrated in a thin-film experiment [85]. The EO material is spin-coated onto the plasmonic MZM and a static electric field is applied across the floating ground electrodes at an elevated temperature for aligning the randomly oriented dipoles of the EO material [36]. Subsequent cooling preserves the dipole orientation even after removal of the poling field. For a plasmonic slot waveguide length of L = 20 µm, we measured an insertion loss of 16 dB. The in-device EO figure-of-merit (FoM) and the EO coefficient are estimated to be $n_{\mathrm{EO}}^3 r_{33} = 315\,\mathrm{pm/V}$ and $r_{33} = 64\,\mathrm{pm/V}$, respectively, by assuming [85] $n_{\mathrm{EO}} = 1.7$. These values are obtained from the measured $U_\pi L$-product of 240 V µm of the push-pull-operated MZM using the relation $U_\pi L = w\lambda_c / (2 n_{\mathrm{EO}}^3 r_{33} \Gamma_{\mathrm{slot}})$, Eq. (7) in Ref. [36]. In this equation, the parameters $\lambda_{\mathrm{c}} = 1.55\,\mu\mathrm{m}$ and U_π are the operating wavelength, and the measured peak-to-peak modulation voltage that is needed to drive the MZM from constructive to destructive interference at low frequencies. The calculated field interaction factor $\Gamma_{\mathrm{slot}} = 0.77$, Eq. (20) in Ref. [36], describes the interaction between the modulating RF field and the optical field. By measuring on-chip silicon nanowire waveguides of different lengths at an excitation wavelength of 1.55 µm, we estimate an insertion loss of 6.5 dB per on-chip grating coupler and a propagation loss of 0.9 dB/mm for the silicon waveguide sections.

Bandwidth measurement

The frequency response of the plasmonic modulator is measured by applying a small sinusoidal voltage with variable frequency in the range $2\,\mathrm{GHz} \le f_{\mathrm{m}} \le 0.36\,\mathrm{THz}$. The open-circuit transmission-line electrodes of the POH MZM feature a total length of about 150 µm, see Appendix A.2 for details. For evaluation of the data, we use a global normalization technique that allows to infer the overall shape of the frequency response despite strong variations in the electrical drive power for various frequency bands. The modulation signal is coupled to the POH MZM by ground-signal-ground (GSG) probes, which have a wave impedance of $Z = 50\,\Omega$. The open-circuit peak voltage U_{e} at the terminals of the POH MZM is estimated from the electric drive power P_{e} which

is available at the input of the GSG probe and is measured by replacing the probes by a power meter, see Appendix A.2 for details. To determine the phase modulation index η, we use a high-resolution optical spectrum analyzer (APEX AP2050) to determine the power of the carrier f_c and of the two first-order intensity modulation sidebands at $f_c \pm f_m$. For larger drive amplitudes, a multitude of modulation sidebands would become visible at frequencies $f_c \pm k f_m$ (k = 1,2,3,…). Assuming equal phase modulation indices η in both arms, the optical power at each frequency is given by [86] $P_o(f_c + k f_m) = P_i J_k^2(\eta)\left(1 + (-1)^k \cos\Delta\phi\right)$, where P_i is the power of the light entering the modulator, $J_k(\eta)$ is the k-th order Bessel function of the first kind, and $\Delta\phi$ is the phase difference between the two interferometer arms of the MZM that determines the operating point. The sideband-to-carrier power ratio of the first-order sidebands at $f_c \pm f_m$ and the spectral line at f_c is hence given by $R_{1,0} = P_o(f_c \pm f_m)/P_o(f_c) = \alpha J_1^2(\eta)/J_0^2(\eta)$ where $\alpha = (1-\cos(\Delta\phi))/(1+\cos(\Delta\phi))$. For small amplitudes of the modulating signal ($\eta \ll 1$), the Bessel functions can be approximated by $J_0(\eta) = 1$ and $J_1(\eta) = \eta/2$, which leads to $R_{1,0} \approx \alpha\eta^2/4$, see Appendix A.2. In order to cover the frequency range of interest, we employ various sources: For $2\,\mathrm{GHz} \le f_m \le 64\,\mathrm{GHz}$, the source of an Anritsu 37397C vector network analyzer (VNA) is used. A Keysight VNA (PNA-X, N5247) with different frequency extension modules (OML N5262-60003 and V06VNA2-T/R-A) acts as the RF source in the frequency ranges $70\,\mathrm{GHz} \le f_m \le 0.11\,\mathrm{THz}$ and $0.11\,\mathrm{THz} \le f_m \le 0.17\,\mathrm{THz}$, respectively. The frequency range $0.22\,\mathrm{THz} \le f_m \le 0.36\,\mathrm{THz}$ is covered by an electrical signal that is generated by photomixing of two detuned CW laser tones in a uni-travelling-carrier (UTC) photodiode. In the range $0.17\,\mathrm{THz} < f_m < 0.22\,\mathrm{THz}$, no source was available in our laboratory. To eliminate the impact of the frequency-dependent drive signal power, the modulation sidebands are measured together with the available electrical power P_e in front of the GSG probes, using a step size of 2 GHz for frequencies up to 0.17 THz and of 5 GHz in the frequencies from 0.22 THz up to 0.36 THz. A dedicated calibration procedure is used to ensure global comparability of the modulation indices measured in the various frequency bands, see Eq. (3.1) as well as Appendix A.2 for details. For frequencies up to 65 GHz, we use an Anritsu ML2438A power meter, whereas the power at higher frequencies is measured by a waveguide-coupled calorimeter (VDI Erickson PM4).

A.2 Frequency response of POH modulator

We characterize the frequency response of the plasmonic-organic hybrid (POH) Mach-Zehnder modulator (MZM) by measuring the output spectrum of the intensity-modulated light for different modulation frequencies and by determining the power ratio of the first-order modulation sidebands and the optical carrier. To this end, a continuous-wave (CW) optical carrier at optical frequency f_c (angular frequency $\omega_c = 2\pi f_c$) with a power $P_o = 18\,\mathrm{dBm}$ is launched into the POH MZM, which is driven with a small sinusoidal RF/THz signal at a frequency f_m, see Fig. 3.2(a) in Chapter 3. The arm lengths of the POH MZM differ by 27 µm, and the wavelength of the optical carrier is chosen to operate the device close to its the quadrature point, where the phase shift in the two arms differs by $\Delta\phi = \pi/2$ in the absence of an electrical modulation signal. The MZM is characterized in the frequency range $2\ \mathrm{GHz} \le f_m \le 0.36\ \mathrm{THz}$. Note that this frequency range is only limited by the equipment available in our lab and not by the speed of the POH MZM itself.

The intensity-modulated signal is detected by an optical spectrum analyzer (OSA, APEX AP2050, 180 MHz resolution bandwidth) which, for small electric drive signals, reveals a peak at the optical carrier frequency f_c and two first-order modulation sidebands at $f_c \pm f_m$. Assuming that the optical signals at the output of the phase-modulating arms of the MZM feature an identical phase modulation index η, the sideband-to-carrier power ratio $R_{1,0}$ of the first-order sideband and the optical carrier is given by [86]

$$R_{1,0} = \frac{P_o(f_c \pm f_m)}{P_o(f_c)} = \frac{J_1^2(\eta)\left(1-\cos\Delta\phi\right)}{J_0^2(\eta)\left(1+\cos\Delta\phi\right)}. \tag{A.1}$$

In this relation, $\Delta\phi$ denotes difference of the phase shifts in both arms in the absence of a modulating electrical signal and hence defines the operating point of the device, and J_0 and J_1 are the 0^{th} and the 1^{st}-order Bessel functions of the first kind. For small electric drive amplitudes U_e of the modulating signal $(\eta \ll 1)$, the Bessel functions can be approximated by $J_0(\eta) = 1$ and $J_1(\eta) = \eta/2$ which leads to

$$R_{1,0} = \alpha \frac{\eta^2}{4}, \quad \alpha = \frac{(1-\cos\Delta\phi)}{(1+\cos\Delta\phi)}. \tag{A.2}$$

If the modulator is operated exactly at its quadrature point $\Delta\phi = \pi/2$, then the correction factor . Exact adjustment of the operating point during the experiment, however, turned out to be difficult due to noise and distortions of the cos²-type spectral power transfer function of the unbalanced POH MZM. To reduce the associated uncertainties, we record the power transmission spectrum of the device over an extended spectral range to estimate the exact phase shift $\Delta\phi$ and hence consider the associated correction factor α for the data evaluation. To this end, we fit the measured power transmission spectrum with a model function. We assume that after eliminating the impact of the grating couplers, the power transfer function of the POH MZM is essentially given by $T(\omega) \propto \cos^2(\Delta\phi/2)$ with $\Delta\phi = \beta(\omega)\Delta L$, where $\beta(\omega)$ is the frequency-dependent propagation constant and ΔL is the path length difference between the two arms of the MZM. For fitting the measured data, we additionally allow for a non-perfect extinction ratio of the MZM, and we adopt a second-order Taylor series expansion of $\beta(\omega)$ about the center frequency ω_0 of the tuning range for taking into account chromatic dispersion. This leads to a model function of the form

$$T(\omega) = \mathrm{A}^{(0)} + \mathrm{A}^{(1)} \cos^2\left(\frac{1}{2}\left(\beta^{(0)} + \beta^{(1)}(\omega-\omega_0) + \frac{1}{2}\beta^{(2)}(\omega-\omega_0)^2\right)\Delta L\right) \tag{A.3}$$

In this relation, $\beta^{(0)}$, $\beta^{(1)}$ and $\beta^{(2)}$ denote the propagation constant, its first and its second-order derivative at the center frequency ω_0. The parameters $\mathrm{A}^{(0)}$, $\mathrm{A}^{(1)}$, $\mathrm{B}^{(0)} = \beta^{(0)}\Delta L$, $\mathrm{B}^{(1)} = \beta^{(1)}\Delta L$, and $\mathrm{B}^{(2)} = \frac{1}{2}\beta^{(2)}\Delta L$ are determined by a least-square fit of the model function to the measured transmission spectrum, see Fig. A.1. Based on these results, the phase shift $\Delta\phi_\mathrm{c} = \left(\frac{1}{2}\left(\beta^{(0)} + \beta^{(1)}(\omega_c-\omega_0) + \frac{1}{2}\beta^{(2)}(\omega_c-\omega_0)^2\right)\Delta L\right)$ is determined for each actual operating point, and used to calculate the associated correction factor α. Fig. A.1 shows the measured power transmission spectrum of the POH MZM. as a function of carrier frequency along with the associated fit according to the

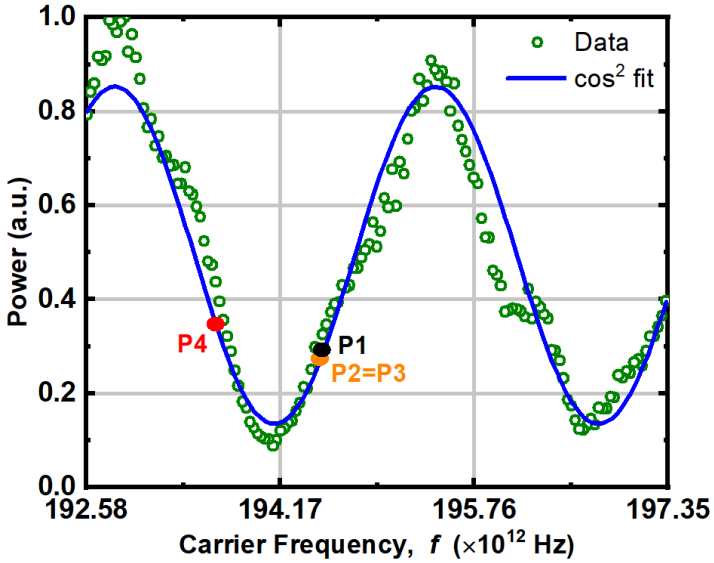

Figure A.1: Measured MZM transfer function (green circles) and associated fit (blue line) according to Eq. (S3). P_1, P_2, $P_3 = P_2$, and P_4 denote the operating points used for measuring the frequency response in the bands 2 GHz ≤ f_m ≤ 64 GHz, 0.07 THz ≤ f_m ≤ 0.11 THz, 0.11 THz ≤ f_m ≤ 0.17 THz and 0.22 THz ≤ f_m ≤ 0.36 THz respectively

Eq. (3.1). Note that the electro-optic frequency response shown in Fig. 3.2(b) in Chapter 3 is measured in four different segments, covering the frequency band $2\,\mathrm{GHz} \le f_m \le 64\,\mathrm{GHz}$, $0.07\,\mathrm{THz} \le f_m \le 0.11\,\mathrm{THz}$, $0.11\,\mathrm{THz} \le f_m \le 0.17\,\mathrm{THz}$ and $0.22\,\mathrm{THz} \le f_m \le 0.36\,\mathrm{THz}$, respectively. Each of these measurements are performed on a slightly modified setup, leading to slightly different operating points that are denoted as P_1, P_2, $P_3 = P_2$, and P_4 in Fig. A.1.

To drive the modulator, we use an external RF/THz source that is connected to the un-terminated on-chip coplanar transmission line of the POH MZM using a 50 Ω ground-signal-ground (GSG) probe. In order to estimate the open-circuit peak voltage U_e of the electrical signal that is effective at the POH MZM, we first measure the available electrical power P_e at the input terminals of the GSG probe taking into account losses from various components used in the setup such as cables, connectors, or THz waveguides. For this purpose, we use a calibrated power meter (Anritsu ML2438A) for $2\,\mathrm{GHz} \le f_m \le 64\,\mathrm{GHz}$ and a waveguide-coupled calorimeter (VDi Erickson PM4) for $64\,\mathrm{GHz} \le f_m \le 0.36\,\mathrm{THz}$. We further need to take into account the losses that the THz signal experiences

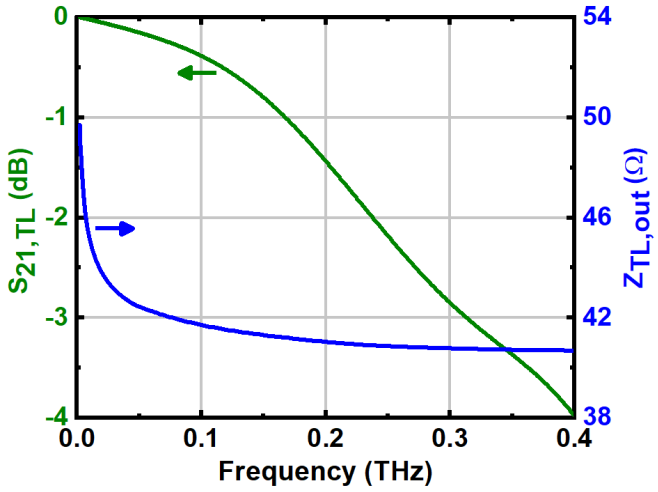

Figure A.2: Simulated RF/THz characteristics of the on-chip tapered transmission line
The frequency-dependent insertion loss $S_{21,\mathrm{TL}}$ and line impedance $Z_{\mathrm{TL,out}}$ of the tapered coplanar transmission line are obtained using CST Microwave Studio

during on-chip propagation along the 150 µm-long tapered coplanar transmission line from the probe pads to the POH MZM. To this end, we use a commercially available simulation tool (CST Microwave Studio) to calculate the transmission parameter $S_{21,\mathrm{TL}}$ of the tapered transmission line, see green trace in Fig. A.2. Moreover, we need to take into account that the line impedance changes along the transmission line taper from an initial value of $Z_{\mathrm{TL,in}} \approx 50\,\Omega$ at the input to a frequency-dependent impedance $Z_{\mathrm{TL,out}}$ at the output, which is also extracted from the numerical simulation, see blue trace in Fig. A.2. Taking into account the insertion loss of the GSG probe $S_{21,\mathrm{Probe}}$ from the datasheet of the manufacturer, the power available at the terminals of the POH modulator can be calculated as $P_{\mathrm{POH}} = P_{\mathrm{e}} \left|S_{21,\mathrm{Probe}}\right|^2 \left|S_{21,\mathrm{TL}}\right|^2$. The open-circuit peak drive voltage of the modulating signal at the terminal of the POH MZM is then given by $U_{\mathrm{e}} = 2\sqrt{2 \times Z_{\mathrm{TL,out}} \times P_{\mathrm{POH}}}$.

To cover the various frequency bands, we use four different GSG probes, which are specified for operation in designated frequency bands: (i) Cascade Microtech Inc. I67-GSG-100 (S/N: HF298) for $2\,\mathrm{GHz} \le f_{\mathrm{m}} \le 64\,\mathrm{GHz}$, (ii) Cascade Microtech Inc. I110-A-GSG-100 (S/N: DV27T) for $0.07\,\mathrm{THz} \le f_{\mathrm{m}} \le 0.11\mathrm{THz}$, (iii) Cascade Microtech Inc. I170-T-GSG-100-BT (S/N: HK254) for $0.11\mathrm{THz} \le f_{\mathrm{m}} \le 0.17\,\mathrm{THz}$ and (iv) Model 325B from GGB Industries Inc. for $0.22\,\mathrm{THz} \le f_{\mathrm{m}} \le 0.36\,\mathrm{THz}$. The insertion losses $(S_{21,\mathrm{Probe}})$ of the GSG probes are obtained from the respective datasheets. In the frequency range

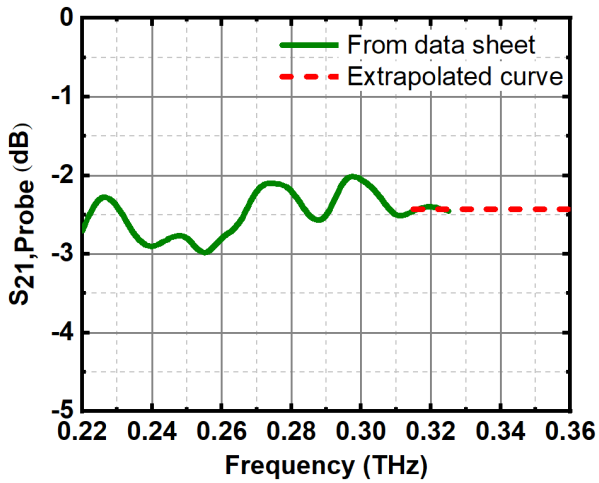

Figure A.3: Insertion loss of the THz GSG probe. S_{21} parameter of the THz probe (GGB, Model 325B) as used for calculating the peak electrical drive voltage. The green curve shows the values from the datasheet of the GSG probe and the dashed red curve is an extrapolation in the frequency range between 0.325 THz and 0.36 THz. Note that extrapolation by an essentially flat frequency response is a conservative estimation: assuming a frequency-dependent decay of the S_{21} parameter would lead to a decrease of the drive voltage that is assumed to be effective at the modulator. This would result in an increase of the normalized MZM frequency response in Fig. 3.2(b), that is obtained from dividing the measured phase modulation index by the estimated drive voltage amplitude

$0.325\,\mathrm{THz} \leq f_\mathrm{m} \leq 0.36\,\mathrm{THz}$, the insertion loss of the THz probe (GGB, Model 325B) is estimated by extrapolating the values from the datasheet, see Fig. A.3. Moreover, we need to account for the fact that the drive power P_e from our signal sources shows a strong dependency with respect to the modulation frequency f_m and hence results in a strongly frequency-dependent modulation index $\eta(f_\mathrm{m})$. The measured phase modulation index $\eta(f_\mathrm{m})$ and the calculated electrical drive voltage $U_\mathrm{e}(f_\mathrm{m})$ for each frequency band are shown in Fig. A.4(a) – (d). Since the phase modulation index η is proportional to the electric drive voltage U_e, we can eliminate the impact of the frequency-dependent drive power $P_\mathrm{e}(f_\mathrm{m})$ by considering the ratio $\eta(f_\mathrm{m})/U_\mathrm{e}(f_\mathrm{m})$. Normalizing the frequency characteristic of this ratio to its value at a reference modulation frequency of $f_\mathrm{m,ref} = 2\,\mathrm{GHz}$, we obtain the dimensionless normalized phase modulation index according to the Eq. (3.1) in the Chapter 3.

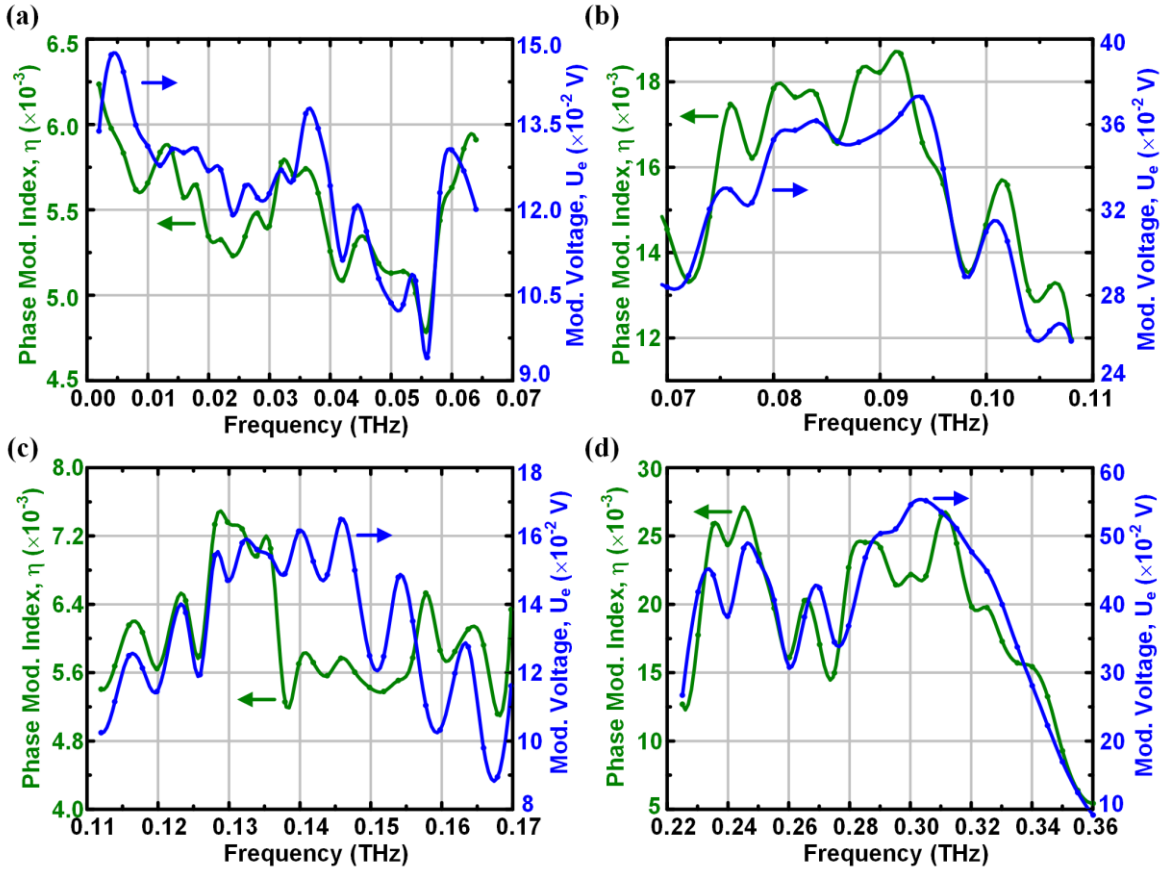

Figure A.4: Frequency-dependent phase modulation indices η (green traces) of the MZM and associated voltage amplitudes U_e (blue traces) of the electric drive signals for various frequency bands. (a) 0.002 THz to 0.07 THz; (b) 0.07 THz to 0.11 THz; (c) 0.11 THz to 0.17 THz; (d) 0.22 THz to 0.36 THz. It can be observed that η is essentially proportional to U_e, as expected from theory.

$$\eta_U(f_\mathrm{m}) = 20\log_{10}\left(\frac{\eta(f_\mathrm{m})/U_\mathrm{e}(f_\mathrm{m})}{\eta(f_\mathrm{m,ref})/U_\mathrm{e}(f_\mathrm{m,ref})}\right) \tag{A.4}$$

The normalization according to Eq. (A.4) allows to infer the global electro-optic (EO) response of the POH MZM measured in various frequency bands, leading to the results shown in Fig. 3.2(b) in the Chapter 3. From these results it can be observed that the plasmonic MZM has a flat frequency response exceeding

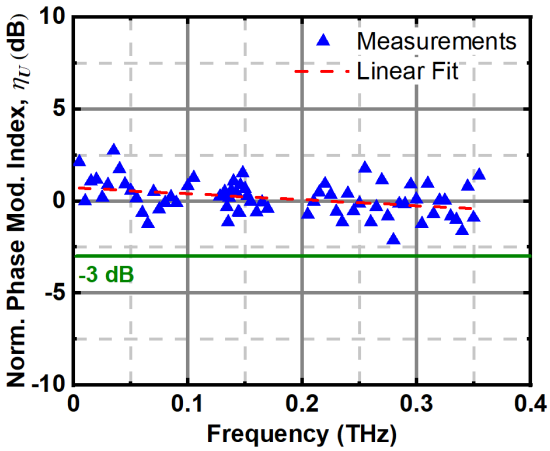

Figure A.5: Normalized phase modulation index η_U of a second-generation POH MZM. The device is based on the nominally same design as in Fig. 3.2(b) in the Chapter 3**,** but uses the organic material YLD124 as an EO cladding rather than SEO100. While measurements confirm the ultra-broadband characteristics of a POH MZM, featuring a flat frequency response until at least 0.355 THz, it also shows variations that have approximately the same magnitude but are otherwise not correlated with the ones seen in Fig. 3.2(b) shown in the Chapter 3.

0.36 THz with no sign of bandwidth limitation. Our findings emphasize the fact that the POH modulators are capable of modulating THz frequencies, as predicted in the literature [34], [36], and are in line with previous experiments [77] that demonstrated operation of POH modulators at frequencies up to 0.17 THz. Note, however, that in the work presented in [77], the frequency response was measured in different frequency bands and the results for each band were then independently normalized to the mean of all data points of the specific band. This technique does not relate the measured modulation index to the actual electric drive amplitude in an extended frequency range and hence makes it difficult to infer the overall frequency roll-off of the modulator transfer function. We overcome this problem by using the global normalization technique presented in the preceding paragraphs.

The normalized transfer function shown in Fig. 3.2(b) of the Chapter 3 exhibits noticeable variations of approximately $\pm 2.5\mathrm{dB}$. Such variations can be observed in all our transfer-function measurements, but they vary from measurement to measurement and hence cannot be attributed to an intrinsic behavior of the POH MZM. As an example, Fig. A.5 shows the results of an independent measurement of a second-generation POH MZM, which is nominally identical

to the first one that is used for the bandwidth measurements shown in Fig. 3.2(b), except that it relies on YLD124 as an organic EO material [134] rather than on SEO100. The measurement of the second-generation device also shows an EO bandwidth of more than 0.35 THz, but also exhibits variations that have approximately the same magnitude but are otherwise not correlated with the ones seen in Fig. 3.2(b) of Chapter 3. We hence attribute these ripples to measurement uncertainties, and not to an intrinsic behavior of the POH MZM. As a main source of uncertainty, we identify both the measurement of the frequency-dependent THz drive power and the power measurement of the intensity-modulated optical carrier and its sidebands. The THz power was measured with a calorimeter (VDi Erickson PM4, for $f_{\mathrm{m}} > 70\,\mathrm{GHz}$) and is subject to uncertainties due to reflections and limited repeatability of the waveguide flange connections. In addition, we observe a drift of the calorimeter of the order of 10…20 µW over a few minutes [135], leading to noticeable errors especially for THz power levels below 100 µW, e.g., in the frequency band from 0.11 THz to 0.17 THz. The measurement of the phase modulation index η, obtained from the sideband-to-carrier power ratio, is also subject to uncertainties because the sideband power levels are small, typically of the order of –40…–50 dBm, due to the small THz power of the driving source. The sideband powers are measured with an optical spectrum analyzer (APEX AP2050) having a resolution bandwidth of 180 MHz, which was necessary to suppress amplified spontaneous emission (ASE) noise originating from the erbium-doped fiber amplifier (EDFA) used in the experiment. When repeatedly scanning the same optical sideband, we observe power variations of up to ± 1 dB, which translate directly into similar variations of the estimated modulation index η_U, see Eq. (A.4). Moreover, small ripples in the optical transfer function due to reflections between the on-chip optical grating couplers may also influence the measured optical sideband power and therefore the extracted η_U. All these effects contribute to the measured ripples in the frequency response of the POH MZM. Additional uncertainties may arise from the THz transmission lines used to feed the modulator. These transmission lines comprise several connectors and the hollow waveguide sections with tapers and flanges, where small reflections and hence ripples in the transfer function could occur.

Note that the POH MZM used for the bandwidth measurement shown in Fig. 3.2 in the Chapter 3 is a first-generation device with non-optimized on-chip passive

components. The overall fiber-to-fiber insertion loss of the device amounts to about 38 dB, measured at the highest transmission of the grating couplers. This comprises a 12 dB intrinsic insertion loss of the POH phase shifters, a 24 dB of loss that originates from non-optimum grating couplers (12 dB per coupler), and an additional loss of 2 dB due to on-chip waveguides and multi-mode interference (MMI) couplers. Moreover, a non-optimum poling of the EO polymer (SEO100) resulted in a rather high π-voltage of this device (about 30 V), while the available wideband-tuneable electric sources used for driving the devices typically deliver rather small on-chip powers P_{POH} down to 25 µW. This corresponds to on-chip voltage swings with amplitudes U_{e} of 0.1 V, leading to sideband-to-carrier power ratios of –52 dB and phase modulation indices as small as 5×10^{-3} rad. In combination with the 38 dB optical insertion loss, this leads to weak sidebands that are 90 dB below the optical input power of around 18 dBm, as measured in the fiber just before the modulator. For detection of these small sidebands powers in our bandwidth measurement experiment, we use an EDFA with a gain of 30 dB in combination with a high-resolution (180 MHz) optical spectrum analyzer to effectively suppress the ASE noise of the EDFA. Note that there is a vast potential to considerably reduce the π-voltage of the POH MZM, see Appendix A.6, and also the overall insertion loss of the device, see Appendix A.7. As an example, we rely on grating couplers with reduced etch depth for the second generation of our devices, leading to an insertion loss of 6.5 dB per fiber-to-chip interface – much lower than the 12 dB measured for our first-generation devices. This was not only an important step towards the data transmission experiments shown in Fig. 3.3 in the Chapter 3, but also allowed us to omit the EDFA for subsequent bandwidth measurements that are shown in Fig. A.5.

A.3 Characterization of uni-travelling-carrier photodiode and THz amplifiers

The frequency response of the uni-travelling-carrier photodiode (UTC-PD) employed in the data transmission experiments is characterized using the setup de

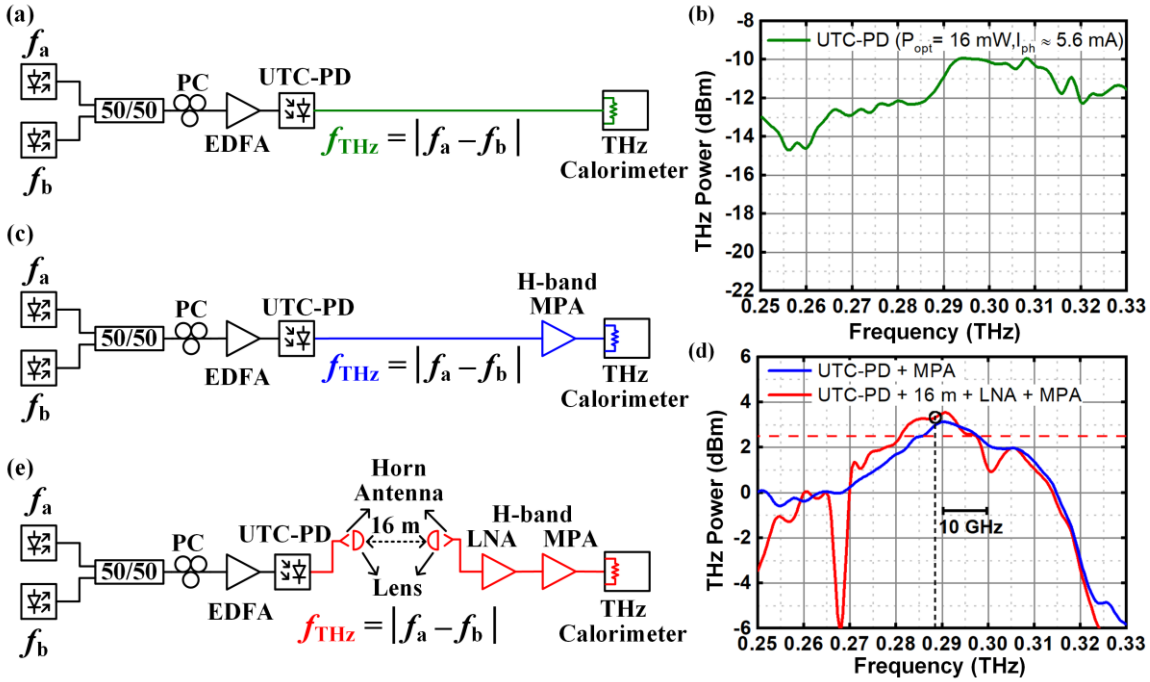

Figure A.6: Setup for characterizing various THz components used in the data transmission experiment. For all the measurements, the optical input power to the uni-travelling-carrier photodiode (UTC-PD) is set to $P_{opt} = 16$ mW which corresponds to a direct photocurrent of $I_{ph} = 5.6\,\text{mA}$. **(a)** Setup for measuring the THz output power of the UTC-PD **(b)** Frequency-dependent THz power of UTC-PD as measured by calorimeter **(c)** Setup for measuring the available THz power after amplification by H-band medium-power amplifier (MPA). **(d)** Frequency-dependent THz power for the combination of UTC-PD and MPA (blue curve). **(e)** Setup for measuring the THz power available after a free-space transmission distance of 16 m and a cascaded amplification stage, comprising a low-noise amplifier (LNA) and the MPA. The available THz power as a function of frequency is shown as the red curve in **(d)**. The kinks in the red curve are attributed to imperfect waveguide connector flanges. A horizontal red dashed line indicates a minimum THz power of 2.5 dBm that was needed at 20 GBd to achieve a BER of 4.5×10^{-3}, corresponding to the threshold for forward-error correction (FEC) with 7 % coding overhead, see Fig. 3.2(d) in the Chapter 3. The operating frequency of the THz communication link for the data transmission experiments is marked with a circle and a vertical line.

picted in Fig. A.6(a). Light from two detuned external-cavity lasers (ECL, Agilent N7714A) emitting identical polarizations with similar optical powers at frequencies $f_a = 193.0\,\text{THz}$ and $f_b = 193.3\,\text{THz}$ is combined in a polarization maintaining 3 dB coupler. The superimposed signal is amplified to an optical power P_{opt} and then fed to the UTC photodiode for photomixing to generate a continuous-wave (CW) THz signal at a frequency $f_{THz} = |f_a - f_b| = 0.3\,\text{THz}$. A

polarization controller (PC) is used to adjust the polarization of the superimposed beat signal for maximizing THz output signal of the polarization-dependent UTC-PD. The frequency of the CW THz signal is tuned from 0.25 THz to 0.33 THz by varying the optical frequency f_a, and the resulting THz output power P_{THz} is measured with a waveguide-coupled calorimeter (VDi, Erickson PM4). Fig. A.6(b) shows the measured THz output power as a function of the generated THz frequency f_{THz} for an input optical power of $P_{opt} = 16\,\mathrm{mW}$, which generates a direct photocurrent of $I_{ph} = 5.6\,\mathrm{mA}$ in the reverse-biased UTC-PD.

Next, we add an H-band medium-power amplifier (MPA, M145AMPH) with a 15 dB gain at 0.3 THz and a saturation output power +4 dBm to the setup to measure the total available THz power after amplification, see Fig. A.6(c). The THz amplifier is a millimeter-wave monolithic integrated circuit (MMIC) based on metamorphic high-electron-mobility transistor (mHEMT) technology [136]. Fig. A.6(d) shows the measured THz power as a function of frequency for the combination of UTC-PD and MPA (blue curve). Finally, we use the setup depicted in Fig. A.6(e) to measure the available THz power after a free-space transmission of 16 m. The UTC-PD transmitter is connected to a horn antenna (26 dBi gain), which radiates the THz signal into free-space. A polytetrafluoroethylene (PTFE) lens is used to collimate the beam that is emitted by the horn antenna. At the receiver, a similar PTFE lens focuses the THz signal to another horn antenna (26 dBi gain). A low-noise H-band amplifier (LNA, M145ALNH) with a gain of 26 dB at 0.3 THz (9 dB noise figure, −30 dBm maximum input power) cascaded with the previously mentioned H-band MPA is used to compensate the free-space loss of the THz signal. The red curve in the Fig. A.6(d) shows the THz available power at the receiver after a transmission distance of d = 16 m and subsequent amplification by the combination of LNA and MPA. The dips in the red curve are attributed to reflections of the THz carrier due to imperfect waveguide connector flanges between the amplifiers. The operating frequency $f_{Tx,THz} = 0.2885\,\mathrm{THz}$ of the THz data transmission experiments is marked with a circle and a dashed vertical line. In our experiments, the free-space path loss (FSPL) of the wireless link would amount to approximately 106 dB according to the relation $\mathrm{FSPL} = 10\log_{10}\left(c/4\pi f_{Tx,THz} d\right)^2$ where c is the vacuum speed of light. From the measurements of the received power, we

estimate that the combination of transmitter-receiver lens-and-horn antenna feature a gain of ~ 79 dBi compared to an isotopic antenna, see Appendix A.4.

In the transmission experiment, presented in Fig. 3.3 of the Chapter 3, a minimum THz power of approximately 2.5 dBm was needed at 20 GBd to achieve a BER of 4.5×10^{-3}, corresponding to the threshold for forward-error correction (FEC) with 7 % coding overhead. This power level refers to the waveguide input of the THz GSG probe and was estimated by taking the minimum THz power within the spectral range occupied by the 20 GBd signal, which is indicated a dashed horizontal line in Fig. A.6(d). Taking into account the GSG probe losses depicted in Fig. A.3, this corresponds to an on-chip THz drive power of approximately 0 dBm. Note that the THz power level required to reach the FEC threshold and the associated signal-to-noise power ratio (SNR) increases in proportion to the symbol rate.

A.4 Setup for data transmission experiments

A detailed sketch of the THz transmitter (Tx) for optical-to-THz (O/T) conversion is depicted in Fig. A.7(a). A software-driven digital-to-analog converter (DAC, Keysight M9505A, sampling frequency 90 GSa s^{-1}) is used to generate drive signals for QPSK modulation using a pseudo-random binary sequence (length $2^{11} - 1$). The signals are shaped to Nyquist pulses featuring a raised-cosine spectrum and a roll-off factor of $\beta = 0.1$. The resulting analog signal is fed to an optical IQ-modulator that is fed by a CW carrier generated by an external-cavity laser (ECL) at an optical frequency $f_0 = 193.3\,\mathrm{THz}$. The IQ-modulator is biased at its zero-transmission point in order to suppress the optical carrier at frequency f_0. The intensity-modulated optical signal is amplified using an erbium-doped fiber amplifier (EDFA). Out-of-band amplified spontaneous emission noise from the EDFA is blocked by an optical band-pass filter (0.6 nm passband width) before superimposing the modulated optical carrier with a CW local-oscillator (LO) tone at a frequency $f_{\mathrm{Tx,LO}}$ derived from another ECL. The power of the CW tone at $f_{\mathrm{Tx,LO}}$ is adjusted to the same level as the average power of the modulated signal. The combined signal is further amplified by a second EDFA, polarization-adjusted, and then fed into a variable optical attenuator (VOA). The CW tone and the optical data signal are mixed in

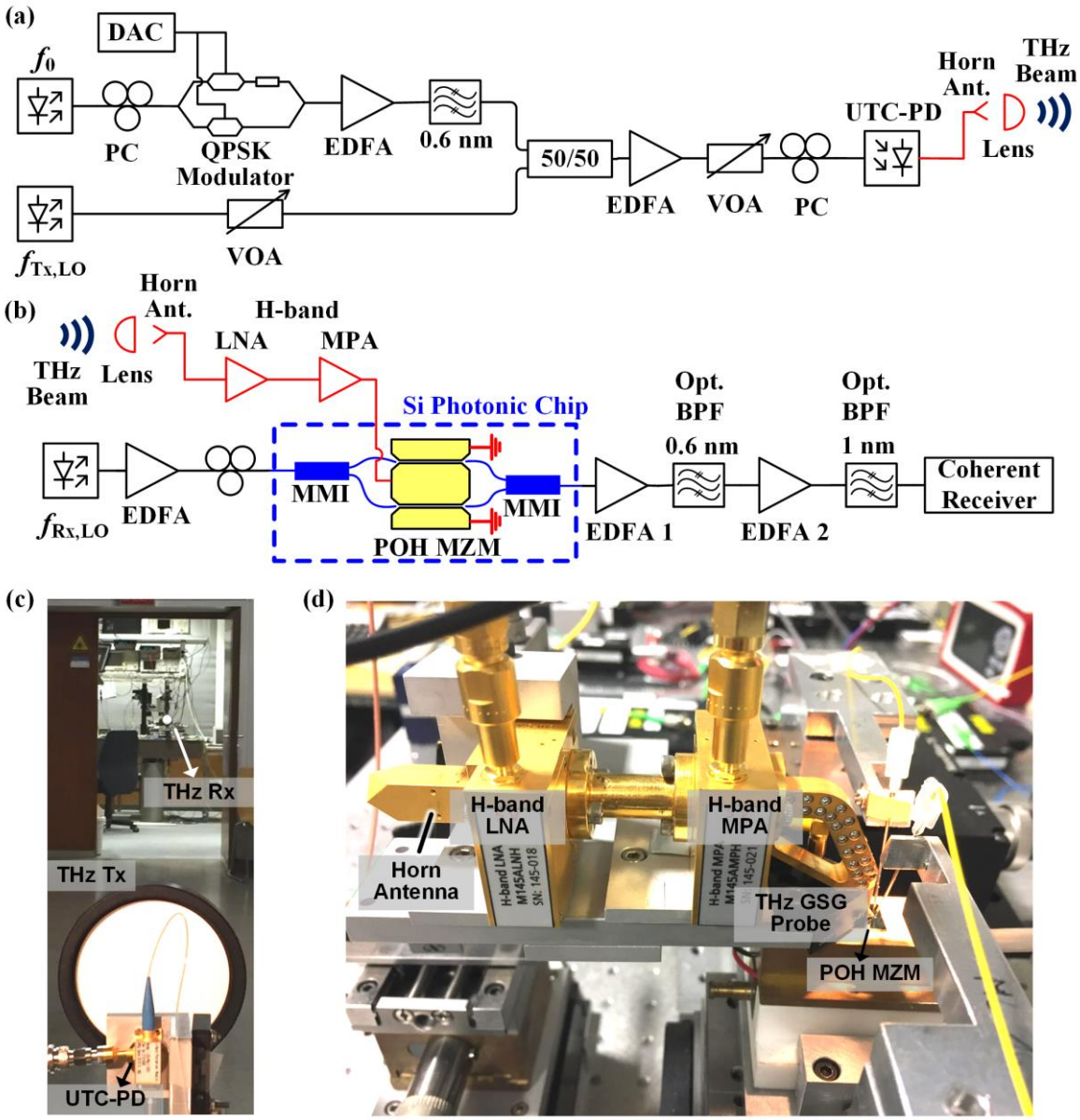

Figure A.7: Detailed setup of the THz transmitter and receiver used for data transmission experiments. (a) Setup of the wireless terahertz transmitter that generates a QPSK data signal on a carrier frequency of $f_{\mathrm{Tx,THz}} = 0.2885\,\mathrm{THz}$ by exploiting photomixing in a uni-travelling-carrier photodiode (UTC-PD) for optical-to-THz (O/T) conversion. The THz signal is radiated into free-space by a horn antenna. A subsequent polytetrafluoroethylene (PTFE) lens is used to collimate the THz beam. **(b)** Setup for terahertz-to-optical (T/O) conversion at the THz receiver using a plasmonic Mach-Zehnder modulator (MZM). The incoming signal is focused into a horn antenna by a second PTFE lens. It is then fed to a cascade of THz (H-band) amplifiers, which drive the POH MZM, thereby modulating the signal onto an optical carrier. A cascade of EDFA and optical band-pass filters (BPF) is used to amplify the intensity-modulated optical signal and to isolate one of the sidebands. Note that, due to the limited tuning range of the optical filter used in this experiment, we chose to isolate the lower sideband of our

optical signal rather than the upper one, as sketched in Fig.3.1(c) in the Chapter 3. **(c)** Photograph of the data transmission setup showing the THz Tx and the Rx. Tx and Rx are built up in different laboratories, separated by 16 m of free-space transmission distance across the hallway. **(d)** Photograph of the THz photonic Rx. The wireless signal is focused by a PTFE lens (not shown), then coupled into the horn antenna and amplified by the dual-stage H-band amplifier, which drive the POH MZM through the ground-signal-ground (GSG) probe. DAC – digital-to-analog converter, PC – polarization controller, MMI – multimode interference coupler, EDFA – erbium-doped fiber amplifier, VOA – variable optical attenuator, LNA – low-noise amplifier, MPA – medium-power amplifier

a UTC-PD, resulting in a THz QPSK data stream at a carrier frequency $f_{\mathrm{Tx,THz}} = \left| f_0 - f_{\mathrm{Tx,LO}} \right| = 0.2885\,\mathrm{THz}$. The polarization of the superimposed signal entering the polarization-sensitive UTC-PD is adjusted to maximize the THz output power. This THz transmitter implementation provides the flexibility of tuning the THz carrier frequency $f_{\mathrm{Tx,THz}}$ over a broad frequency range, only limited by the bandwidth of the UTC-PD, by adjusting the frequency $f_{\mathrm{Tx,LO}}$ of the unmodulated LO tone. The THz output power provided by the UTC-PD typically amounts to −11 dBm. A conical horn antenna with a gain of 26 dBi and an aperture diameter of 5.6 mm is attached directly to the UTC-PD to radiate the THz signal into free-space. The radiated signal is collimated by a plano-convex PTFE lens (diameter – 101.6 mm and focal length – 200 mm) and is sent over a wireless transmission distance of 16 m.

Figure A.7(b) shows the THz receiver (Rx) setup used for THz-to-optical (T/O) conversion. Light emitted by an ECL at a frequency $f_{\mathrm{Rx,LO}}$ is amplified to a power of 18 dBm by an EDFA and then launched into the POH MZM using an on-chip grating coupler on the silicon (Si) photonic chip. The on-chip insertion loss of the MZM with 20 µm -long POH phase shifter amounts to 16 dB. The grating couplers and the on-chip waveguides contribute to an additional loss of 14 dB, with vast potential for further reduction by using optimized passive silicon photonic devices. The passive silicon photonic waveguides feeding the POH MZM have a length difference of 80 µm and hence enable the adjustment of the quadrature (3 dB) operating point of the POH MZM by tuning the wavelength. Alternatively, the operating point of the POH MZM could be set by applying a DC bias or by additional phase shifters in the silicon photonic waveguides of the MZM arms. For wireless reception, the THz QPSK data stream is focused to a horn antenna (26 dBi gain) by a PTFE plano-convex lens similar

to the one used in the THz transmitter setup. A cascaded combination of H-band LNA and MPA boosts the power of the THz signal and drives the POH MZM through a THz GSG probe (GGB, Model 325B). The intensity-modulated signal out of the plasmonic modulator is coupled out of the chip using another grating coupler and then amplified by an EDFA. One of the modulated sidebands of the amplified signal at a frequency $f_{\mathrm{Rx,LO}} \pm f_{\mathrm{Tx,THz}}$ is filtered with a 0.6 nm band-pass filter and sent through a second amplification stage, where the optical signal is further amplified to a power of 1 dBm. The resulting signal is again filtered with a 1 nm band-pass filter to additionally suppress the optical carrier and one of the modulation sidebands before being detected by a coherent optical receiver (Agilent optical modulation analyzer N4391A, OMA). The received electrical signal is recorded by a real-time oscilloscope (32 GHz analog bandwidth) and evaluated off-line using digital signal processing (DSP). After resampling and clock-recovery, the recorded data is equalized using a constant-modulus algorithm. The phase of the carrier is estimated based on a Viterbi-Viterbi algorithm, and the bit error ratio (BER) is computed as a final step.

Figure A.7(c) shows a photograph of the THz communication link with the transmitter and receiver separated by 16 m. The THz beam path contains a horn antenna and a plano-convex PTFE lens on each side. Figure A.7(d) shows a photograph of the THz receiver, comprising a horn antenna and a combination of H-band LNA and MPA which drive the POH MZM through a THz ground-signal-ground (GSG) probe. From the free-space path loss (FSPL) of approximately 106 dB, see Appendix A.3, we estimate that the directivity gain of each antenna-lens combination is approximately 40 dBi. We later realized that the insertion loss of the THz beam path could be further reduced by more careful alignment of the components, leaving room for further increasing the performance of the transmission link.

A.5 Signal impairment analysis

In contrast to conventional optical transmission links, the quality of the T/O-converted signal in our demonstration is dictated by the quality of the modulating THz signal and not so much by the optical transmission link. Specifically, the THz signal might be subject to impairments like frequency-dependent losses

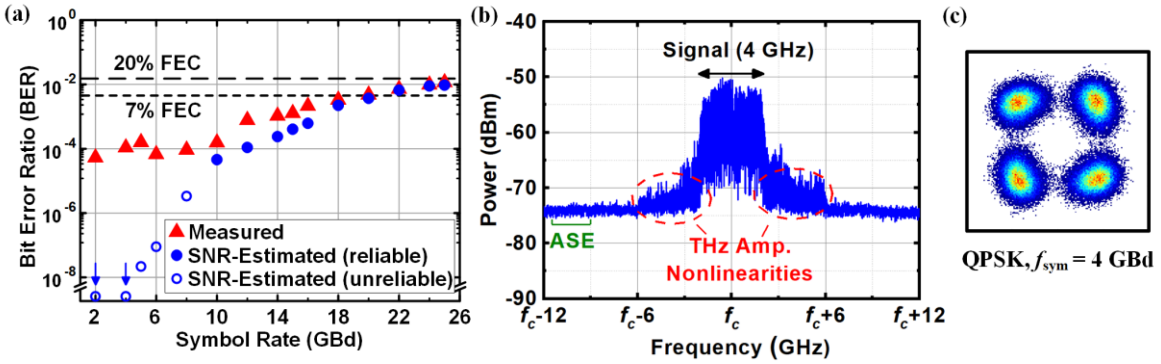

Figure A.8:BER and signal impairment analysis. (a) Bit error ratio (BER) of QPSK signals at different symbol rates upon T/O conversion and coherent optical reception. The red triangles denote the measured BER, while the filled blue circles represent BER values that can be reliably estimated from the SNR of the received signal according to Eq. (A.6). The open blue circles correspond to SNR-based estimations that become increasingly unreliable for $\mathrm{BER} \leq 10^{-5}$. For high symbol rates, the measured BER fits well with the theoretical estimations, indicating that the SNR is limited by the ASE noise of the EDFA. For smaller symbol rates, however, the measured BER differs strongly from the (unreliably) estimated ones, due to nonlinearities of the THz amplifiers and due to phase-noise of the LO laser used in the coherent Rx. **(b)** Spectrum showing nonlinear signal impairments of a 4 GBd QPSK signal at the coherent receiver. The spectrum exhibits noticeable 'pedestals' on both sides of the actual data signal, caused by nonlinearities of the THz amplifiers, which are operated close to their saturation output power. **(c)** Constellation map of the 4 GBd QPSK signal with elongated constellation points indicating phase noise from the free-running laser used for coherent reception.

of the free-space path, electrical noise of the THz amplifiers, or bandwidth limitations of the O/T and T/O converters. Due to these fundamental differences to classical fiber-optic transmission schemes, it is difficult to compare the constellation diagrams shown in Fig. 3.3(e) of the Chapter 3 with those of conventional optical transmission links. In the following, we present a detailed analysis of our data transmission demonstration and the corresponding results are shown in Fig. A.8.

For high symbol rates, we find that the dominant signal impairments are introduced when amplifying the weak optical output signal of the POH MZM by an erbium-doped fiber amplifier, which is labelled as EDFA 1 in Fig. A.7(b). The signal-to-noise power ratio (SNR) at the optical receiver can be calculated from the ratio of the optical signal power P_s and the noise power density N_0 within the signal bandwidth B, and the error vector magnitude (EVM) can be estimated assuming data-aided reception according to the relation [137]–[139]

$$\mathrm{SNR} = \frac{P_s}{N_0 B}, \qquad \mathrm{EVM} \approx \left(\mathrm{SNR}\right)^{-1/2} \tag{A.5}$$

In this relation, N_0 denotes the power spectral density of the amplified spontaneous emission (ASE) background that is co-polarized with the signal. We estimated the BER of the QPSK signal from the estimated data-aided EVM using the (corrected [138]) Eq. (4) in [137],

$$\mathrm{BER} = \frac{1}{2}\mathrm{erfc}\left(\sqrt{\frac{1}{2\,\mathrm{EVM}^2}}\right) \approx \frac{1}{2}\mathrm{erfc}\left(\sqrt{\frac{\mathrm{SNR}}{2}}\right) \tag{A.6}$$

Note that the BER estimation according to Eq. (A.6) relies on the assumption that the signal is dominantly impaired by additive white Gaussian noise (AWGN). It can be deduced from Fig. 3b in Ref. [137] that the BER estimate according to Eq. (A.6) is reliable for $10^{-5} \le \mathrm{BER} \le 10^{-2}$ but the BER is increasingly under-estimated and hence unreliable for $\mathrm{BER} \le 10^{-5}$ as the difference in the EVM between data-aided and non-data-aided reception becomes significant [137]. The results of this reliable estimation of BER are depicted as filled blue circles in Fig. A.8(a) while the under-estimated and unreliable BER is represented by open blue circles. For high symbol rates, the BER estimate is consistent with the BER that we actually measure in our experiments, indicated as red triangles in Fig. A.8(a). This shows that the ASE background introduced by EDFA 1 is the main source of signal impairment. For low symbol rates, however, the directly measured BER is much higher than the (unreliably) estimated ones from the SNR. This is attributed to additional signal impairments that cannot be described only by an AWGN background.

To understand these additional impairments, we investigate the signal spectra as well as the QPSK constellation diagrams for signals with smaller symbol rates. As an example, the signal spectrum and the respective constellation diagram for a 4-GBd QPSK signal after T/O conversion and coherent optical detection are shown in Fig. A.8(b) and (c). The spectrum exhibits an additional "pedestal", encircled with broken red lines, Fig. A.8(b), which peaks out of the white-noise background. We attribute this pedestal to nonlinear distortions caused by third-order intermodulation products in the THz amplifiers that were operated close to their saturation output power. These impairments are also present at higher symbol rates where the signal spectrum is wider and has a smaller

power spectral density. In this case, however, the nonlinearity-generated spectral parts have a correspondingly reduced spectral power density and are therefore masked by the white-noise background. Moreover, despite the use of advanced phase tracking algorithms in our post-processing routines, the signals at low symbol rates are impaired also by phase noise, which can be inferred from the azimuthally elongated constellation points in Fig. A.8(c). This phase noise originates from the finite coherence time of the free-running LO laser used for coherent reception of the QPSK signal and its impact increases with decreasing symbol rate [140].

A.6 POH modulator performance and potential for improvements

The POH MZM described in Chapter 3 is an experimental device that still leaves significant room for further performance improvements. The following section presents various performance metrics and the underlying theoretical limits, and discusses the path for future improvements.

In general, plasmonic-organic hybrid (POH) modulators stand out due to an ultra-small π-voltage-length product $U_\pi L$. This is a consequence of the strong optical confinement within the nano-scale slot, and of the high EO activity of the organic cladding materials [36], [88]. The π-voltage-length product of a push-pull MZM is calculated according to Eq. (7) in [36] as

$$U_\pi L = \frac{w\lambda_c}{2n_{\mathrm{EO}}^3 r_{33}\Gamma_{\mathrm{slot}}}, \tag{A.7}$$

where $\lambda_c = 1.55\,\mu\mathrm{m}$ is the operating wavelength, w is the slot-width, Γ_{slot} is the field interaction factor describing the interaction between the modulating RF field and the optical field, and $n_{\mathrm{EO}}^3 r_{33}$ is the EO figure-of-merit. In the device used in our transmission experiments, the $U_\pi L$ product amounts to 240 Vμm, which is been achieved with a slot width of 75 nm, a field interaction factor of $\Gamma_{\mathrm{slot}} = 0.77$, and a moderate electro-optic coefficient of $r_{33} = 64\,\mathrm{pm/V}$ ($n_{\mathrm{EO}}^3 r_{33} = 315\,\mathrm{pm/V}$). This leaves vast room for improvement: the field interaction factor can be increased to values [36] of approximately 0.9 by using a metal thickness of 180 nm along with — technically still feasible — slot widths

down to 60 nm. In addition, organic EO materials have recently been demonstrated to exhibit EO coefficients in excess of $r_{33} = 390\,\mathrm{pm/V}$ ($n_{\mathrm{EO}}^3 r_{33} = 2300\,\mathrm{pm/V}$), enabled by theory-guided molecular optimization of EO chromophores [26]. Together, this would reduce the π-voltage-length product to values below 35 Vμm at a wavelength of 1.55 μm, corresponding to a seven-fold improvement compared to our current device. The feasibility of devices with $U_\pi L$ products down to an impressive 50 Vμm at $\lambda_c = 1.55\,\mu\mathrm{m}$ has been previously demonstrated [90], but these devices were not tested with respect to high-frequency modulation.

Ultra-small $U_\pi L$ products are also of highest importance when it comes to optical insertion loss – one of the most crucial performance limitations of POH modulators. Since the plasmonic devices suffer from significant optical propagation losses in the metal slot waveguide, the phase shifter section has to be kept short, typically with lengths of the order of a few tens of micrometers. This leads to a fundamental trade-off between low insertion loss and low π-voltage U_π, which can be quantified by the product of the propagation loss *a*, expressed in dB/μm, and the $U_\pi L$ product in V μm, resulting in a π-voltage-loss product $aU_\pi L$, expressed in V dB. Our current POH MZM features a $U_\pi L$ product of 240 Vμm and a propagation loss of *a* = 0.8 dB/μm corresponding to a $aU_\pi L$ product of about 190 V dB. The propagation loss may be reduced to about 0.2 dB/μm by using optimized metal deposition techniques [133] and by resorting to alternative materials which feature smaller plasmonic losses, for example silver. Together with the aforementioned possible reduction of the $U_\pi L$ product to 35 Vμm, this would permit more than a 25-fold improvement of the $aU_\pi L$ product, leading to values of the order of 7 V dB. Note that these $aU_\pi L$ products are even smaller than those of state-of-the-art silicon depletion-type modulators, which typically [13], [141] exceed 10 V dB.

The most attractive feature of POH modulators is the ultra-high modulation bandwidth, which is enabled by the small device footprint and by the ultra-small capacitance, which is of the order of a few fF. Assuming a signal source with a 50 Ω internal impedance and a 3 fF capacitance as estimated for our device, this would lead to RF cutoff frequency [36] in excess of 1 THz. This is in good agreement with the bandwidth measurements presented in Fig. 3.2(b) of the Chapter 3. These measurements do not show any sign of frequency roll-off, and

are also well in line with published [77] and unpublished [142] findings from other research groups. The signal bandwidth demonstrated in our experiment may hence be further increased by at least a factor of two.

A.7 General considerations for seamless interfacing of wireless THz links and fiber-optic networks

With respect to the integration of current POH devices into fiber-optic networks, the optical losses are still too high, even when considering the second device generation which features a fiber-to-fiber insertion loss of about 26 dB (comprising 6.5 dB of loss per grating coupler, 12 dB loss of the plasmonic waveguides, and 1 dB loss of on-chip waveguides and non-optimum MMI couplers). The loss of the on-chip grating couplers can be reduced to below 2 dB per coupler [143], and further down to 0.7 dB by incorporating reflecting surfaces underneath the grating couplers [144]. Moreover, the intrinsic loss of the 20 µm-long plasmonic phase shifters can be reduced to 4 dB by using silver as a low-loss plasmonic material, see Appendix A.6. Implementing these improvements brings down the total insertion loss to less than 6 dB, comprising 1.4 dB for the grating couplers and 4 dB for the 20 µm-long POH MZM. This compares well with the insertion losses of state-of-the-art silicon depletion-type modulators [141] that are typically used in optical communications, but that are far from providing the required modulation bandwidths in excess of 0.3 THz. Note, however, that even the non-optimum POH MZM used in our current THz transmission experiments would permit transmission of the optical signal over tens or even hundreds of kilometers of optical fiber. This is due to the fact that the optical signal-to-noise ratio (OSNR) is dominated by the ASE noise of the first EDFA after the POH MZM and hence any re-amplification along the fiber link would not deteriorate the OSNR significantly.

In the current proof-of-concept demonstrations, the POH MZM is driven with a THz power of 0 dBm, see Appendix A.3, and the transmission distance of the THz wireless link is 16 m, limited by the width of the building in which the experiment was performed. This span is still smaller than those envisaged for medium-distance links, in which wireless signal should be transmitted over of

100 m…1 km [58]. For a distance $d = 16\,\mathrm{m}$ bridged in our current transmission experiment, the free-space path loss (FSPL) at a carrier frequency of $f_{\mathrm{Tx,THz}} = 0.2885\,\mathrm{THz}$ is $10\log_{10}\left(c/4\pi f_{\mathrm{Tx,THz}} d\right)^2 = 106\,\mathrm{dB}$, and the THz transmitter power amounts to −11 dBm, measured at the output of the UTC-PD. Taking into account the overall gain of 41 dB provided by the THz amplifier cascade as well as the 2.5 dB loss in the THz probe, the overall antenna gain of the transmitter and the receiver antenna-lens combination in our experiment amounts to approximately 79 dBi. For a span of $d = 1\,\mathrm{km}$, the FSPL would increase to about 142 dB. At the same time, we may assume that the POH MZM can be improved to feature a lower $U_\pi L$ product of, e.g., 100 Vμm, which is a factor of 2.4 smaller than the $U_\pi L$ product of 240 Vμm of the current device. Assuming the same modulator length as in the current experiment, the required THz drive power to obtain a similar BER performance as the one shown in Fig 3.3(d) of Chapter 3 would drop to approximately −8 dBm. Using the same UTC-PD and THz amplifiers as in the current experiment, one would require an overall antenna gain of about 106 dBi, which can be realistically realized [58]. Additional improvements may be achieved by using further optimized EO materials, for which $U_\pi L$ products of the order of 35 Vμm can be attained, see Appendix A.6, contributing another 9 dB to the power budget. Moreover, co-packaging of THz amplifiers and POH MZM may help to eliminate the losses of the THz connections and the probe, and use of high-power THz UTC-PD [145], in combination with THz amplifier (e.g., MPA) at the transmitter, can permit higher transmitter powers of, e.g. 4 dBm, which would add at least another 15 dB to the power budget. Note also that, for high data rates, any improvement of the optical losses of the POH MZM contributes to a further increase in the loss margin. Taken together, these measures should allow to increase the transmission distance to 1 km or more, while still maintaining a reasonable loss margin for the wireless THz link.

Another unique feature of POH modulators is their compact footprint, which, when used in conventional transceivers, offers large communication bandwidth on a small chip area. Taking into account silicon photonic MMI couplers along with the POH phase shifter section, a T/O converter would occupy an on-chip area of approximately 40 μm × 10 μm = 400 μm² and features a 3 dB frequency response exceeding 0.36 THz, thus leading to a bandwidth-to-area ratio larger

than 900 THz/mm². Considering the aforementioned improvements with respect to the use of polymers with larger EO coefficients (a seven-fold increase in the $n_{EO}^3 r_{33}$) and assuming that the power splitters can be designed using the plasmonic waveguides [34], the total area of the POH MZM can be brought down to approximately 5 µm × 2 µm = 10 µm², resulting in a bandwidth-to-area ratio as large as 36 PHz/mm². In comparison, the state-of-the-art silicon depletion-type modulators [13] have a bandwidth-to-area ratio of, e.g., 3.2 THz/mm² (3 dB frequency of 48 GHz with a modulator length of 250 µm and assuming a minimum width of 60 µm) which is at least a factor of 280 smaller than what could be achieved with the POH technology. Note that these numbers are merely estimations, which completely disregard the necessary electrical and optical feed lines. The coupling structures for the THz signals such as contact pads or THz antennae would dominate the device footprint and eventually limit integration density. In a general practice, MMIC chips are coupled to the rectangular waveguides terminations of bulk devices, for e.g., high-gain horn antenna, through radial-probe transitions [146]. Following a similar approach for T/O converters requires a considerable chip area of at least 0.4 mm², corresponding to the dimensions of the rectangular waveguide. Alternatively, T/O converters could be integrated with on-chip planar antenna structures [147], [148] which have relaxed space requirements of less than 0.1 mm² but come at a cost of smaller antenna gain and increased cross-talk. However, these coupling structures are still much larger than the footprint of the POH devices.

[End of the Methods and Supplementary Information of paper [J3]]

B Fabrication and characterization of CC-SOH MZM

The contents of this appendix is taken from Supplementary Information of a research article [J1] published in Optica. The structure and layout is adapted to fit this thesis.

S. Ummethala, J. N. Kemal, A. S. Alam, M. Lauermann, A. Kuzmin, Y. Kutuvantavida, S. H. Nandam, L. Hahn, D. L. Elder, L. R. Dalton, T. Zwick, S. Randel, W. Freude, C. Koos, "Hybrid Electro-Optic Modulator Combining Silicon Photonic Slot Waveguides with High-k Radio-Frequency Slotlines" published in *Optica*.

[Start of the Supplementary Information of journal publication [J1]]

B.1 Field simulations of RC-SOH and CC-SOH devices

Exemplary field profiles of RF and optical modes of typical resistively-coupled silicon-organic hybrid (RC-SOH) and capacitively-coupled SOH (CC-SOH) devices that are depicted in Figures 5.1(b) and (d) were carried out using eigenmode solver of CST Microwave Studio. For both devices, we assumed a slot width $w_s = 100\,\text{nm}$, a silicon (Si) rail width $w_{\text{rail}} = 200\,\text{nm}$, a rail height of $h_{\text{rail}} = 220\,\text{nm}$, and a spacing of $w_{\text{sb}} = w_{\text{hk}} = 1\,\mu\text{m}$ between the rails and the metal traces of the ground-signal-ground (GSG) transmission line. To reduce optical losses due to free-carrier absorption (FCA) in the doped Si regions of the RC-SOH device, we assumed a two-level doping profile with a low donor concentration in the rails (n_{D}, light green in Fig. 5.1(a), resistivity $\rho = 5.5\times10^{-4}\,\Omega\,\text{m}$) and a higher concentration (n_{D}^{+}, dark green in Fig. 5.1(a), resistivity $\rho = 1\times10^{-4}\,\Omega\,\text{m}$) in the doped Si slabs, see [32] for details. The slab thickness amounts to $h_{\text{sb}} = 70\,\text{nm}$. In the simulation shown in Fig. 5.1(b), the doped silicon is modeled as a conductive dielectric with the aforementioned

resistivities and a permittivity of $\varepsilon_{r,Si} = 11.7$. For the CC-SOH devices, we assumed a high-k slab with a thickness of $h_{hk} = 350\,\text{nm}$ and a permittivity $\varepsilon_{r,hk} = 100$, see Appendix B.5 for a more detailed discussion of advantageous device designs. The Si rails are assumed to be undoped and therefore modeled as a pure dielectric with zero conductivity and a relative permittivity $\varepsilon_{r,Si} = 11.7$. Note that the silicon rails may also be slightly doped to increase the efficiency of the device, see our discussion of improved designs for CC-SOH MZM in Appendix B.5. For RF modelling of the organic electro-optic (EO) material, we assume a relative permittivity $\varepsilon_{r,EO} = 5.68$.For simulating the optical mode profiles, we used the refractive indices of $n_{Si} = 3.5$ and $n_{SiO_2} = 1.44$ for silicon and silicon dioxide at a vacuum wavelength of 1.55 µm. The high-k dielectric is modelled with a refractive index $n_{hk} = 1.85$, which was the value that we obtained from spectroscopic ellipsometry measurements of the amorphous $BaTiO_3$ (BTO) films used in the experiments, see Appendix B.2.3 and Fig. B.1 below. For the organic EO material, we assumed a refractive index of $n_{EO} = 1.9$ at a wavelength of 1.55 µm as specified in [54].

B.2 Device fabrication

B.2.1 Fabrication of CC-SOH MZM waveguide structures

The CC-SOH MZM used in our experiments are fabricated on standard silicon-on-insulator (SOI) substrates, featuring 220 nm-thick silicon (Si) device layers and 2 µm-thick buried oxide (SiO_2) layers. The devices are fabricated in a five-step lithographic process using high-resolution electron-beam (e-beam) lithography (Raith EBPG-5200). In the first lithography step, gold markers are fabricated on the SOI chip to ensure alignment accuracy of better than 50 nm between different exposures. In two subsequent lithographic steps, we fabricate shallow-etched grating couplers and fully-etched Si strip and slot waveguides along with the corresponding strip-to-slot converters. In the fourth lithographic step, ground-signal-ground (GSG) transmission lines made of 150-nm-thick gold are fabricated via a lift-off process using a poly-methyl methacrylate (PMMA) and an electron-beam-evaporated gold layer. In the last step, the high-k dielectric $BaTiO_3$ (BTO) is deposited and structured via a second lift-off process using again PMMA as a mask. For the current device generation, 1 µm-

wide amorphous BTO films with a thickness of 150 nm are deposited by room-temperature RF magnetron sputtering using a stoichiometric $BaTiO_3$ disk with 2-inch diameter as a target. The deposition is carried out at a base pressure of 5×10^{-8} mbar, and the working pressure is set to 2.5×10^{-3} mbar by controlling the flow rate (30 sccm) of Ar gas. A rather low RF power of 30 W is applied to the target to keep the temperature of SOI substrates below the glass transition temperature of the PMMA mask to enable a proper lift-off. Due to the low process temperature, the BTO thin film is known to be amorphous [125], [149], which may be overcome by subsequent annealing [128]. The width of the BTO film is chosen to be 1 µm for good trade-off between the optical losses due to the gold transmission line and the capacitance of the BTO film, see Appendix B.5 for details. Note that, in the current CC-SOH devices, the thickness of the BTO films and the metal electrodes is limited to 150 nm due to limitations of the lift-off process using a single PMMA resist layer. With process optimization and by employing bi-layer resists [104], [105], it would be possible to fabricate optimized CC-SOH devices with thicker BTO and metal layers and thus further increased modulation efficiency, see Appendix B.5 for details.

B.2.2 Optical losses of CC-SOH MZM

For our current CC-SOH devices structures, we measure an insertion loss of about 5 dB per grating coupler, a propagation loss of 6 dB/mm in the CC-SOH phase shifter, and an additional 3 dB of loss from other passive on-chip structures such as transport waveguides, strip-to-slot converters, and MMI couplers. This results in a total fiber-to-fiber insertion loss of about 19 dB for a 1 mm-long CC-SOH MZM. Note that these losses can be greatly reduced by optimized designs and fabrication processes. Specifically, systematic optimization of strip-to-slot converters and MMI couplers may allow to reduce the losses of each of these building blocks to 0.02 dB and 0.2 dB, respectively [47],[108], leading to an overall loss contribution of less than 0.5 dB. We also investigated the origin of the rather high propagation losses in the CC-SOH phase shifter. To this end, we measured the attenuation of 500 nm-wide strip waveguides of different lengths that were fabricated in the same process run as the CC-SOH devices, but that were not covered with BTO. For these structures, we also obtained rather high propagation losses of approximately 1 dB/mm, which is much

larger than the value of 0.045 dB/mm that can be achieved when fabricating similar strip waveguides using highly optimized foundry processes[107]. We attribute the high loss of our structures to large sidewall roughness caused by a non-optimum fabrication process. The even higher propagation losses of 6 dB/mm measured for the slot-waveguide phase shifters are attributed to the fact that slot waveguides are more prone to roughness-induced scattering losses than strip waveguides. Specifically, ref [5] reports about slot-waveguides with 100 nm slot width and propagation losses of 0.2 dB/mm, which is approximately 3.5 to 6 times higher than the propagation loss of (0.045 ± 0.012) dB/mm measured for 500 nm-wide strip waveguides that were fabricated in the same process. For our structures, the 6 dB/mm measured for slot waveguides with 100 nm slot width and the 1 dB/mm propagation loss for 500 nm-wide strip waveguides leads also to a ratio of 6. This ratio is in good agreement with the findings in [5] given the fact that the rail width of the slot waveguides presented there amounts to 260 nm, whereas the rails in our structures are only 200 nm, thereby leading to slightly increased propagation losses of the slot waveguides. We further expect that absorption losses in the BTO slabs, which are in direct contact with the silicon rails, can be neglected – sputtered BTO has negligible optical losses in the visible and near infrared spectral range[109]–[113], which is also confirmed by ellipsometric measurement of the deposited films, see Fig. B.1 and Appendix B.2.3 below. We also checked the potential impact of absorption losses in the gold pads of the GSG transmission line by using electromagnetic simulations (CST Microwave Studio), based on which we estimate a contribution less than 0.1 dB/mm, assuming a width of the BTO slabs of $w_{\mathrm{hk}} = 1\,\mu\mathrm{m}$, see Fig. B.8 and the associated discussion in Appendix B.5 for details. In combination with roughness-induced slot-waveguide propagation losses of 0.2 dB/mm[107], the overall propagation loss in the CC-SOH phase shifter might hence be brought down to approximately 0.3 dB/mm. Assuming a 1 mm-long CC-SOH phase shifter and taking into account an additional 0.5 dB of loss from the strip-to-slot converters and MMI couplers[47][108], on-chip insertion losses of the order of 1 dB might eventually come into reach. These losses can well compete with low-loss RC-SOH devices of much lower bandwidth [29]. In addition, the fiber-chip and chip-chip coupling losses can be greatly reduced by using 3D-printed micro-lenses[114] or photonic wire bonds[115], [116].

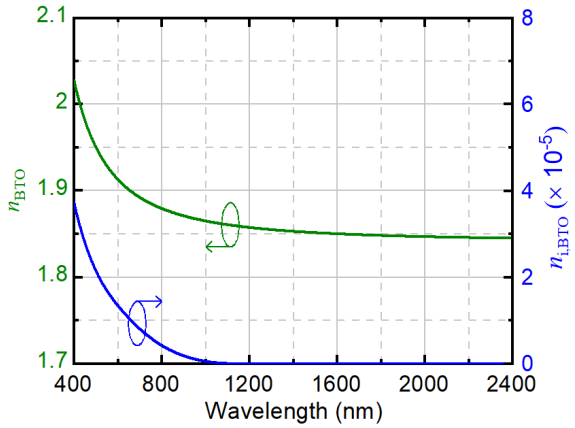

Figure B.1: Refractive index n_{BTO} and extinction coefficient $n_{\mathrm{i,BTO}}$ of 750 nm-thick amorphous BTO film measured using spectroscopic ellipsometry. Note that the results for the extinction coefficient $n_{\mathrm{i,BTO}}$ are not very accurate and should rather be understood as an order-of magnitude estimate due to limited sensitivity of the measurement technique with respect to optical loss.

B.2.3 Optical properties of the BTO film

The optical properties of BTO thin films are determined from 750 nm-thick BTO layers deposited on SiO_2/Si substrates using the same process parameters that are used for fabricating the CC-SOH modulators as described in the previous section. By carrying out spectroscopic ellipsometric measurements, we determine a real part of the refractive index $n_{\mathrm{BTO}} = 1.85$ along with a negligible imaginary part (extinction coefficient) $n_{i,\mathrm{BTO}}$ at 1550 nm, see Fig. B.1. It should be noted that the results for the extinction coefficient $n_{\mathrm{i,BTO}}$ are likely not very accurate and should rather be understood as an order-of magnitude estimate due to limited sensitivity of the ellipsometric measurement technique with respect to optical loss. For evaluating the raw data, the wavelength dependence of n_{BTO} and $n_{\mathrm{i,BTO}}$ is modeled by a simple Cauchy-type dispersion model [150]. The refractive index extracted from our measurements shows a good agreement with previously published values for amorphous $BaTiO_3$ layers deposited by room-temperature sputtering[109], [113], [151]. The slight differences in the indices are attributed to variations of the process parameters such as gas pressure in the deposition chamber, which results in composition variations of the deposited material.

B.2.4 Permittivity of the BTO film at RF frequencies

As mentioned in Section 5.2, the RF properties of BTO are crucial for the performance of CC-SOH modulators. Since the material properties of BTO vary substantially depending on the deposition technique and its parameters[152], we perform a dedicated experiment to extract the RF properties of our BTO films. To this end, we fabricate two sets of coplanar waveguides (CPW) with lengths *L* of 1 mm, 2 mm, and 3 mm and a gap width of $w = 1\,\mu\mathrm{m}$ between the ground and the signal traces, see Fig. B:2 for a more detailed description of the underlying cross-sectional geometries. The first set of CPW only consists of the metal transmission-line strips without any BTO, Fig. B.2(b), whereas the second set contains a BTO thin film filling the gaps between the CPW strips, Fig. B.2(c). For better comparability to the CC-SOH modulators described in Chapter 5, we used the same SOI wafers for these test structures and removed the silicon device layer prior to depositing the metal transmission lines and the BTO films. We measure the two-port *S*-parameters for all variations of the CPW using a vector network analyzer (VNA, Keysight PNA-X N5247) in the frequency range from 0.01 GHz to 110 GHz. In this measurement, we use the line–reflect–reflect–match [153] calibration technique to perform an on-wafer calibration of the VNA and the associated cables and probes. To remove the impact of the on-chip RF fixtures (RF pads and tapered transitions), we de-embed the measured S-parameters using the so-called 'L-2L de-embedding' technique described in Section 4.6 of [154], which allows us to extract the *S*-parameters of the uniform transmission line sections with lengths *L* of 1 mm, 2 mm, and 3 mm. From these measurements, we derive the respective complex propagation constant $\underline{\gamma}_{\mathrm{BTO}}$ and $\underline{\gamma}_{\mathrm{air}}$ of the BTO-filled and air-filled CPW, respectively. Once the frequency-dependent complex propagation constant $\underline{\gamma}_{\mathrm{BTO,m}} = \alpha_{\mathrm{BTO,m}} + \mathrm{j}\beta_{\mathrm{BTO,m}}$ is known, the associated effective permittivity $\varepsilon_{\mathrm{eff,meas}}$ of the mode is can be obtained by

$$\varepsilon_{\mathrm{eff,meas}}(f) = \left(\frac{\beta_{\mathrm{BTO,m}}}{2\pi f / c_0} \right)^2 . \tag{B.1}$$

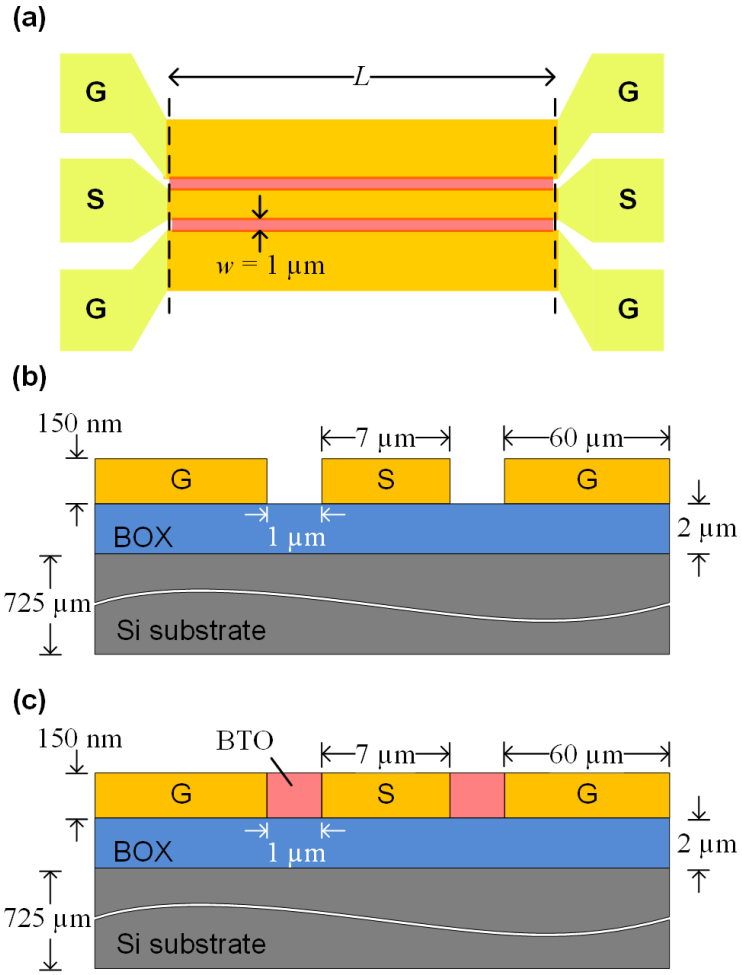

Figure B.2: CPW structures used for extracting the relative permittivity and the loss tangent of amorphous BTO films. **(a)** Top-view schematic of the CPW test transmission line with length L and electrode spacing $w = 1\,\mu\text{m}$. **(b)** Cross-section of air-filled CPW test structure showing the geometric dimensions. **(c)** Cross-section of BTO-filled CPW showing the geometric parameters.

In this relation, c_0 denotes the vacuum speed of light. The extracted $\varepsilon_{\text{eff,meas}}$ obtained from transmission lines of different lengths L is shown in Fig. B.3. Note that the sharp increase of the measured effective permittivity $\varepsilon_{\text{eff,meas}}$ towards low frequencies is a result of the non-zero resistivity of the metal CPW traces, resulting in the so-called slow-wave effect [155]. The slow-wave effect is a consequence of the fact that, at low frequencies, the penetration depth of the RF fields ("skin depth") approaches or even exceeds the thickness of the metal transmission-line traces. In this case, magnetic fields can exist also within the metal conductor, which leads to an additional internal inductance that strongly

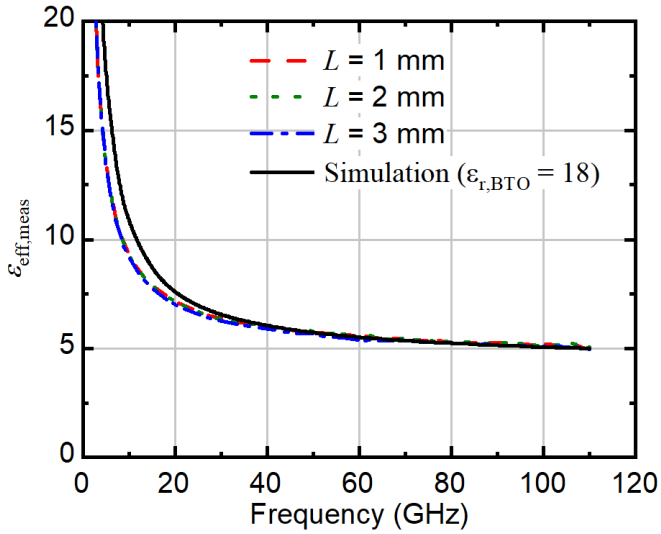

Figure B.3: Measured and simulated effective permittivity of the BTO-filled CPW for different lengths *L*. The sharp rise in the effective permittivity of the CPW originates from resistive metal CPW traces and from the so-called slow-wave effect and does not represent a dispersive behaviour of the underlying dielectric materials. The black curve shows the effective permittivity of the of the CPW simulated using an electromagnetic solver and assuming a frequency-independent relative permittivity $\varepsilon_{\mathrm{r,BTO}} = 18$ for the BTO film.

increases the effective permittivity of the RF mode [155], [156]. To properly account for resistive metal traces and for the slow-wave effect, we use a commercial electromagnetic solver (CST Microwave Studio) to simulate the dispersion of the RF field to determine the effective permittivity of the BTO-filled CPW. In this simulation, we modelled the gold transmission lines by a material with frequency-dependent complex surface impedance that is calculated using the Hammerstad-Jensen model ("tabulated surface impedance" in CST Microwave studio)[157]. The geometrical cross-section of the simulated BTO-filled transmission line corresponds to the one shown in Fig. B.2(c). For the gold we assume a conductivity of 2.5×10^{7} S/m., which was extracted from the measured RF losses using the same numerical model, see Appendix B.2.5 below.

For the BTO, we assume a frequency-independent relative permittivity $\varepsilon_{\mathrm{r,BTO}}$, which we vary as to find best agreement between the simulated frequency-dependent effective permittivity $\varepsilon_{\mathrm{eff}}(f)$ of the RF mode and its measured counterpart $\varepsilon_{\mathrm{eff,meas}}$. We find good agreement for $\varepsilon_{\mathrm{r,BTO}} = 18$, which leads to the solid black curve in Fig. B.3. Note that the agreement of the measured and the simulated behaviour of $\varepsilon_{\mathrm{eff}}$ is particularly good at high frequencies, which is

the most relevant part for our devices. For low frequencies, the measured effective permittivity $\varepsilon_{\mathrm{eff,meas}}$ is slightly smaller than its simulated counterpart. We attribute these differences to small deviations between the simulated and the fabricated cross-section of the CPW, which become more relevant at low frequencies where RF currents flow in the entire cross-section of the metal traces. Note also that our finding of a frequency-independent relative permittivity of $\varepsilon_{\mathrm{r,BTO}} = 18$ is in good agreement with literature [125]–[128], where permittivities $\varepsilon_{\mathrm{r,BTO}}$ between 14 and 20 were found in the frequency range between 1 kHz and 40 GHz. Regarding future CC-SOH devices, the modulation efficiency can be greatly improved by using polycrystalline BTO films, for which with relative permittivities in excess of 100 [126], [128] have been measured over a few GHz [158].

B.2.5 Dielectric RF loss of the BTO film

To estimate the loss tangent of the BTO film, we compare the microwave propagation loss measured from the S-parameters of the BTO-filled CPW with that extracted from an electromagnetic simulation. Since the contribution of ohmic losses is unknown, we first extract the frequency-dependent propagation loss of the air-filled CPW loss from the associated electrical S-parameter measurements, see Appendix B.2.4 above, and compare them with the results of numerical simulations (CST Microwave Studio) for various conductivities. We find very good agreement when assuming a conductivity of $\sigma_{\mathrm{Au}} = 2.5 \times 10^7\,\mathrm{S/m}$ for the 150-nm-thick gold strips, see the blue solid and dashed curves in Fig. B.4. In these simulations, we assumed a conductivity of $\sigma_{\mathrm{Si}} = 0.13\,\mathrm{S/m}$ for the bulk Si substrate, as specified by the wafer manufacturer. Note that the conductivity value for deposited gold thin films is smaller than the conductivity of $4.5 \times 10^7\,\mathrm{S/m}$ for bulk gold – a common phenomenon observed in thin gold layers, for which the properties also seem to depend on the process conditions [159]. Using the same conductivity values for gold and the Si substrate, we simulate BTO-filled CPW using a relative permittivity $\varepsilon_{\mathrm{r,BTO}} = 18$ and different values for loss tangent for the 150 nm-thick BTO film. The CPW losses obtained from the simulations are compared with those extracted from the measured electrical S-parameters of the BTO-filled CPW. Interestingly, the simulations already predict an increase of the RF losses of the BTO-filled CPW with

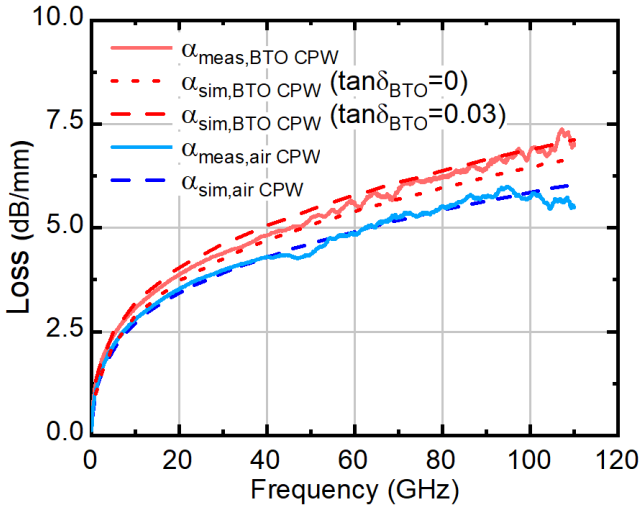

Figure B.4: Measured (solid lines) and simulated (dashed lines) microwave propagation loss $\alpha_{\text{air CPW}}\left(\alpha_{\text{BTO CPW}}\right)$ of the air-filled (BTO-filled) CPW. The measured and simulated loss assuming a loss tangent $\tan\delta_{\text{BTO}} = 0$ and $\tan\delta_{\text{BTO}} = 0.03$ for the 150-nm-thick amorphous BTO film. We determine an upper limit for the BTO loss tangent to be 0.03.

respect to its air-filled counterpart, even when the BTO is assumed to be lossless ($\tan\delta_{\text{BTO}} = 0$), see dotted red curve in Fig. B.4. We attribute this finding to the fact that the BTO filling of the CPW leads to an increase of the RF current density in the metal traces that are directly adjacent to the BTO slabs, which increases the ohmic losses. Note that this increase might already be sufficient to explain the measured losses of the BTO-filled CPW within the measurement accuracy. If we additionally vary the loss tangent $\tan\delta_{\text{BTO}}$, the propagation losses increase further – we have included the simulated propagation loss for a loss tangent of $\tan\delta_{\text{BTO}} = 0.03$, see dashed red line in Fig. B.4, which represents an upper boundary for the measured losses. We hence consider this loss tangent a conservative estimate for the dielectric losses of the amorphous BTO films used in the current devices. The extracted material loss parameter $\tan\delta_{\text{BTO}} = 0.03$ is in fair agreement with previously published values of similar amorphous BTO films [125].

B.2.6 Residual conductivity of the BTO slabs

The BTO layers used in our devices are amorphous and may exhibit a residual conductivity that might impair the dynamics of the CC-SOH devices by long

RC time constants. To investigate this effect, we applied a DC voltage between the signal and the ground pads of our structures and tried to measure the associated DC current. We did this both with the CC-SOH modulator structure, for which the signal trace of the transmission line is separated from each ground trace by a pair of BTO slabs with a gap in between, see Fig. 5.1(c), and with the CPW test structures according to Fig. B.2, which either have no BTO at all or a continuous BTO slab between the metal traces. In all these experiments, the measured DC current was of the order of 10 nA, even for an applied DC voltage of 40 V, with no clear dependence on the device structure or on the on the presence of the BTO slabs. We may hence extract a lower limit of the order of few GΩ for the resistance of the BTO slabs – but it is presumably much higher since the BTO is very likely not the main source of the DC currents, which were also measured for the structure without the BTO. Still, these findings may confirm our notion that a residual conductivity of the BTO can be safely neglected for our devices. This is in line with the finding that we did not observe any slow dynamics in the electro-optic response of the CC-SOH MZM that could be related to the impact of non-zero resistivity of the BTO. Specifically, accounting for the frequency-dependent roll-off according to Fig. 5.2(d), the "low-frequency" U_π of 1.3 V measured with a 300 Hz triangular drive signal, Fig. 5.2(c), is still effective for the high-speed transmission experiments, where the eye diagrams shown in Fig. 5.3(b) were generated with a peak-to-peak drive signal of 1 V.

B.3 Field interaction factor, electro-optic coefficient, and bandwidth of CC-SOH MZM

B.3.1 Field interaction factor and $U_\pi L$ product

CC-SOH devices combine a silicon photonic slot waveguide for optical frequencies[46] with a high-k dielectric slotline for RF frequencies [57]. This leads to strong EO interaction of the RF and the optical fields, which we can be quantified by a field interaction factor Γ_s , obtained from an overlap integral of the optical and the RF field. The following section provides a derivation of these equations.

In general, the presence of the electric RF field will lead to an anisotropic change $\Delta\boldsymbol{\varepsilon}_{\mathrm{r,o}}$ of the relative permittivity tensor that is seen by the optical field. The optical fields can be represented by the vectorial electric and magnetic eigenmode fields $\underline{\mathcal{E}}_{\mathrm{o}}(x,y)$ and $\underline{\mathcal{H}}_{\mathrm{o}}(x,y)$ by a slowly varying complex envelope $\underline{A}_{\mathrm{o}}(z,t)$ [160],

$$\begin{aligned}\underline{\mathrm{E}}(x,y,z) &= \underline{A}_{\mathrm{o}}(z,t)\frac{\underline{\mathcal{E}}_{\mathrm{o}}(x,y)}{\sqrt{\mathcal{P}_{\mathrm{o}}}}\,\mathrm{e}^{\mathrm{j}(\omega_{\mathrm{c}}\,\mathrm{t}-\beta_{\mathrm{c}}z)},\\ \underline{\mathrm{H}}(x,y,z) &= \underline{A}_{\mathrm{o}}(z,t)\frac{\underline{\mathcal{H}}_{\mathrm{o}}(x,y)}{\sqrt{\mathcal{P}_{\mathrm{o}}}}\,\mathrm{e}^{\mathrm{j}(\omega_{\mathrm{c}}\,\mathrm{t}-\beta_{\mathrm{c}}z)}.\end{aligned} \tag{B.2}$$

In this relation, ω_{c} is the optical carrier frequency and β_{c} the associated wave-number of the optical mode. $\underline{A}_{\mathrm{o}}(z,t)$ represents a complex power amplitude with unit $\sqrt{\mathrm{W}}$, and $\mathcal{P}_{\mathrm{o}}$ denotes the power that is associated with the vectorial optical mode fields $\underline{\mathcal{E}}_{\mathrm{o}}(x,y)$ and $\underline{\mathcal{H}}_{\mathrm{o}}(x,y)$,

$$\mathcal{P}_{\mathrm{o}} = \frac{1}{2}\iint \mathrm{Re}\left\{\underline{\mathcal{E}}_{\mathrm{o}}(x,y)\times\underline{\mathcal{H}}_{\mathrm{o}}^{*}(x,y)\right\}\cdot\mathbf{e}_{\mathrm{z}}\,\mathrm{d}x\,\mathrm{d}y. \tag{B.3}$$

Similarly, the electric and magnetic RF fields can be represented by

$$\begin{aligned}\underline{\mathbf{E}}_{\mathrm{RF}}(x,y,z) &= \underline{A}_{\mathrm{RF}}\frac{\underline{\mathcal{E}}_{\mathrm{RF}}(x,y)}{\sqrt{\mathcal{P}_{\mathrm{RF}}}}\,\mathrm{e}^{\mathrm{j}(\Omega\mathrm{t}-Bz)},\\ \underline{\mathbf{H}}_{\mathrm{RF}}(x,y,z) &= \underline{A}_{\mathrm{RF}}\frac{\underline{\mathcal{H}}_{\mathrm{RF}}(x,y)}{\sqrt{\mathcal{P}_{\mathrm{RF}}}}\,\mathrm{e}^{\mathrm{j}(\Omega\mathrm{t}-Bz),}\end{aligned} \tag{B.4}$$

where Ω is the RF frequency of the applied signal and B the associated wave-number of the RF mode with vectorial electric and magnetic mode fields $\underline{\mathcal{E}}_{\mathrm{RF}}(x,y)$ and $\underline{\mathcal{H}}_{\mathrm{RF}}(x,y)$. $\underline{A}_{\mathrm{RF}}$ represents the complex power amplitude of the RF wave with unit $\sqrt{\mathrm{W}}$ and $\mathcal{P}_{\mathrm{RF}}$ denotes the power that is associated with the RF mode fields,

$$\mathcal{P}_{\mathrm{RF}} = \frac{1}{2}\iint \mathrm{Re}\left\{\underline{\mathcal{E}}_{\mathrm{RF}}(x,y)\times\underline{\mathcal{H}}_{\mathrm{RF}}^{*}(x,y)\right\}\cdot\mathbf{e}_{\mathrm{z}}\,\mathrm{d}x\,\mathrm{d}y. \tag{B.5}$$

According to Eq. (1.57) and Eq. (1.58) in [160], the modulation of the optical wave can be described by a change of the associated complex amplitude according to

$$\frac{\partial \underline{A}_{\mathrm{o}}(z,t)}{\partial z} = -\mathrm{j}\frac{\omega}{4\mathcal{P}_{\mathrm{o}}} \iint \left[\Delta\boldsymbol{\varepsilon}(x,y,z)\underline{\mathcal{E}}_{\mathrm{o}}(x,y)\right]\cdot\underline{\mathcal{E}}_{\mathrm{o}}^{*}(x,y)\,\mathrm{d}x\,\mathrm{d}y\;\; \underline{A}_{\mathrm{o}}(z,t), \tag{B.6}$$

where $\Delta\boldsymbol{\varepsilon}(x,y,z) = \varepsilon_0 \Delta\boldsymbol{\varepsilon}_{\mathrm{r,o}}(x,y,z)$ denotes the anisotropic perturbation of the relative-permittivity profile for the optical field, that arises as a consequence of the electrical RF field. Note that this relation is formulated with respect to a retarded time frame, see Eq. (1.54) in [160]. To quantify the perturbation of the relative permittivity, we express it through the associated change $\Delta\boldsymbol{\eta}$ of the impermeability tensor $\boldsymbol{\eta} = \boldsymbol{\varepsilon}_{\mathrm{r,o}}{}^{-1}$ which, for small perturbations, is related to $\Delta\boldsymbol{\varepsilon}_{\mathrm{r,o}}$ by

$$\Delta\boldsymbol{\varepsilon}_{\mathrm{r,o}} = -\,\boldsymbol{\varepsilon}_{\mathrm{r,o}}\Delta\boldsymbol{\eta}\,\boldsymbol{\varepsilon}_{\mathrm{r,o}} \tag{B.7}$$

Within the organic electro-optic material, the change $\Delta\boldsymbol{\eta}$ of the impermeability tensor is related to the electric field of the RF wave via the electro-optic tensor r_{lm} according to Eq. (11.2.13a) in [37]. Note that, for organic EO materials, the electro-optic tensor r_{lm} is defined with respect to a local coordinate system, for which the axis $l = 3$ is given by the local poling direction of the EO material. This poling direction is induced by a static electric field that is applied to the transmission-line electrodes at an elevated temperature. For simplicity, we assume that the RF electric field is predominantly transverse, i.e., $\underline{E}_{\mathrm{RF},z} \approx 0$, that the transverse components $\underline{E}_{\mathrm{RF},x}$ and $\underline{E}_{\mathrm{RF},y}$ are in phase and can thus be represented as real numbers, and that the static poling field can be approximated by the real-valued vector field $\underline{E}_{\mathrm{RF}}(x,y)$. We further assume that only the dominant r_{33} coefficient of the organic EO material plays a role and that all other coefficients r_{lm} with $l,m \neq 3$ can be neglected. Accounting for the local transformation between the coordinate system of the EO tensor and the (x,y,z)-system of the device, approximating the EO material in absence of an electric field by an isotropic medium with refractive index n_{EO}, and neglecting any walk-off between the optical and the RF field, Eq. (B.16) can be rewritten as

$$\frac{\partial \underline{A}_{\mathrm{o}}(z,t)}{\partial z} = -\mathrm{j}\,\Delta\beta_{\mathrm{c}}\underline{A}_{\mathrm{o}}(z,t),$$
$$\Delta\beta_{\mathrm{c}} = \frac{\omega\varepsilon_0 n_{\mathrm{EO}}^4 r_{33}\underline{A}_{\mathrm{RF}}}{4\mathcal{P}_{\mathrm{o}}\sqrt{\mathcal{P}_{\mathrm{RF}}}} \times \iint\limits_{A_{\mathrm{EO}}} \left|\underline{\mathcal{E}}_{\mathrm{o}}(x,y)\right|^2 \underline{\mathcal{E}}_{\mathrm{RF}}(x,y)\cos^2\vartheta(x,y)\,\mathrm{d}x\,\mathrm{d}y \tag{B.8}$$

In these relations, $\Delta\beta_{\mathrm{c}}$ denotes the (complex) amplitude change of the modal propagation constant due to the modulating RF field of (complex) power amplitude $\underline{A}_{\mathrm{RF}}$, and $\vartheta(x,y)$ is the local angle between the optical and the RF electric field vectors. A_{EO} denotes the cross-sectional area that is filled by the organic EO material. Without loss of generality, we may assume that $\underline{A}_{\mathrm{RF}}, \Delta\beta_{\mathrm{c}} \in \mathbb{R}$, which allows us to rewrite Eq. (B.7) in terms of the associated RF voltage amplitude $U_{\mathrm{RF}} = \underline{A}_{\mathrm{RF}}\sqrt{Z_{\mathrm{RF}}}$, where Z_{RF} is the line impedance of the RF transmission line. For better comparability to conventional RC modulators, we express the phase shift $\Delta\phi$ introduced along an EO section of length L by the electric field $U_{\mathrm{RF}}/w_{\mathrm{s}}$ that would be generated by the RF voltage U_{RF} within a slot of width $w_{\mathrm{s},}$,

$$\Delta\phi = \frac{1}{2} n_{\mathrm{EO}}^3 r_{33} \frac{U_{\mathrm{RF}}}{w_{\mathrm{s}}} k_0 L\,\Gamma_{\mathrm{s}} \tag{B.9}$$

where k_0 is the vacuum wavenumber of the optical field, and where the field interaction factor Γ_{s} is given by,

$$\Gamma_{\mathrm{s}} = \frac{n_{\mathrm{EO}} w_{\mathrm{s}}}{2Z_0\mathcal{P}_{\mathrm{o}}\sqrt{\mathcal{P}_{\mathrm{RF}} Z_{\mathrm{RF}}}} \iint\limits_{A_{\mathrm{EO}}} \left|\underline{\mathcal{E}}_0(x,y)\right|^2 \underline{\mathcal{E}}_{\mathrm{RF}}(x,y)\cos^2\vartheta(x,y)\,\mathrm{d}x\,\mathrm{d}y. \tag{B.10}$$

In this relation, $Z_0 = 377\,\Omega$ is the free-space wave impedance. Not that, for a push-pull MZM, the phase difference of the optical signals at the end of the two MZM arms is twice the phase shift $\Delta\phi$ calculated in Eq. (B.9). The $U_\pi L$-product of a push-pull MZM is hence related to the EO coefficient r_{33} of the organic material by

$$U_\pi L = \frac{w_{\mathrm{s}}\lambda}{2n_{\mathrm{EO}}^3 r_{33}\Gamma_{\mathrm{s}}}, \tag{B.11}$$

where λ denotes the vacuum wavelength of the optical field. Note that these relations are general and can be widely applied to any EO modulator structure.

In our CC-SOH devices, the high-permittivity BTO slabs lead to a local enhancement of the electrical RF field $\underline{\mathcal{E}}_{\mathrm{RF}}(x,y)$ within the EO material in the slot, which increases the associated field interaction factor Γ_{s}. Appendix B.5 provides a more detailed discussion on how the field interaction factor Γ_{s} of CC-SOH structures can be increased by appropriate device design.

B.3.2 Electro-optic coefficient and poling efficiency of the fabricated CC-SOH Mach-Zehnder modulator

To estimate the EO coefficient r_{33} of our CC-SOH structures from the measured $U_{\pi}L$ product, we need to evaluate Eqs. (B.10) and (B.11). In a first step, we use an electromagnetic mode solver (CST Microwave Studio) and calculate the field profiles of the optical and RF eigenmodes of the CC-SOH modulator along with the associated RF line impedance $Z_{\mathrm{RF.}}$ The basic cross section of the structure is illustrated in Fig. 5.1(c). In these calculations, we use a silicon rail width $w_{\mathrm{rail}} = 200$ nm, a rail height $h_{\mathrm{rail}} = 220\,\mathrm{nm}$, a slot width $w_{\mathrm{s}} = 100\,\mathrm{nm}$ along with a BTO slab of height $h_{\mathrm{hk}} = 150\,\mathrm{nm}$ and width $w_{\mathrm{hk}} = 1\,\mu\mathrm{m}$, see Fig. 5.1(c). We further assume a vacuum wavelength of $\lambda = 1550\,\mathrm{nm}$ for the optical signal along with refractive indices of $n_{\mathrm{Si}} = 3.5, n_{\mathrm{SiO_2}} = 1.44, n_{\mathrm{BTO}} = 1.85$ and $n_{\mathrm{EO}} = 1.9$ for the silicon, the silicon dioxide, the BTO, and the organic EO material YLD124, respectively. For the calculating the RF field, we assume a GSG transmission line with a metal height $h_{\mathrm{m}} = 150\,\mathrm{nm}$. The width of the signal trace and of each ground trace amounts to 7 µm and 60 µm, respectively, and the conductivity of the gold is set to 2.5×10^{7} S/m, see Appendix B.2.5 above. For the silicon, the silicon dioxide (BOX), the EO material, and the BTO, we assume permittivities of $\varepsilon_{\mathrm{r,Si}} = 11.7, \varepsilon_{\mathrm{r,SiO_2}} = 3.9, \varepsilon_{\mathrm{r,EO}} = 5.68,$ and $\varepsilon_{\mathrm{r,BTO}} = 18,$ respectively. For the simulation of the RF field, the transmission-line traces are modelled as a lossy metal, in which the electromagnetic behaviour of the metal is approximated by assuming a skin depth that is much smaller than the metal thickness. In contrast to the Hammerstad-Jensen model [157] ("tabulated surface impedance" in CST Microwave studio), that was needed for quantitatively correct modelling of the effective permittivity $\varepsilon_{\mathrm{eff}}$ and the RF losses, see Appendix B.2.4 and B.2.5 above, the lossy-metal model allows to account for the true 3D geometry of the metal, which is important for obtaining the correct distribution of the associated RF mode fields. Evaluation of Eq. (B.10) with the

calculated mode fields leads to a field interaction factor of $\Gamma_s = 0.048$ for our current device generation. Using the measured $U_\pi L$ product of 1.3 Vmm, see Fig. 5.2(c), we then evaluate Eq. (B.11) to obtain an EO coefficient of $r_{33} \approx 180$ pm/V for the organic EO material YLD124. Furthermore, we estimated the strength of the poling field that can be expected in the slot when applying a DC voltage of 600 V between the two floating ground traces of the GSG transmission line, leading to a poling voltage of $U_p = 300$ V between the signal and each of the floating ground traces. For simplicity, we assumed that the transverse distribution of the associated static electric field can be approximated by the electric field of the RF mode at low frequencies, leading to a field strength of approximately 450 V/µm within the slot for an externally applied poling voltage of $U_p = 300$ V. For a slot with width $w_s = 100$ nm, 45 V would hence drop across the slot, which corresponds to 15 % of the overall applied poling voltage U_p. This number illustrates clearly that the current structures leave vast room for further improving the interaction of the RF field with the EO material in the slot, e.g., by using polycrystalline BTO films with higher permittivities $\varepsilon_{r,BTO}$ [126], [128] in excess of 100. As explained in Appendix B.5, improved CC-SOH structures can provide field interaction factors Γ_s in excess of 0.3, which is more than six times higher than the currently achieved value of 0.048. Still, the BTO slabs of the current devices already contribute significantly to enhancing the electro-optic interaction – removing the BTO slabs would decrease the field interaction factor by approximately a factor of two to values below 0.025.

B.3.3 Bandwidth of the CC-SOH Mach-Zehnder modulator

The frequency response of the CC-SOH MZM is measured in the frequency range from 0.01 GHz to 110 GHz using a vector network analyzer (VNA, Keysight PNA-X N5247). A calibration kit for 1 mm-connectors is used to shift the measurement reference plane from the network analyzer ports to the end of the connected coaxial cables using a short-open-load-through (SOLT) calibration procedure. The RF signal from the VNA is coupled to the ground-signal-ground (GSG) pads of the CC-SOH MZM using a GSG probe (Cascade Infinity Probe I110-A-GSG-100). The other end of the MZM transmission line is terminated by a second probe connected to a 50 Ω impedance. Spurious reflections

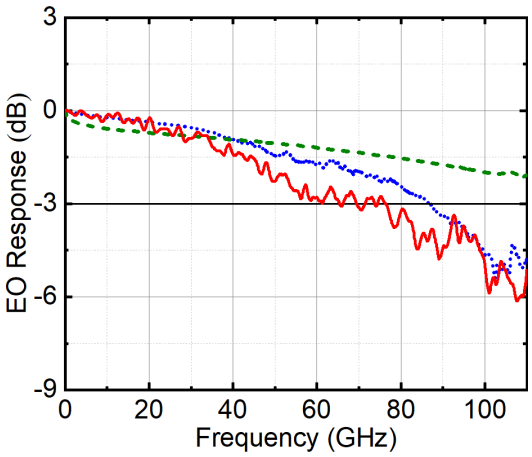

Figure B.5: EO response of a CC-SOH MZM having a phase shifter length L = 1 mm. The red (solid) curve shows the directly measured EO response $S_{21,\mathrm{EO,meas}}$, while the blue (dotted) curve represents the EO response $S_{21,\mathrm{EO,der}}$ derived from the electrical S-parameters. The directly measured and the derived characteristics are in good agreement. The measured device is based on metal transmission lines that are only 150 nm thick. The green (dashed) line represents the possible EO response of the CC-SOH MZM that can be achieved with an improved device having 600 nm-thick metal transmission lines that features smaller RF losses, see Appendix B.5 for details.

at the coplanar transmission line of the CC-SOH MZM are avoided by a tapered transition that provides an impedance matching between the contact pads and the phase shifter section. We exploit the unbalanced arm lengths of the MZM to adjust the device to the quadrature operating point by tuning the wavelength of the feed laser. The intensity-modulated output of the CC-SOH MZM is detected by a calibrated high-speed photodiode (HHI, C05-W36), and the output signal is recorded by the second port of the VNA. The photodiode has a 3 dB bandwidth of 78 GHz, followed by a smooth roll-off, which allows to perform measurements up 110 GHz, where the transfer function drops by 9 dB with respect to the low-frequency range. The EO response $S_{21,\mathrm{EO,meas}}$ of the CC-SOH MZM can be de-embedded from the measured overall transmission $S_{21,\mathrm{overall}}$ by taking into account the frequency response of the photodiode and of the RF probes, leading to the red curve in Fig. B.5, which is equivalent to Fig. 5.2(d). For a 1 mm-long CC-SOH MZM, we measure a 3 dB EO bandwidth of 76 GHz.

To confirm the directly measured EO dynamics, we also estimate the EO transfer function from the electrical scattering parameters. To this end, we measure the electrical S-parameters by connecting the second port of the VNA to the RF

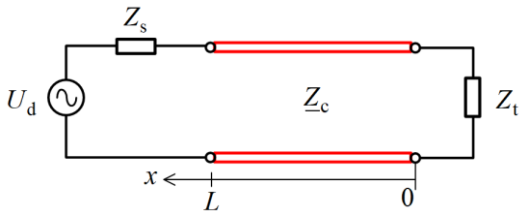

Figure B.6: Equivalent-circuit model for a traveling-wave modulator having a length L and a complex line impedance $\underline{Z}_c$. The device is driven by an RF source with an internal impedance Z_s and a voltage amplitude U_d. Z_t denotes the termination impedance.

probe that was earlier used as a termination of the CPW. For calibration and de-embedding, we apply the line–reflect–reflect–match[153] and the 'L-2L de-embedding' technique, described in Section 4.6 of [154]. The transfer function of the RF fixtures, i.e., the on-chip metal contact pads and the tapered transitions to the metal strips of the transmission line, are de-embedded by using *S*-parameter measurements of CC-SOH MZM of different modulator lengths. Based on this, we extract the complex propagation constant B_e as well as the complex line impedance $\underline{Z}_c$ of the CC-SOH transmission line. For estimating the EO response of the traveling-wave modulator, we use the equivalent circuit shown in Fig. B.6. We assume a device of length L and a complex RF impedance $\underline{Z}_c$, driven by an RF source of internal impedance Z_s at RF modulation frequency $\Omega_m/2\pi$ and voltage amplitude U_d, and terminated by an impedance Z_t. The instantaneous voltage seen by the optical signal at a particular position on the line is then given by Eqs. 1 – 5 in [123],

$$U\left(x,\omega_m\right)=\frac{U_d}{2}\cdot\left(1+\rho_1\right)\cdot e^{-jB_oL}\cdot\frac{e^{-j\left(B_e-B_o\right)x}+\rho_2\cdot e^{j\left(B_e+B_o\right)x}}{e^{-jB_eL}+\rho_1\cdot\rho_2\cdot e^{jB_eL}} \tag{B.12}$$

$$\rho_1=\frac{\underline{Z}_c-Z_s}{\underline{Z}_c+Z_s} \tag{B.13}$$

$$\rho_2=\frac{Z_t-\underline{Z}_c}{Z_t+\underline{Z}_c} \tag{B.14}$$

$$B_o=\frac{\Omega_m}{c_0}n_{g,opt} \tag{B.15}$$

$$B_{\mathrm{e}} = \frac{\Omega_{\mathrm{m}}}{c_0} n_{\mathrm{e,RF}} + \mathrm{j}\alpha_{\mathrm{m}} \tag{B.16}$$

In these relations, α_{m} is the amplitude attenuation constant of the RF signal, $n_{\mathrm{g,opt}}$ denotes the optical group refractive index, $n_{\mathrm{e,RF}}$ is the effective index of the RF signal, and c_0 is the speed of light in vacuum. The phase shift experienced by an optical wave traveling through the modulator is directly proportional to the voltage experienced by it along the length of the phase shifter. To simplify the analysis, it is convenient to work with the average voltage along the length L of the modulator, see Eq. 17 in Ref.[122],

$$\begin{aligned} U_{\mathrm{avg}}\left(\Omega_{\mathrm{m}}\right) &= \frac{1}{L}\int_0^L U\left(x,\Omega_{\mathrm{m}}\right)\mathrm{d}x \\ &= \frac{U_{\mathrm{d}}\cdot\left(1+\rho_1\right)\cdot e^{-\mathrm{j}B_{\mathrm{o}}L}}{2\left(e^{-\mathrm{j}B_{\mathrm{e}}L}+\rho_1\cdot\rho_2\cdot e^{-\mathrm{j}B_{\mathrm{e}}L}\right)}\cdot\left(U_{+}+\rho_2\cdot U_{-}\right), \end{aligned} \tag{B.17}$$

where

$$U_{\pm} = e^{\pm\mathrm{j}\phi_{\pm}}\frac{\sin\phi_{\pm}}{\phi_{\pm}}, \quad \phi_{\pm} = \frac{\left(B_{\mathrm{e}}\mp B_{\mathrm{o}}\right)L}{2}. \tag{B.18}$$

Note that Eq. (B.17) accounts for the impact of RF propagation loss, the impedance mismatch of the modulator transmission line with respect to the source and the termination, as well as velocity mismatch of the RF and the optical waves of the traveling-wave modulator. The optical group refractive index $n_{\mathrm{g,opt}} = 2.8$ needed in Eq. (B.15) is numerically calculated using a commercially available optical mode solver (CST Microwave Studio).

For relating the frequency-dependent decay of the average voltage U_{avg} to the phase modulation of the optical signal, we exploit the fact that the relative permittivity $\varepsilon_{\mathrm{r,BTO}} = 18$ is constant over the frequency range of interest, Appendix B.52D. Since the transverse dimensions of the RF transmission lines are much smaller than the RF wavelength, we may hence assume that the RF field profiles change only marginally with modulation frequency Ω_{m}. The amplitude of the phase modulation is hence directly proportional to the average voltage

$U_{\mathrm{avg}}(\omega_{\mathrm{m}})$ on the transmission line, and the EO frequency response can be written as

$$m(\Omega_{\mathrm{m}}) = \left| \frac{U_{\mathrm{avg}}(\Omega_{\mathrm{m}})}{U_{\mathrm{avg}}(0)} \right|. \tag{B.19}$$

We finally obtain the dB-values of the EO response derived from the electrical scattering parameters of the CC-SOH MZM as $S_{21,\mathrm{EO,der}} = 20\log_{10}\left(m(\Omega_{\mathrm{m}})\right)$. For a device with a phase shifter length of $L = 1\,\mathrm{mm}$, the results are indicated by a blue dotted line in Fig. B.5. The EO response $S_{21,\mathrm{EO,der}}$ derived from the electrical scattering parameters is in fair agreement with its directly measured counterpart $S_{21,\mathrm{EO,meas}}$, thus confirming the validity of the approach.

Furthermore, we investigate the limiting factors for the bandwidth of the CC-SOH MZM. From the numerically calculated value of $n_{\mathrm{g,opt}}$ and the mean RF effective index $\bar{n}_{\mathrm{e,RF}} = 2.2$ averaged over the frequency range 0.01 GHz … 110 GHz, the velocity-mismatch-limited 3dB-bandwidth of a CC-SOH device is given by Eq. 2 in Ref.[124],

$$f_{\mathrm{vm}} = 1.4 \frac{c_0}{\left(\pi \left| n_{g,\mathrm{opt}} - \bar{n}_{\mathrm{e,RF}} L \right|\right)}. \tag{B.20}$$

For our 1 mm-long CC-SOH devices, we estimate a velocity-mismatch-limited 3 dB frequency of $f_{\mathrm{vm}} = 220\,\mathrm{GHz}$. It is thus clear that the bandwidth limitation of 76 GHz observed in our current measurements cannot be caused by velocity mismatch but must arise from the non-optimum electrical design of our first-generation device, in particular from the high RF propagation loss.

In general, RF propagation loss has two main contributions – ohmic loss and dielectric loss. As discussed in Appendix B.2.5 above, the BTO thin film has a negligibly small loss tangent $\tan\delta_{\mathrm{BTO}} = 0.03$. This results in a bulk BTO loss of only 0.38 dB/mm, which is much smaller than the overall RF propagation loss of 4.5 dB/mm at 50 GHz, see red curve in Fig. B.7. We hence conclude that ohmic losses of the metal traces of the transmission line must have significant impact. As mentioned in Chapter 5, these traces were fabricated using a lift-off process with a thin photoresist, which limited the thickness of the gold layer to a rather small value of approximately 150 nm. To confirm the notion

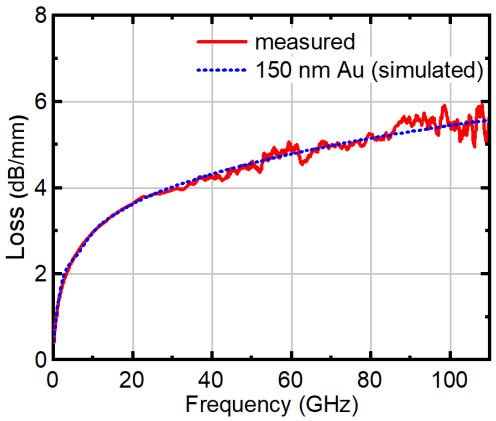

Figure B.7: Frequency-dependent RF propagation loss of the fabricated CC-SOH MZM. The red solid curve corresponds to the measurement, and blue dotted curve to a simulation based on a 150 nm-thick gold (Au) transmission line. In the simulation, we assumed a conductivity $\sigma_{\mathrm{Au}} = 2.6\times10^{7}\,\mathrm{S/m}$ for the gold to best match the measurement. The conductivity of the underlying bulk Si substrate amounts to $\sigma_{\mathrm{Si}} = 0.13\,\mathrm{S/m}$.

that this leads to strong ohmic RF losses, we simulate the RF mode of the CC-SOH device using the same technique as described in Appendix B.2.5. For the BTO, we assume again a relative permittivity $\varepsilon_{\mathrm{r,BTO}} = 18$ and a loss tangent $\tan\delta_{\mathrm{BTO}} = 0.03$, and we also consider the conductivity of the bulk Si substrate, for which a value of $\sigma_{\mathrm{Si}} = 0.13\,\mathrm{S/m}$ was specified by the wafer supplier. In our simulations, we vary the conductivity of the gold traces, and we find best agreement with the measured losses for a value of $\sigma_{\mathrm{Au}} = 2.6\times10^{7}\,\mathrm{S/m}$, see red and blue curves in Fig. B.7. This value agrees well with the gold conductivity of $\sigma_{\mathrm{Au}} = 2.5\times10^{7}\,\mathrm{S/m}$ obtained from the characterization of the CPW test structures, Appendix B.2.5. Based on these findings, we conclude that the RF propagation loss of the current CC-SOH devices arises from the ohmic loss of the thin gold traces in the underlying transmission line, and that these limitations can be overcome by using thicker metal layers, see Appendix B.5 below for improved device designs.

B.4 Pre-emphasis of the drive signals in the high-speed signaling experiments

In the high-speed signaling experiments, we use digital pre-emphasis of the drive signals to compensate for the frequency roll-off of the AWG, of the subsequent RF amplifier, of the 6 dB attenuator, and of the bias-tee, see Section 5.4 and Fig. 5.3(a). The required correction is extracted from a back-to-back measurement of the electrical signal, in which the AWG is operated without any pre-emphasis to generate a test signal. This test signal is then sent through the subsequent RF amplifier, the 6 dB attenuator, and the bias-tee, see left part of Fig. 5.3(a), before being recorded by a real-time oscilloscope (RTO). To estimate the digital pre-emphasis that needs to be applied at the transmitter, the frequency spectrum of the recorded signal is then compared to that of the idea (transmitted) spectrum. For the data transmission experiment, the CC-SOH modulator, the corresponding RF probe, the optical transmission link, the photodetector as well as another RF amplifier are then added, leading to the full setup shown in Fig. 5.3(a). None of these elements was part of the signal path during the calibration measurement – they are hence not compensated by the estimated pre-emphasis.

B.5 Improved designs of CC-SOH modulators

The experimental results presented in Chapter 5 were obtained with first-generation devices that leave vast room for improvements with respect to modulation efficiency and bandwidth. In this section, we shall further investigate the potential of the CC-SOH concept by numerical simulations of devices with improved designs, in which we adjust the various geometrical parameters defined in Fig. 5.1(c). Regarding the modulation efficiency, the $U_\pi L$ product of the devices may be greatly reduced by using polycrystalline BTO layers with relative permittivities $\varepsilon_{\mathrm{r,BTO}} \geq 100$ [126], [128], which is much larger than the value of $\varepsilon_{\mathrm{r,BTO}} = 18$ in our current devices. In addition, the dimensions of the BTO slabs may be adapted to find an optimum trade-off between different design goals. Specifically, increasing the height h_{hk} beyond the current value of 150 nm will be instrumental to improve the overlap of the RF field and the optical field and thus to further increase the field interaction factor Γ_{s}. On the other hand, a

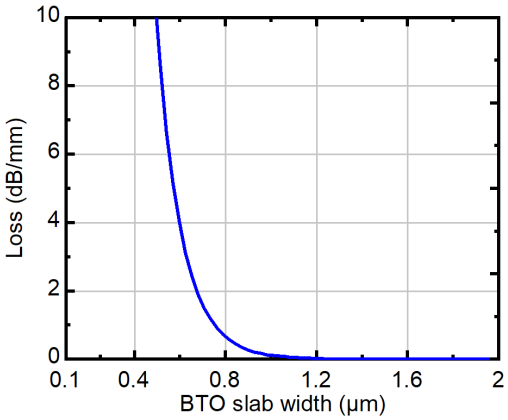

Figure B.8: Optical loss due to interaction of the guided light with the metal traces of the RF transmission line as a function of the BTO slab width w_{hk}. For $w_{\mathrm{hk}} \geq 1\,\mu\mathrm{m}$, the loss contribution of the transmission line is less than 0.1 dB/mm and can thus be neglected.

thicker BTO will increase the transverse capacitance of the line and thus lead to a reduced line impedance Z_{RF}. In combination with a given operation voltage of the MZM dictated by the required phase shift, this will increase the RF power consumption. For the width w_{hk} of the BTO slabs, choosing a small value leads to an increased coupling capacitance C_{c} and thus an increased modulation efficiency, but also results in larger interaction of the optical mode with the metal traces of the RF transmission line and therefore increases the optical losses. With respect to the ground-signal-ground (GSG) RF transmission-line, we may increase the height h_{m} of the metal traces to reduce the RF losses of the CC-SOH device and to thus increase the bandwidth. On the other hand, if the height h_{m} of the metal is chosen too thick, the RF electric field will extend vertically and thus occupies regions of the organic EO material which do not contain significant optical power. This will reduce field interaction factor, see Eq. (B.10). Besides the height h_{m}, the width w_{sig} of the signal trace may be adapted to tune the line impedance to a certain target value of, e.g., 50 Ω. In the following, we systematically vary all these parameters and investigate their impact on the field interaction factor Γ_{s}, the line impedance Z_{RF} as well as on the optical and the RF losses of the CC-SOH device. For the BTO, we assume a relative permittivity $\varepsilon_{\mathrm{r,BTO}} = 100$ and a refractive index of $n_{\mathrm{BTO}} = 1.85$, while the optical and the RF properties of all other materials correspond to those specified in Appendix B.1. The dimensions of the optical slot waveguide are kept at the previously

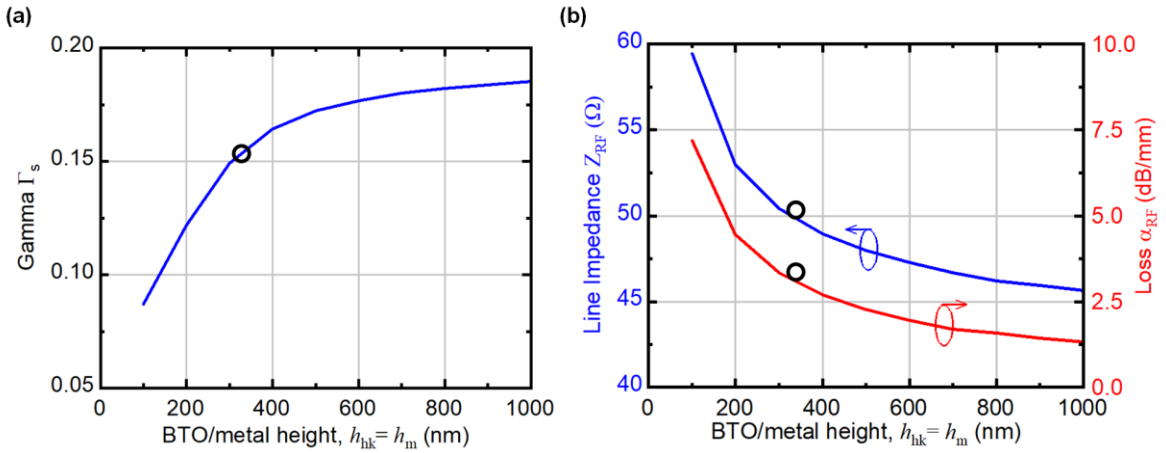

Figure B.9: Impact of BTO/metal height $h_m = h_{hk}$ on various parameters of the CC-SOH modulator. The width of the BTO and of the signal trace are kept to constant values of $w_{hk} = 1\,\mu m$ and $w_{sig} = 4\,\mu m$, respectively. **(a)** Field interaction factor Γ_s for different BTO/metal heights $h_m = h_{hk}$. The field interaction factor reaches a plateau at $\Gamma_s \approx 0.17$ for $h_m = h_{hk} > 600$ nm, **(b)** Microwave propagation loss α_{RF} and RF line impedance Z_{RF} at 50 GHz for different BTO/metal heights $h_m = h_{hk}$. Circles indicate the RF propagation loss and field interaction factor of a transmission line with a line impedance of $Z_{RF} = 50\,\Omega$.

used values of $h_{rail} = 220$ nm, $w_{rail} = 200$ nm, $w_s = 100$ nm, and the vacuum wavelength of the optical signal amounts to 1.55 µm.

In a first step of our design considerations, we estimate the optical propagation loss introduced by the interaction of the evanescent field with the metal transmission lines. To this end, we assume the BTO slabs and the metal traces to have the same height $h_m = h_{hk} = 150$ nm and calculate the contribution to the optical propagation loss as a function of the width w_{hk} of the BTO slabs, see Fig. B.8. We find that, for values of $w_{hk} \geq 1\,\mu m$, the loss contribution of the metal trace is below 0.1 dB/mm and can thus be neglected. In the subsequent simulations, we fix the width of the BTO slab to the value of $w_{hk} = 1\,\mu m$.

As a next step, we simulate the CC-SOH devices by treating the Si rails as pure dielectrics with zero conductivity and by setting the BTO height h_{hk} and the metal height h_m to the same value, which is swept between 100 nm and 1 µm, see Fig. B.9. In these simulations the width of the BTO and of the signal trace are kept to constant values of $w_{hk} = 1\,\mu m$ and $w_{sig} = 4\,\mu m$. As expected, the field interaction factor Γ_s increases steadily with $h_m = h_{hk}$ and finally saturates for $h_m = h_{hk} > 600$ nm, see Fig. B.9(a). This saturation is caused by the fact that

an increasing height of the BTO slabs and the metal traces distributes the RF electric field into regions of the organic EO material, which do not contain significant optical power. At the same time, the RF losses and the impedance of the transmission line go down with increasing values of $h_{\mathrm{m}} = h_{\mathrm{hk}}$ due to the increased transverse capacitance and the reduced ohmic losses of the metal traces, see values calculated at 50 GHz in Fig. B.9(b). It turns out that, for a line impedance of $Z_{\mathrm{RF}} = 50\,\Omega$, the heights of the BTO slabs and the metal should be chosen to $h_{\mathrm{m}} = h_{\mathrm{hk}} \approx 300\,\mathrm{nm}$, which leads to non-optimum RF loss and field interaction factors, as indicated by circles in Fig. B.9. Thicker layers with $h_{\mathrm{m}} = h_{\mathrm{hk}} \geq 600\,\mathrm{nm}$ would lead to much better modulation efficiency and less RF loss, but the line impedance Z_{RF} would drop below the desired value of 50 Ω. This may be fixed by using slightly thinner BTO slabs.

For the next design iteration, we therefore set the height of the metal traces to a fixed value of $h_{\mathrm{m}} = 600\,\mathrm{nm}$ and we again sweep the height the sweep the height h_{hk} of the BTO slabs between 100 nm and 1 µm, see Fig. B.10. In addition to the non-conductive Si rails, we also consider the case of a slight doping in the rails designed for a resistivity of approximately $\rho = 5.5\times10^{-4}\,\Omega\mathrm{m}$ [32]. This conductivity should eliminate the electric field within the Si rails and thus increase the field in the EO material accordingly, see field plots in the insets of Fig. B.10(a). The chosen resistivity should not contribute any significant optical loss[32], and lead to a dielectric relaxation frequency in excess of 1 THz and thereby does not reduce the bandwidth of our devices. Note that our model is still fairly coarse – the silicon was represented as a simple conductive dielectric without considering the exact band structure and the internal distribution of mobile and fixed charges. Still, the results should give a reliable estimate of the performance that can be expected for CC-SOH devices. From our simulations we find that the devices with undoped silicon rails devices may now maintain a line impedance of $Z_{\mathrm{RF}} = 50\,\Omega$ for BTO heights of approximately $h_{\mathrm{hk}} = 350\,\mathrm{nm}$, which leads to an improved value of $\Gamma_{\mathrm{s}} \approx 0.14$ for the field interaction factor and to an RF propagation loss of about 1.7 dB/mm at 50 GHz, see blue traces and blue circles in Fig. B.10(a), (b), and (c). When using doped silicon slabs, these values can be further improved: For a line impedance of $Z_{\mathrm{RF}} = 50\,\Omega$, the BTO height can be increased to $h_{\mathrm{hk}} = 400\,\mathrm{nm}$, which leads to a field interaction factor of $\Gamma_{\mathrm{s}} \approx 0.32$ and to RF losses of about 2.3 dB/mm, see green traces and green circles in Fig. B.10(a), (b), and (c). This field interaction factor is only

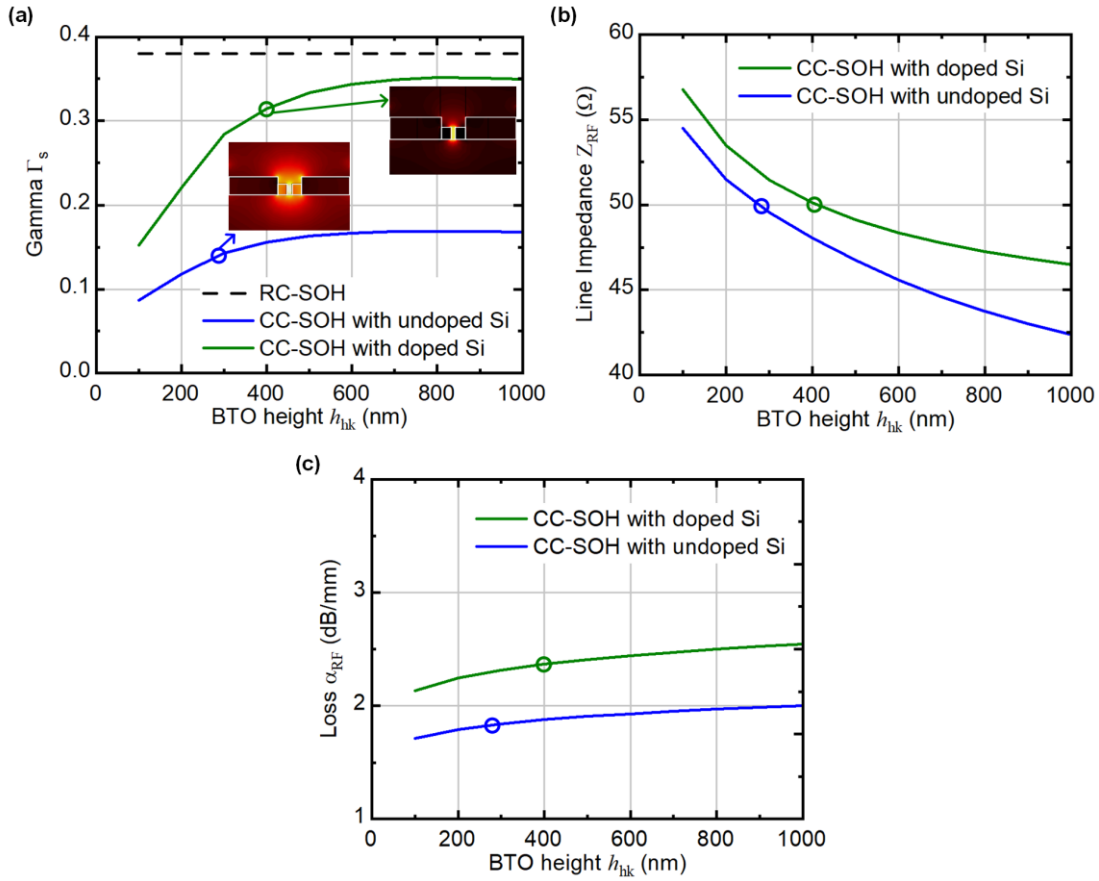

Figure B.10: Impact of BTO slab height h_{hk} on the field interaction factor Γ_s, line impedance Z_{RF} and RF loss α_{RF} for CC-SOH modulator with pure dielectric Si rails and doped ($\rho = 5.5\times10^{-4}$ Ωm) Si rails having $w_{hk} = 1\,\mu m$, $w_{sig} = 4\,\mu m$, and a metal thickness of 600 nm. **(a)** Field interaction factor Γ_s of CC-SOH modulator as a function of BTO slab height h_{hk}. As a comparison, the field interaction factor of RC-SOH modulator, $\Gamma_{RC\text{-}SOH} \approx 0.38$ is shown in black trace. Inset shows RF field profiles of CC-SOH devices with undoped and slightly doped Si rails at positions marked by the respectively colored circles. **(b)** Line impedance Z_{RF} of CC-SOH modulator for different slab heights. **(c)** RF propagation loss α_{RF} of CC-SOH modulator with and without doped Si rails for different BTO slab heights. The respective designs with doped and undoped Si rails having a good match to 50 Ω source impedance are marked in colored circles.

slightly smaller than the value of $\Gamma_{RC\text{-}SOH} \approx 0.38$ that can be achieved for conventional RC-SOH devices, see dashed black curve in Fig. B.10(a). We may hence conclude that the CC-SOH concept can reach similar modulation efficiencies as RC-SOH devices, for which $U_\pi L$ products down to 0.32 Vmm were demonstrated [26], while offering bandwidths in excess of 100 GHz.

Taking the above considerations, we also investigate the impact that an increased thickness of the metal traces would have on our current CC-SOH devices. To this end, we assume undoped Si rails along with 150 nm-thick BTO slabs having and 600 nm-thick metal traces. The width of the signal trace is kept to $w_{sig} = 7\,\mu m$. From this simulation, we extract the line impedance and the microwave propagation loss and then calculate the electro-optic (EO) response according to the model described in Appendix B.3C. The result is shown as a green trace in Fig. B.5 and in Fig. 5.2(d), corresponding to a bandwidth of more than 100 GHz. This clearly indicates that the performance of the experimentally demonstrated devices can be greatly improved by appropriate device designs.

[End of the Methods and Supplementary Information of paper [J3]]

C Recipes for fabrication of high-speed EO modulators

This appendix lists detailed recipes that are developed at the Institute of Microstructure Technology (IMT) and the Karlsruhe Nano Micro Facility (KNMF) for fabrication of high-speed EO modulators. The EO modulators are fabricated on silicon-on-insulator (SOI) chips having a 220 nm thick silicon device layer, 2 µm buried oxide (SiO_2) on a 725 µm thick silicon substrate.

In order to avoid surface contamination of the chip, the SOI chip is treated with the following 'sample cleaning' procedure between different process steps:

Sample cleaning

- 5 min rinse of the sample in a beaker of acetone placed in an ultrasonic bath for removing organic contaminants.
- 2 min rinse in a beaker of isopropanol placed in an ultrasonic bath for removing the acetone residues.
- 2 min rinse in de-ionized (DI) water to remove isopropanol residues and other particles if any.
  As a quick verification, the hydrophobic nature of the silicon (Si) confirms that the sample is free from organic residues and other contaminants. The hydrophobic property of silicon surface arises because water molecules cannot form H-bonds with the bare Si surface. Therefore, water molecules bond with other water molecules resembling a hydrophobic behaviour on the Si surface.
- Drying the sample with N_2 gas for removing remaining water along with the particles floating in it.

C.1 Fabrication of markers for high-accuracy alignment

Spin coating

After sample cleaning, the SOI chip is spin coated with a 300 nm thick bi-layer of poly-methyl methacrylate (PMMA) resist having different molecular weights. In this process, the bottom PMMA layer is slightly more sensitive with a lower molecular weight, while a PMMA with higher molecular weight serves as the top layer. Such a bi-layer resist is sometimes preferred to ensure a slight undercut in the developed resist to facilitate proper lift-off. The procedure of spin coating of bi-layer PMMA resist is described as follows:

- Spin coating of PMMA AR-P 662.04 (Allresist GmbH) with 600 k molecular weight, 775 rpm spin speed, acceleration 150 rpm/s, 60 s.
- Hot plate at 180°C for 5 min.
- Spin coating of PMMA AR-P 672.02 (Allresist GmbH) with 950 k molecular weight, 2000 rpm spin speed, acceleration 150 rpm/s, 60 s.
- Hot plate at 180°C for 5 min.

Lithography and development

The four corners of the resist-coated SOI chip are exposed with an octagonal-shaped marker using Raith EBPG5200 e-beam lithography system and subsequently developed:

- Exposure of markers in the bi-layer PMMA resist with a dose of 1000 $\mu C/cm^2$.
- Development of bi-layer PMMA for 50 s in a 1:3 solution of methyl isobutyl ketone (MIBK) and isopropanol, commonly referred to as MIBK:ISO 1:3. The development of the exposed structures is stopped by rinsing the sample in pure isopropanol, which is a standard process while developing any PMMA resist.

Metallization and lift-off

- Electron-beam evaporation (Leybold Univex 400) of 10 nm chromium (Cr) or titanium (Ti), followed by a gold (Au) thickness of 30 nm in a vacuum chamber with a pressure less than 10^{-6} mbar.
- Lift-off of the PMMA layer in a beaker of acetone placed in a low-power ultrasonic bath. The SOI chip is then subjected to the standard sample cleaning procedure.

C.2 Fabrication of partially etched structures in silicon

Spin coating

- Spin coating of 340 nm thick PMMA AR-P 672.045 (Allresist GmbH), 2000 rpm spin speed, acceleration 1000 rpm/s, 60 s.
- Hot plate at 180°C for 5 min.

Lithography and development

- Exposure of patterns in the PMMA resist with a dose of 950 μC/cm^2 without compensating for proximity effect correction (PEC).
- Development of PMMA resist in 1:3 MIBK:ISO for 25 s.

Reactive-ion-etching and resist stripping

The patterns developed in the PMMA resist are transferred 70 nm deep into the silicon device layer with inductively coupled plasma reactive-ion etching (ICP-RIE) using an Oxford Instruments Plasmalab 100 tool. Following the etching process, the PMMA mask is stripped in oxygen plasma machine.

- Partial etch of silicon is carried out at 20°C with a chemistry of CHF_3 and SF_6 and O_2 at flow rates of 7 sccm and 50 sccm, respectively and a pressure of 4.5 mTorr. The ICP power is 800 W, RF power is 8 W, etch time is 40 s.
  The etch rate was determined immediately before etching the SOI chip. To this end, a dummy sample of an identical SOI chip is etched, and the rate is determined by measuring the thickness of the dummy sample before and after etching with a spectroscopic ellipsometer. An etch rate of 10.0 nm/min was determined.
- After etching silicon, the remaining PMMA resist is stripped using an oxygen plasma tool at a working pressure of 10^{-3} mbar, O_2 flow rate of 30 sccm and an RF power of 100 W for 1 hr.

C.3 Fabrication of fully etched structures in silicon

Spin coating

- Spin coating of 180 nm thick 6 % hydrogen silsesquioxane (HSQ, Dow Corning), 1000 rpm spin speed, acceleration 1000 rpm/s, 30 s.
- Hot plate at 50°C for 10 min.

Lithography and development

- Exposure of patterns in the HSQ resist with a PEC dose 4500 µC/cm^2 for silicon waveguides, a non-PEC dose of 3500 µC/cm^2 for silicon pads of partially etched grating couplers, a dose of 2500 µC/cm^2 for fully etched grating coupler patterns.
- Development of HSQ resist in 25 % weight solution of tetra-methyl ammonium hydroxide (TMAH) in DI water for 5 min in a beaker placed on a shaker at 250 rpm. After the development of HSQ, the sample is rinsed for 30 s in isopropanol, followed by a 30 s rinse in DI water.

Reactive-ion-etching and resist stripping

- Cryogenic etch of silicon at – 110°C with a chemistry of SF_6 and O_2 at flow rates of 24 sccm and 6 sccm respectively. The ICP power is 800 W, RF power 8 W, pressure 4.5 mTorr, etch time of 16 s with a strike step of 4 s.
  Before etching the sample, the etch process is calibrated to fully etch Si device layer by tuning the etch time on a dummy SOI sample.
- After the full etch of silicon, the HSQ resist can be retained as its properties are very similar to that of SiO_2. However, for CC-SOH modulators, it is favorable to remove the HSQ resist to provide a direct contact with the overlap section of high-k slabs and the silicon slot waveguide.
  In order to strip HSQ, the sample is dipped into 5 % hydrogen fluoride (HF) acid for about 30 Sect. HF also attacks the buried oxide of the SOI chip, however, this can be neglected due to the short process time.

C.4 Fabrication of vertical-slot structures of POH modulators

Spin coating

- Spin coating of 330 nm thick PMMA AR-P 672.045, 2000 rpm spin speed, acceleration 1000 rpm/s, 60 s.
- Hot plate at 180°C for 5 min.
- Spin coating of a monolayer of ESPACER 300Z, 1500 rpm spin speed, 1000 rpm/s, 60 s.
  The thin film of ESPACER has a high conductivity and therefore eliminates the positional error of the e-beam, which in usual cases arises due to the charging of the sample during the lithography process.

Lithography and development

- Exposure of vertical plasmonic slot waveguides with a PEC dose of 700 µC/cm^2 – 750 µC/cm^2 and large metal contact pads with a PEC dose of 900 µC/cm^2.
- Development of PMMA for 25 s – 30 s in a 1:3 MIBK:ISO solution, followed by a rinse in isopropanol.

Metallization and lift-off

- E-beam evaporation of 5 nm Cr/Ti and 150 nm Au. For a proper lift-off of the vertical plasmonic slots, the sample temperature and the evaporation rate are carefully optimized.
- Lift-off of the PMMA layer in a beaker of n-methyl-2-pyrrolidone (NMP) at 65°C in medium-power ultrasonic bath. Thereafter, the SOI chip is subjected to the standard sample cleaning procedure at room temperature.

C.5 Fabrication of horizontal-slot structures of POH modulators

The horizontal plasmonic slot waveguide of HS-POH modulators are fabricated in a 3-step lithographic process. In step I, the bottom metal is fabricated and

step II forms the HSQ sacrificial layer of the plasmonic slot. In the final step III, the top metal is fabricated and the HSQ sacrificial layer is stripped. The detailed fabrication procedure is explained as follows

I – Spin coating

- Spin coating of 400 nm thick PMMA: AR-P 672.045, 1250 rpm spin speed, acceleration 1000 rpm/s, 60 s.
- Hot plate at 180°C for 5 min.

I – Lithography and development

- Exposure for patterning bottom metal of horizontal slot plasmonic waveguides with a PEC dose of 750 μC/cm^2.
- Development of PMMA for 25 s in a 1:3 MIBK:ISO solution, followed by a rinse in isopropanol.

I – Metallization and lift-off

- E-beam evaporation of 5 nm Cr/Ti and 70 nm Au.
- Lift-off of the PMMA layer in a beaker of acetone in low-power ultrasonic bath, followed by a rinse in isopropanol and DI water.

II – Spin coating

- Spin coating of 100 nm thick 6 % HSQ, 3500 rpm spin speed, acceleration 1000 rpm/s, 30 s.
- Hot plate at 50°C for 10 min.

II – Lithography and development

- Exposure of patterns in HSQ that will later form the slot region of the HS-POH modulator with a PEC dose of 3000 μC/cm^2.
- Development in 25 % TMAH solution for 5 min in a beaker, which is placed on a shaker at 250 rpm. After the development of HSQ, the sample is rinsed for 30 s in isopropanol, followed by a 30 s rinse in DI water.

III – Spin coating

- Spin coating of 600 nm thick bi-layer PMMA: AR-P 662.04, 500 rpm spin speed, acceleration 150 rpm/s, 60 s; AR-P 672.045, 700 rpm spin speed, acceleration 150 rpm/s, 60 s.
- Hot plate at 180°C for 5 min after each spin coating step.

III – Lithography and development

- Exposure for patterning top metal and the contact pads of HS-POH modulator with a PEC dose of 900 µC/cm^2.
- Development of PMMA for 140 s in a 1:3 MIBK:ISO solution, followed by a rinse in isopropanol.

III – Metallization and lift-off

- E-beam evaporation of 5 nm Cr/Ti and 200 nm Au.
- Lift-off of the PMMA layer in a beaker of acetone in low-power ultrasonic bath, followed by a rinse in isopropanol and DI water.

III – Sacrificial removal of HSQ

- Removal of HSQ in 5 % HF acid or buffered oxide etch (BOE) for 30 s, followed by a rinse in DI water.

To avoid the collapse of the top metal due to surface tension, the sample is dried using a critical point dryer (CPD).

C.6 Fabrication of transmission lines of CC-SOH modulators

Spin coating

- Spin coating of 400 nm thick PMMA AR-P 672.045, 1500 rpm spin speed, acceleration 1000 rpm/s, 60 s.
- Hot plate at 180°C for 5 min.

Lithography and development

- Exposure of patterns with a PEC dose of 800 µC/cm^2.

- Development of PMMA for 45 s in a 1:3 MIBK:ISO solution, followed by a rinse in isopropanol.

Metallization and lift-off

- E-beam evaporation of 5 nm Cr/Ti and 150 nm Au.
- Lift-off of the PMMA layer in a beaker of acetone in low-power ultrasonic bath, followed by a rinse in isopropanol and DI water.

C.7 Fabrication of BTO slabs of CC-SOH modulators

Spin coating

- Spin coating of about 950 nm thick bi-layer PMMA: 400 nm thick PMMA AR-P 662.04, 500 rpm spin speed, acceleration 1000 rpm/s, 60 s and 550 nm thick PMMA AR-P 672.045, 750 rpm spin speed, acceleration 150 rpm/s, 60 s.
- Hot plate at 180°C for 5 min after each spin coating step.

Lithography and development

- Exposure of patterns with a PEC dose of 1050 µC/cm^2.
- Development of PMMA for 45 s in a 1:1 MIBK:ISO solution, followed by a rinse in isopropanol.

RF sputtering and lift-off

The deposition of amorphous $BaTiO_3$ (BTO) is carried out in a custom-assembled RF magnetron sputtering tool at the institute of nanotechnology (INT), KIT.

- The 50 nm – 200 nm thick amorphous $BaTiO_3$ slabs are deposited at room-temperature using a stoichiometric $BaTiO_3$ disk with 2 inch diameter. The deposition is carried out at a base pressure of 5×10^{-8} mbar, and the working pressure 2.5×10^{-3} mbar is set to by controlling the flow rate (30 sccm) of Ar gas. A low RF power of 30 W is applied to the target

to keep the temperature of SOI chip below the glass transition temperature (110°C) of the PMMA mask to enable proper lift-off. To allow cooling of the chip, the deposition is carried out in multiple cycles with a 2.5 min deposition time and a 10 min pause time for each cycle.

- Lift-off of the PMMA layer in a beaker of n-methyl-2-pyrrolidone (NMP) at 65°C in medium-power ultrasonic bath. Thereafter, the SOI chip is subjected to the standard sample cleaning procedure at room temperature.

D Bibliography

[1] SPIE, “Optics & Photonics Industry Report 2020,” 2020. [Online]. Available: https://spie.org/news/2020-optics-and-photonics-industry-report.

[2] Cisco, “Cisco Visual Networking Index: Forecast and Trends, 2017-2022,” *White Paper*, 2019. [Online]. Available: https://www.cisco.com/c/en/us/solutions/collateral/service-provider/visual-networking-index-vni/white-paper-c11-741490.pdf.

[3] F. Testa and L. Pavesi, *Optical Switching in next Generation Data Centers*. Springer, 2018.

[4] E. L. Wooten *et al.*, “A Review of Lithium Niobate Modulators for Fiber-Optic Communications Systems,” *IEEE J. Sel. Top. Quantum Electron.*, vol. 6, no. 1, pp. 69–82, 2000.

[5] T. L. Koch and U. Koren, “Semiconductor Photonic Integrated Circuits,” *IEEE J. Quantum Electron.*, vol. 2727, no. 3, pp. 641–653, 1991.

[6] M. Smit, J. van der Tol, and M. Hill, “Moore’s Law in Photonics,” *Laser Photonics Rev.*, vol. 6, no. 1, pp. 1–13, 2012.

[7] M. Smit *et al.*, “An Introduction to InP-Based Generic Integration Technology,” *Semicond. Sci. Technol.*, vol. 29, no. 8, 2014.

[8] C. R. Doerr, “Silicon Photonic Integration in Telecommunications,” *Front. Phys.*, vol. 3, no. August, pp. 1–16, 2015.

[9] Infinera, “The Advantages of Indium Phosphide Photonic Integration in High-Performance Coherent Optics,” *White paper*, 2019. [Online]. Available: https://www.infinera.com/wp-content/uploads/The-Advantages-of-InP-Photonic-Integration-in-High-Performance-Coherent-Optics-0223-WP-RevA-1219.pdf.

[10] G. T. Reed, *Silicon Photonics: The State of the Art*. John Wiley & Sons, 2008.

[11] A. H. Atabaki *et al.*, “Integrating Photonics with Silicon Nanoelectronics for the next Generation of Systems on a Chip,” *Nature*, vol. 556, no. 7701, pp. 349–354, 2018.

[12] A. Liu *et al.*, “High-Speed Optical Modulation Based on Carrier Depletion in a Silicon Waveguide.,” *Opt. Express*, vol. 15, no. 2, pp. 660–668, 2007.

[13] S. S. Azadeh *et al.*, “Low Vπ Silicon Photonics Modulators with Highly Linear Epitaxially Grown Phase Shifters,” *Opt. Express*, vol. 23, no. 18, p. 23526, 2015.

[14] D. K. Schroder, R. N. Thomas, and J. C. Swartz, “Free Carrier Absorption

in Silicon," *IEEE J. Solid-State Circuits*, vol. 13, no. 1, pp. 180–187, 1978.
[15] M. M. R. Howlader, T. Suga, and M. J. Kim, "Room Temperature Bonding of Silicon and Lithium Niobate," *Appl. Phys. Lett.*, vol. 89, no. 3, pp. 1–4, 2006.
[16] G. Poberaj, H. Hu, W. Sohler, and P. Günter, "Lithium Niobate on Insulator (LNOI) for Micro-Photonic Devices," *Laser Photonics Rev.*, vol. 6, no. 4, pp. 488–503, 2012.
[17] C. Wang *et al.*, "Integrated Lithium Niobate Electro-Optic Modulators Operating at CMOS-Compatible Voltages," *Nature*, vol. 562, pp. 101–106, 2018.
[18] M. He *et al.*, "High-Performance Hybrid Silicon and Lithium Niobate Mach–Zehnder Modulators for 100 Gbit s -1 and Beyond," *Nat. Photon.*, vol. 13, no. 5, pp. 359–364, 2019.
[19] H. Liang, R. Luo, Y. He, H. Jiang, and Q. Lin, "High-Quality Lithium Niobate Photonic Crystal Nanocavities," *Optica*, vol. 4, no. 10, p. 1251, 2017.
[20] S. Abel *et al.*, "Controlling Tetragonality and Crystalline Orientation in $BaTiO_3$ Nano-Layers Grown on Si," *Nanotechnology*, vol. 24, no. 28, p. 285701, 2013.
[21] S. Abel *et al.*, "A Strong Electro-Optically Active Lead-Free Ferroelectric Integrated on Silicon," *Nat. Commun.*, vol. 4, p. 1671, 2013.
[22] S. Abel *et al.*, "A Hybrid Barium Titanate – Silicon Photonics Platform for Ultraefficient Electro-Optic Tuning," vol. 34, no. 8, pp. 1688–1693, 2016.
[23] S. Abel *et al.*, "Large Pockels Effect in Micro- and Nanostructured Barium Titanate Integrated on Silicon," *Nat. Mater.*, vol. 18, no. 1, pp. 42–47, 2019.
[24] F. Eltes *et al.*, "A BaTiO3-Based Electro-Optic Pockels Modulator Monolithically Integrated on an Advanced Silicon Photonics Platform," *J. Lightwave Technol.*, vol. 37, no. 5, pp. 1456–1462, 2019.
[25] L. R. Dalton, P. Günter, M. Jazbinsek, and O. P. Kwon, *Organic Electro-Optics and Photonics: Molecules, Polymers and Crystals*. Cambridge University Press, 2015.
[26] C. Kieninger *et al.*, "Ultra-High Electro-Optic Activity Demonstrated in a Silicon-Organic Hybrid (SOH) Modulator," *Optica*, vol. 5, no. 6, pp. 739–748, Sep. 2018.
[27] L. Alloatti *et al.*, "100 GHz Silicon-Organic Hybrid Modulator," *Light Sci. Appl.*, vol. 3, no. e173, pp. 5–8, 2014.
[28] C. Kieninger *et al.*, "Ultra-High Electro-Optic Activity Demonstrated in a

Silicon-Organic Hybrid (SOH) Modulator," *Optica*, vol. 5, no. 6, pp. 739–748, 2018.
[29] C. Kieninger *et al.*, "Silicon-Organic Hybrid (SOH) Mach-Zehnder Modulators for 100 GBd PAM4 Signaling with Sub-1 DB Phase-Shifter Loss," *Opt. Express*, vol. 28, no. 17, pp. 24693–24707, 2020.
[30] S. Wolf *et al.*, "DAC-Less Amplifier-Less Generation and Transmission of QAM Signals Using Sub-Volt Silicon-Organic Hybrid Modulators," *J. Lightwave Technol.*, vol. 33, no. 7, pp. 1425–1432, 2015.
[31] S. Wolf *et al.*, "Silicon-Organic Hybrid (SOH) Mach-Zehnder Modulators for 100 Gbit/s on-off Keying," *Sci. Rep.*, vol. 8, no. 1, pp. 1–13, 2018.
[32] H. Zwickel *et al.*, "Verified Equivalent-Circuit Model for Slot-Waveguide Modulators," *Opt. Express*, vol. 28, no. 9, pp. 12951–12976, 2020.
[33] A. Melikyan *et al.*, "High-Speed Plasmonic Phase Modulators," *Nat. Photon.*, vol. 8, no. 3, pp. 229–233, Feb. 2014.
[34] C. Haffner *et al.*, "All-Plasmonic Mach–Zehnder Modulator Enabling Optical High-Speed Communication at the Microscale," *Nat. Photon.*, vol. 9, no. 8, pp. 525–528, Jul. 2015.
[35] M. Ayata *et al.*, "High-Speed Plasmonic Modulator in a Single Metal Layer," *Science*, vol. 358, no. 6363, pp. 630–632, 2017.
[36] C. Koos *et al.*, "Silicon-Organic Hybrid (SOH) and Plasmonic-Organic Hybrid (POH) Integration," *J. Lightwave Technol.*, vol. 34, no. 2, pp. 256–268, 2016.
[37] R. W. Boyd, *Nonlinear Optics*, 3rd ed. Academic Press, 2008.
[38] R. J. Essiambre, G. J. Foschini, P. J. Winzer, G. Kramer, and B. Goebel, "Capacity Limits of Optical Fiber Networks," *J. Lightwave Technol.*, vol. 28, no. 4, pp. 662–701, 2010.
[39] G. T. Reed, G. Mashanovich, F. Y. Gardes, and D. J. Thomson, "Silicon Optical Modulators," *Nat. Photon.*, vol. 4, no. 8, pp. 518–526, Jul. 2010.
[40] R. A. Soref and B. R. Bennett, "Electrooptical Effects in Silicon," *IEEE J. Quantum Electron.*, vol. 23, no. 1, pp. 123–129, 1987.
[41] L. R. Dalton, P. A. Sullivan, and D. H. Bale, "Electric Field Poled Organic Electro-Optic Materials: State of the Art and Future Prospects," *Chem. Rev.*, vol. 110, no. 1, pp. 25–55, 2010.
[42] J. Leuthold *et al.*, "Silicon-Organic Hybrid Electro-Optical Devices," *IEEE J. Sel. Top. Quantum Electron.*, vol. 19, no. 6, pp. 340413–340143, 2013.
[43] S. Koeber *et al.*, "Femtojoule Electro-Optic Modulation Using a Silicon-Organic Hybrid Device," *Light Sci. Appl.*, vol. 4, no. 2, 2015.
[44] S. Wolf *et al.*, "Coherent Modulation up to 100 GBd 16QAM Using

Silicon-Organic Hybrid (SOH) Devices," *Opt. Express*, vol. 26, no. 1, p. 220, 2018.
[45] H. Zwickel *et al.*, "Silicon-Organic Hybrid (SOH) Modulators for Intensity-Modulation / Direct-Detection Links with Line Rates of up to 120 Gbit/S," *Opt. Express*, vol. 25, no. 20, p. 23784, 2017.
[46] V. R. Almeida, Q. Xu, C. A. Barrios, and M. Lipson, "Guiding and Confining Light in Void Nanostructure," *Opt. Lett.*, vol. 29, no. 11, p. 1209, 2004.
[47] R. Palmer *et al.*, "Low-Loss Silicon Strip-to-Slot Mode Converters," *IEEE Photonics J.*, vol. 5, no. 1, p. 2200409, 2013.
[48] J. M. Liu, *Photonic Devices*. Cambridge University Press, 2005.
[49] J. Witzens, T. Baehr-Jones, and M. Hochberg, "Design of Transmission Line Driven Slot Waveguide Mach-Zehnder Interferometers and Application to Analog Optical Links," *Opt. Express*, vol. 18, no. 16, p. 16902, 2010.
[50] D. K. Gramotnev and S. I. Bozhevolnyi, "Plasmonics beyond the Diffraction Limit," *Nat. Photon.*, vol. 4, no. 2, pp. 83–91, 2010.
[51] S. A. Maier, *Plasmonics: Fundamentals and Applications*. Springer, 2007.
[52] G. Veronis and S. Fan, "Modes of Subwavelength Plasmonic Slot Waveguides," *J. Lightwave Technol.*, vol. 25, no. 9, pp. 2511–2521, 2007.
[53] A. Melikyan, "Active and Passive Plasmonic Devices for Optical Communications," PhD Thesis, Karlsruhe Institute of Technology, 2014.
[54] W. Heni *et al.*, "Nonlinearities of Organic Electro-Optic Materials in Nanoscale Slots and Implications for the Optimum Modulator Design," *Opt. Express*, vol. 25, no. 3, p. 2627, 2017.
[55] S. Ummethala *et al.*, "THz-to-Optical Conversion in Wireless Communications Using an Ultra-Broadband Plasmonic Modulator," *Nat. Photon.*, vol. 13, no. 8, pp. 519–524, 2019.
[56] S. Shi and D. W. Prather, "Dual Rf-Optical Slot Waveguide for Ultrabroadband Modulation with a Subvolt Vπ," *Appl. Phys. Lett.*, vol. 96, no. 20, pp. 6–9, 2010.
[57] S. Shi and D. W. Prather, "Ultrabroadband Electro-Optic Modulator Based on Hybrid Silicon-Polymer Dual Vertical Slot Waveguide," *Adv. Optoelectron.*, vol. 2011, no. 714895, 2011.
[58] T. Nagatsuma, G. Ducournau, and C. C. Renaud, "Advances in Terahertz Communications Accelerated by Photonics," *Nat. Photon.*, vol. 10, no. 6, pp. 371–379, 2016.
[59] T. Kürner and S. Priebe, "Towards THz Communications - Status in

Research, Standardization and Regulation," *J. Infrared, Millimeter, Terahertz Waves*, vol. 35, no. 1, pp. 53–62, 2014.

[60] A. J. Seeds, H. Shams, M. J. Fice, and C. C. Renaud, "Terahertz Photonics for Wireless Communications," *J. Lightwave Technol.*, vol. 33, no. 3, pp. 579–587, 2015.

[61] "Cisco Visual Networking Index: Forecast and Methodology, 2016-2021," *White Paper*, 2017. [Online]. Available: http://www.cisco.com/c/en/us/solutions/collateral/service-provider/visual-networking-index-vni/complete-white-paper-c11-481360.pdf.

[62] C. W. Chow *et al.*, "100 GHz Ultra-Wideband (UWB) Fiber-to-the-Antenna (FTTA) System for in-Building and in- Home Networks," *Opt. Express*, vol. 18, no. 2, pp. 11–15, 2010.

[63] S. Koenig *et al.*, "Wireless Sub-THz Communication System with High Data Rate," *Nat. Photon.*, vol. 7, no. 12, pp. 977–981, Oct. 2013.

[64] X. Yu *et al.*, "160 Gbit/s Photonics Wireless Transmission in the 300-500 GHz Band," *APL Photonics*, vol. 1, no. 8, p. 081301, 2016.

[65] X. Pang *et al.*, "260 Gbit/s Photonic-Wireless Link in the THz Band," in *IEEE Photonics Conference (IPC)*, 2016, no. October, pp. 1–2.

[66] A. Beling and J. C. Campbell, "InP-Based High-Speed Photodetectors," *J. Lightwave Technol.*, vol. 27, no. 3, pp. 343–355, 2009.

[67] A. Kanno *et al.*, "Coherent Terahertz Wireless Signal Transmission Using Advanced Optical Fiber Communication Technology," *J. Infrared, Millimeter, Terahertz Waves*, vol. 36, no. 2, pp. 180–197, 2015.

[68] T. Nagatsuma *et al.*, "Terahertz Wireless Communications Based on Photonics Technologies," *Opt. Express*, vol. 21, no. 20, p. 23736, 2013.

[69] C. Wang *et al.*, "0.34-THz Wireless Link Based on High-Order Area Network Applications," *IEEE Trans. Terahertz Sci. Technol.*, vol. 4, no. 1, pp. 75–85, 2014.

[70] T. W. Crowe, "GaAs Schottky Barrier Mixer Diodes for the Frequency Range 1-10 THz," *Int. J. Infrared Millimeter Waves*, vol. 10, no. 7, pp. 765–777, 1989.

[71] T. Harter *et al.*, "110-m THz Wireless Transmission at 100 Gbit/s Using a Kramers-Kronig Schottky Barrier Diode Receiver," in *44th European Conference on Optical Communication (ECOC'18)*, 2018, p. Th3F.7 (postdeadline paper).

[72] S. Ummethala *et al.*, "Terahertz-to-Optical Conversion Using a Plasmonic Modulator," in *Conference on Lasers and Electro-Optics*, 2018, p. STu3D.4.

[73] S. Ummethala, T. Harter, K. Koehnle, Z. Li, S. Muehlbrandt, and Y. Kutuvantavida, “Wireless Transmission at 0.3 THz Using Direct THz-to-Optical Conversion at the Receiver,” in *44th European Conference on Optical Communication (ECOC’18)*, 2018, p. We4H.3.
[74] Y. Salamin *et al.*, “Direct Conversion of Free Space Millimeter Waves to Optical Domain by Plasmonic Modulator Antenna,” *Nano Lett.*, vol. 15, pp. 8342–8346, 2015.
[75] A. Melikyan *et al.*, “Plasmonic-Organic Hybrid (POH) Modulators for OOK and BPSK Signaling at 40 Gbit/S,” *Opt. Express*, vol. 23, no. 8, pp. 9938–9946, 2015.
[76] C. Haffner *et al.*, “Low-Loss Plasmon-Assisted Electro-Optic Modulator,” *Nature*, vol. 556, no. 7702, pp. 483–486, 2018.
[77] C. Hoessbacher *et al.*, “Plasmonic Modulator with >170 GHz Bandwidth Demonstrated at 100 GBd NRZ,” *Opt. Express*, vol. 25, no. 3, pp. 1762–1768, 2017.
[78] J. Macario *et al.*, “Full Spectrum Millimeter-Wave Modulation,” *Opt. Express*, vol. 20, no. 21, pp. 810–815, 2012.
[79] M. Andrew J., S. Shouyan, Y. Peng, X. Linli, M. W. Robert, and W. P. Dennis, “Thin Film Lithium Niobate Electro-Optic Modulator with Terahertz Operating Bandwidth,” *Opt. Express*, vol. 26, no. 11, pp. 14810–14816, 2018.
[80] G. Veronis and S. Fan, “Modes of Subwavelength Plasmonic Slot Waveguides,” *J. Lightwave Technol.*, vol. 25, no. 9, pp. 2511–2521, 2007.
[81] G. Veronis and S. Fan, “Guided Subwavelength Plasmonic Mode Supported by a Slot in a Thin Metal Film.,” *Opt. Lett.*, vol. 30, no. 24, pp. 3359–3361, 2005.
[82] D. F. P. Pile, D. K. Gramotnev, R. F. Oulton, and X. Zhang, “On Long-Range Plasmonic Modes in Metallic Gaps,” *Opt. Express*, vol. 15, no. 21, p. 13669, 2007.
[83] A. M. Urbas *et al.*, “Roadmap on Silicon Photonics,” *J. Opt.*, vol. 18, no. 7, p. 073003, 2016.
[84] D. F. P. Pile and D. K. Gramotnev, “Adiabatic and Nonadiabatic Nanofocusing of Plasmons by Tapered Gap Plasmon Waveguides,” *Appl. Phys. Lett.*, vol. 89, no. 4, p. 041111, 2006.
[85] Y. Enami, J. Luo, and A. K. Y. Jen, “Short Hybrid Polymer/Sol-Gel Silica Waveguide Switches with High in-Device Electro-Optic Coefficient Based on Photostable Chromophore,” *AIP Adv.*, vol. 1, no. 4, p. 042137, 2011.
[86] Y. Shi, L. Yan, and A. E. Willner, “High-Speed Electrooptic Modulator

Characterization Using Optical Spectrum Analysis," *J. Lightwave Technol.*, vol. 21, no. 10, pp. 2358–2367, 2003.

[87] G. V. Naik, V. M. Shalaev, and A. Boltasseva, "Alternative Plasmonic Materials: Beyond Gold and Silver," *Adv. Mater.*, vol. 25, no. 24, pp. 3264–3294, 2013.

[88] C. Haffner *et al.*, "Harnessing Nonlinearities near Material Absorption Resonances for Reducing Losses in Plasmonic Modulators," *Opt. Mater. Express*, vol. 7, no. 7, pp. 2168–2181, 2017.

[89] F. Chang, K. Onohara, and T. Mizuochi, "Forward Error Correction for 100 G Transport Networks," *IEEE Commun. Mag.*, vol. 48, no. 3, pp. 48–55, 2010.

[90] W. Heni *et al.*, "Nonlinearities of Organic Electro-Optic Materials in Nanoscale Slots and Implications for the Optimum Modulator Design," vol. 25, no. 3, pp. 2627–2653, 2017.

[91] M. Burla *et al.*, "500 GHz Plasmonic Mach-Zehnder Modulator Enabling Sub-THz Microwave Photonics," *APL Photonics*, vol. 4, no. 5, p. 056106, 2019.

[92] A. Melikyan, M. Kohl, M. Sommer, C. Koos, W. Freude, and J. Leuthold, "Photonic-to-Plasmonic Mode Converter," *Opt. Lett.*, vol. 39, no. 12, pp. 3488–3491, 2014.

[93] C. Weimann *et al.*, "Silicon-Organic Hybrid (SOH) Frequency Comb Sources for Terabit / s Data Transmission," vol. 22, no. 3, pp. 3629–3637, 2014.

[94] S. Lange *et al.*, "100 GBd Intensity Modulation and Direct Detection with an InP-Based Monolithic DFB Laser Mach-Zehnder Modulator," *J. Lightwave Technol.*, vol. 36, no. 1, pp. 97–102, 2018.

[95] A. Melikyan, N. Kaneda, K. Kim, N. B. Labs, and H. Road, "100 Gbaud QAM Signaling with Silicon Photonic Electro-Absorption Modulators," in *45th European Conference on Optical Communication*, 2019, p. PD2.5 (postdeadline).

[96] C. Weimann, M. Lauermann, F. Hoeller, W. Freude, and C. Koos, "Silicon Photonic Integrated Circuit for Fast and Precise Dual-Comb Distance Metrology," *Opt. Express*, vol. 25, no. 24, pp. 30091–30104, 2017.

[97] D. Marpaung, J. Yao, and J. Capmany, "Integrated Microwave Photonics," *Nat. Photon.*, vol. 13, no. 2, pp. 80–90, 2019.

[98] K. Giewont *et al.*, "300-Mm Monolithic Silicon Photonics Foundry Technology," *IEEE J. Sel. Top. Quantum Electron.*, vol. 25, no. 5, p. 8200611, 2019.

[99] J. Witzens, "High-Speed Silicon Photonics Modulators," *Proc. IEEE*, vol. 106, no. 12, pp. 2158–2182, 2018.
[100] C. Koos, J. Brosi, M. Waldow, W. Freude, and J. Leuthold, "Silicon-on-Insulator Modulators for Next-Generation 100 Gbitls-Ethernet," in *33rd European Conference and Exhibition of Optical Communication*, 2007, pp. 1–2.
[101] A. Melikyan *et al.*, "High-Speed Plasmonic Phase Modulators," *Nat. Photon.*, vol. 8, no. 3, pp. 229–233, Feb. 2014.
[102] Y. Ogiso *et al.*, "80-GHz Bandwidth and 1.5-V Vπ InP-Based IQ Modulator," *J. Lightwave Technol.*, vol. 38, no. 2, pp. 249–255, 2020.
[103] S. Ummethala *et al.*, "Capacitively Coupled Silicon-Organic Hybrid Modulator for 200 Gbit/s PAM-4 Signaling," in *Conference on Lasers and Electro-Optics*, 2019, p. JTh5B.2 (postdeadline).
[104] J. Golden, H. Miller, D. Nawrocki, and J. Ross, "Optimization of Bi-Layer Lift-off Resist Process," in *2009 International Conference on Compound Semiconductor Manufacturing Technology, CS MANTECH 2009*, 2009, no. January 2009.
[105] S. Krátký *et al.*, "Lift-off Technology for Thick Metallic Microstructures," in *METAL 2017 - 26th International Conference on Metallurgy and Materials, Conference Proceedings*, 2017, pp. 1298–1302.
[106] W. Jin *et al.*, "Benzocyclobutene Barrier Layer for Suppressing Conductance in Nonlinear Optical Devices during Electric Field Poling," *Appl. Phys. Lett.*, vol. 104, p. 2443304, 2014.
[107] S. K. Selvaraja *et al.*, "Highly Uniform and Low-Loss Passive Silicon Photonics Devices Using a 300mm CMOS Platform," in *Optical Fiber Communication Conference, OFC 2014*, 2014, p. Th2A.33.
[108] W. Bogaerts *et al.*, "Silicon-on-Insulator Spectral Filters Fabricated with CMOS Technology," *IEEE J. Sel. Top. Quantum Electron.*, vol. 16, no. 1, pp. 33–44, 2010.
[109] Ľ. Scholtz, P. Šutta, P. Calta, P. Novák, M. Solanská, and J. Müllerová, "Investigation of Barium Titanate Thin Films as Simple Antireflection Coatings for Solar Cells," *Appl. Surf. Sci.*, vol. 461, no. March, pp. 249–254, 2018.
[110] M. Cardona, "Optical Properties and Band Structure of SrTiO3 and BaTiO3," *Phys. Rev.*, vol. 140, no. 2A, pp. 651–655, 1965.
[111] J. Xu, J. Zhai, X. Yao, J. Xue, and Z. Huang, "Dielectric and Optical Properties of BaTiO3 Thin Films Prepared by Low-Temperature Process," *J. Sol-Gel Sci. Technol.*, vol. 42, no. 3, pp. 209–212, 2007.

[112] A. Karvounis, F. Timpu, V. V. Vogler-Neuling, R. Savo, and R. Grange, "Barium Titanate Nanostructures and Thin Films for Photonics," *Adv. Opt. Mater.*, vol. 8, no. 2001249, pp. 1–23, 2020.
[113] A. K. Sharma, B. G. Priyadarshini, B. R. Mehta, and D. Kumar, "An Amorphous Barium Titanate Thin Film Improves Light Trapping in Si Solar Cells," *RSC Adv.*, vol. 5, no. 74, pp. 59881–59886, 2015.
[114] P. I. Dietrich *et al.*, "In Situ 3D Nanoprinting of Free-Form Coupling Elements for Hybrid Photonic Integration," *Nat. Photon.*, vol. 12, no. 4, pp. 241–247, 2018.
[115] M. Billah *et al.*, "Hybrid Integration of Silicon Photonic Circuits and InP Lasers by Photonic Wire Bonding," *Optica*, vol. 5, no. 7, pp. 876–883, 2018.
[116] M. Blaicher *et al.*, "Hybrid Multi-Chip Assembly of Optical Communication Engines by in Situ 3D Nano-Lithography," *Light Sci. Appl.*, vol. 9, no. 71, 2020.
[117] H. Chung, W. S. C. Chang, and E. L. Adler, "Modeling and Optimization of Traveling-Wave LiNbO3 Interferometric Modulators," *IEEE J. Quantum Electron.*, vol. 27, no. 3, pp. 608–617, 1991.
[118] H. Yu and W. Bogaerts, "An Equivalent Circuit Model of the Traveling Wave Electrode for Carrier-Depletion-Based Silicon Optical Modulators," *J. Lightwave Technol.*, vol. 30, no. 11, pp. 1602–1609, 2012.
[119] F. Merget *et al.*, "Silicon Photonics Plasma-Modulators with Advanced Transmission Line Design," *Opt. Express*, vol. 21, no. 17, p. 19593, 2013.
[120] K. Kawano, T. Kitoh, H. Jumonji, T. Nozawa, and M. Yanagibashi, "New Travelling-Wave Electrode Mach-Zehnder Optical Modulator with 20 GHz Bandwidth and 4.7 V Driving Voltage at 1.52 Mm Wavelength," *Electron. Lett.*, vol. 25, no. 20, pp. 1382–1383, 1989.
[121] I. P. Kaminow, *An Introduction to Electrooptic Devices*. Academic Press, 1974.
[122] S. Y. Wang and S. H. Lin, "High Speed III-V Electro-Optic Waveguide Modulators at Lamda = 1.3 Mm," *J. Lightwave Technol.*, vol. 6, no. 6, 1988.
[123] S. H. Lin and S.-Y. Wang, "High-Throughput GaAs PIN Electrooptic Modulator with a 3-DB Bandwidth of 96 GHz at 1.3 Mm," *Appl. Opt.*, vol. 26, no. 9, p. 1696, 1987.
[124] R. G. Walker, "High-Speed III-V Semiconductor Intensity Modulators," *IEEE J. Quantum Electron.*, vol. 27, no. 3, pp. 654–667, 1991.
[125] S. S. Park, "Properties of BaTiO3 Films Sputter Deposited on PET for Pulse Power Capacitors," *Ferroelectrics*, vol. 457, no. 1, pp. 97–104,

2013.
[126] Z. Q. Shi, Q. X. Jia, and W. A. Anderson, “Electrical and Dielectric Properties of Thin Film BaTiO3 Capacitors Deposited by Radio Frequency Magnetron Sputtering,” *J. Vac. Sci. Technol. A Vacuum, Surfaces, Film.*, vol. 10, no. 4, pp. 733–736, 1992.
[127] W. T. Liu *et al.*, “Frequency Domain (1kHz-40GHz) Characterisation of Thin Films for Multichip Module Packaging Technology,” *Electron. Lett.*, vol. 30, no. 2, pp. 117–118, 1994.
[128] Q. X. Jia, Z. Q. Shi, and W. A. Anderson, “BaTiO3 Thin Film Capacitors Deposited by r.f. Magnetron Sputtering,” *Thin Solid Films*, vol. 209, pp. 230–239, 1991.
[129] Telecordia, “GR-468: Generic Reliability Assurance Requirements for Optoelectronic Devices Used in Telecommunications Equipment,” 2004.
[130] C. Kieninger *et al.*, “Demonstration of Long-Term Thermally Stable Silicon-Organic Hybrid Modulators at 85 °C,” *Opt. Express*, vol. 26, no. 21, p. 27955, 2018.
[131] Z. Shi *et al.*, “Tuning the Kinetics and Energetics of Diels-Alder Cycloaddition Reactions to Improve Poling Efficiency and Thermal Stability of High-Temperature Cross-Linked Electro-Optic Polymers,” *Chem. Mater.*, vol. 22, no. 19, pp. 5601–5608, 2010.
[132] U. Koch *et al.*, “A Monolithic Bipolar CMOS Electronic–Plasmonic High-Speed Transmitter,” *Nat. Electron.*, vol. 3, no. June, pp. 338–345, 2020.
[133] K. M. McPeak *et al.*, “Plasmonic Films Can Easily Be Better: Rules and Recipes,” *ACS Photonics*, vol. 2, no. 3, pp. 326–333, 2015.
[134] W. Jin *et al.*, “Structure-Function Relationship Exploration for Enhanced Thermal Stability and Electro-Optic Activity in Monolithic Organic NLO Chromophores,” *J. Mater. Chem. C*, vol. 4, no. 15, pp. 3119–3124, 2016.
[135] “Operating Manual: Millimeter-Submillimeter Power Meter, VDi Erickson PM4,” Virginia Diodes, 2010.
[136] A. Tessmann *et al.*, “High-Gain Submillimeter-Wave MHEMT Amplifier MMICs,” *IEEE MTT-S Int. Microw. Symp. Dig.*, pp. 53–56, 2010.
[137] R. Schmogrow *et al.*, “Error Vector Magnitude as a Performance Measure for Advanced Modulation Formats,” *IEEE Photonics Technol. Lett.*, vol. 24, no. 1, pp. 61–63, 2012.
[138] R. Schmogrow *et al.*, “Erratum: Corrections to Error Vector Magnitude as a Performance Measure for Advanced Modulation Formats (IEEE Photonics Technology Letters (2012) 24:1 (61-63)),” *IEEE Photonics Technol. Lett.*, vol. 24, no. 23, p. 2198, 2012.

[139] W. Freude *et al.*, "Quality Metrics for Optical Signals: Eye Diagram, Q-Factor, OSNR, EVM and BER," in *14th International Conference on Transparent Optical Networks*, 2012, p. Mo.B1.5.
[140] T. Pfau, S. Hoffmann, and R. Noe, "Hardware-Efficient Coherent Digital Receiver Concept With Feedforward Carrier Recovery for M-QAM Constellations," *J. Lightwave Technol.*, vol. 27, no. 8, pp. 989–999, 2009.
[141] R. Ding *et al.*, "High-Speed Silicon Modulator with Slow-Wave Electrodes and Fully Independent Differential Drive," *J. Lightwave Technol.*, vol. 32, no. 12, pp. 2240–2247, 2014.
[142] M. Burla *et al.*, "500 GHz Plasmonic Mach-Zehnder Modulator Enabling Sub-THz Microwave Photonics," *Prepr. arXiv1901.00477*, 2018.
[143] Y. Ding, H. Ou, and C. Peucheret, "Ultrahigh-Efficiency Apodized Grating Coupler Using Fully Etched Photonic Crystals," *Opt. Lett.*, vol. 38, no. 15, p. 2732, 2013.
[144] D. Benedikovic *et al.*, "Subwavelength Index Engineered Surface Grating Coupler with Sub-Decibel Efficiency for 220-Nm Silicon-on-Insulator Waveguides," *Opt. Express*, vol. 23, no. 17, p. 22628, 2015.
[145] H. J. Song, K. Ajito, Y. Muramoto, A. Wakatsuki, T. Nagatsuma, and N. Kukutsu, "Uni-Travelling-Carrier Photodiode Module Generating 300 GHz Power Greater than 1 MW," *IEEE Microw. Wirel. Components Lett.*, vol. 22, no. 7, pp. 363–365, 2012.
[146] H. J. Song, "Packages for Terahertz Electronics," *Proc. IEEE*, vol. 105, no. 6, pp. 1121–1138, 2017.
[147] Y. Salamin *et al.*, "Microwave Plasmonic Mixer in a Transparent Fibre–Wireless Link," *Nat. Photon.*, vol. 12, no. 12, pp. 749–753, 2018.
[148] T. Harter *et al.*, "Silicon-Plasmonic Integrated Circuits for Terahertz Signal Generation and Coherent Detection," *Nat. Photon.*, vol. 12, no. 10, pp. 625–633, 2018.
[149] G. G. Raju, *Dielectrics in Electric Fields*. CRC Press, 2017.
[150] V. A. Shvets, V. N. Kruchinin, and V. A. Gritsenko, "Dispersion of the Refractive Index in High-k Dielectrics," *Opt. Spectrosc.*, vol. 123, no. 5, pp. 728–732, 2017.
[151] M. Wöhlecke, V. Marrello, and A. Onton, "Refractive Index of BaTiO3and SrTiO3films," *J. Appl. Phys.*, vol. 48, no. 4, pp. 1748–1750, 1977.
[152] S. Gevorgian, *Ferroelectrics in Microwave Devices, Circuits and Systems*. Springer, 2009.
[153] A. Davidson, K. Jones, and E. Strid, "LRM and LRRM Calibrations with Automatic Determination of Load Inductance," in *36th ARFTG*

conference digest., 1190, vol. 18.
[154] E. Lourandakis, *On-Wafer Microwave Measurements and de-Embedding*. Artech House, 2016.
[155] G. E. Ponchak and A. N. Downey, "Characterization of Thin Film Microstrip Lines on Polyimide," *IEEE Trans. Components Packag. Manuf. Technol. Part B*, vol. 21, no. 2, pp. 171–176, 1998.
[156] J. Judek, A. P. Gertych, M. Swiniarski, M. Zdrojek, J. Krupka, and J. K. Piotrowski, "Characterization of Finite-Width Ground Coplanar Waveguides on High Resistivity Silicon with Ultralow Metallization Thickness," *IEEE Trans. Microw. Theory Tech.*, vol. 65, no. 12, pp. 4836–4842, 2017.
[157] E. Hammerstad and O. Jensen, "Accurate Models for Microstrip Computer-Aided Design," in *1980 IEEE MTT-S International Microwave Symposium Digest. IEEE*, 1980, pp. 407–409.
[158] M. P. McNeal, S. J. Jang, and R. E. Newnham, "The Effect of Grain and Particle Size on the Microwave Properties of Barium Titanate (BaTiO3)," *J. Appl. Phys.*, vol. 83, no. 6, pp. 3288–3297, 1998.
[159] M. Adamov, B. Perović, and T. Nenadović, "Electrical and Structural Properties of Thin Gold Films Obtained by Vacuum Evaporation and Sputtering," *Thin Solid Films*, vol. 24, pp. 89–100, 1974.
[160] C. Koos, *Nanophotonic Devices for Linear and Nonlinear Optical Signal Processing*. Univ.-Verl. Karlsruhe, 2007, 2007.

E Glossary

E.1 List of abbreviations

16QAM	16-state quadrature amplitude modulation
4QAM	4-state quadrature amplitude modulation
64QAM	64-state quadrature amplitude modulation
ADC	Analog-to-digital converters
ASE	Amplified spontaneous emission
Au	Gold
AWG	Arbitrary-waveform generator
AWGN	Additive white Gaussian noise
BB	Baseband
Bd	Baudrate
BER	Bit error ratio
BOX	Buried silicon dioxide
BPF	Band-pass filter
BTO	Barium titanate, $BaTiO_3$
CC-SOH	Capacitively-coupled silicon-organic hybrid
CMOS	Complementary metal-oxide semiconductor
CMT	Conformal mapping technique
CPD	Critical point dryer
CPW	Coplanar waveguide

Cr	Chromium
CW	Continuous-wave
DI	De-ionized
DSP	Digital signal processing
e-beam	Electron beam
ECL	External-cavity laser
EDFA	Erbium-doped fiber amplifier
EO	Electro-optic
EVM	Error vector magnitude
FEC	Forward error correction
FEGC	Fully etched grating coupler
FoM	Figure-of-merit
FSPL	Free-space path loss
FTTA	Fiber-to-the-antenna
GC	Grating coupler
GSG	Ground-signal-ground
HD-FEC	Hard-decision forward error correction
HF	Hydrofluoric
HS-POH	Horizontal-slot plasmonic-organic hybrid
HSQ	Hydrogen silsesquioxane
ICP-RIE	Inductively coupled plasma – reactive ion etching
IMT	Institute of Microstructure Technology
InP	Indium phosphide

IoT	Internet of things
IQ	In-phase and quadrature-phase
ISO	Isopropanol
KIT	Karlsruhe Institute of Technology
KNMF	Karlsruhe Nano Micro Facility
LNA	H-band low-noise amplifier
LO	Local oscillator
mHEMT	metamorphic high-electron-mobility transistor
MIBK	Methyl isobutyl ketone
MIM	Metal-insulator-metal
MMI	Multi-mode interference
MMIC	Millimeter-wave monolithic integrated circuits
MPA	H-band medium-power amplifier
MZM	Mach-Zehnder modulator
NMP	N-methyl-2-pyrrolidone
O/T	Optical-to-terahertz
OMA	Optical modulation analyzer
OOK	On-off keying
Opt. Rx	Optical receiver
Opt. Tx	Optical transmitter
PAM2	Pulse amplitude modulation
PAM4	4-state pulse-amplitude modulation
PC	Polarization controller

PEC	Proximity effect correction
PEGC	Partially etched grating couplers
PIC	Photonic integrated circuits
PMMA	Poly-methyl methacrylate
POH	Plasmonic-organic hybrid
PTFE	Polytetrafluoroethylene
QAM	Quadrature amplitude modulation
QPSK	Quadrature phase shift keying
RC-SOH	Resistively-coupled silicon-organic hybrid
RF	Radio frequency/microwave
Rx	Receiver
SD-FEC	Soft-decision forward error correction
SEM	Scanning electron microscope
Si WG	Silicon waveguide
Si	Silicon
SiP	Silicon photonic
SNR	Signal-to-noise power ratio
SOH	Silicon-organic hybrid
SOI	Silicon-on-insulator
SPP	Surface plasmon polaritons
T/O	Terahertz-to-optical
TE	Transverse electric
TEM	Transverse-electric

THz	Terahertz
Ti	Titanium
TM	Transverse magnetic
TMAH	Tetra-methyl ammonium hydroxide
ToF	Terahertz-over fiber
TRx	Transceiver
Tx	Transmitter
UTC-PD	Uni-travelling-carrier photodiode
VNA	Vector network analyzer
VOA	Variable optical attenuator
VS-POH	Vertical-slot plasmonic-organic hybrid

E.2 List of mathematical symbols

Greek symbols

α	Amplitude loss parameter
β	Propagation constant
γ	Complex propagation constant
Γ	Field interaction factor
δ	Impulse function
ε_0	Vacuum permittivity
ε_r	Relative dielectric permittivity
$\varepsilon_{\mathrm{r,ij}}$	Relative dielectric permittivity tensor
$\Delta\varepsilon_\mathrm{r}$	Change of the relative permittivity
η	Phase modulation index

λ	Wavelength
μ_0	Vacuum permeability
ρ	Reflection coefficient
φ	Phase shift of a signal
ϕ_b	Bias phase
$\underline{\chi}^{(n)}$	Influence function of order n
$\underline{\tilde{\chi}}^{(n)}$	Electric susceptibility of order n
ω	Angular frequency

Latin symbols

a	Attenuation in dB
A_slot	Cross-sectional area of the slot waveguide
$\underline{b}_k$	Complex symbol for data transmission
$b_\mathrm{k,I}$	Real part of a symbol
$b_\mathrm{k,Q}$	Complex part of a symbol
B	Signal bandwidth
c, c_0	Vacuum speed of light
C'	Differential capacitance
d	Distance between the plasmonic rails
$\vec{E}$	Electrical field vector
$\vec{\mathcal{E}}$	Transversal electric mode field
f	Frequency
G'	Differential conductance
h	Height
$i(t)$	Time dependent current
$\vec{\mathcal{H}}$	Transversal magnetic mode field
I	Optical intensity

J_n	n^{th} Bessel function of the first kind
k_0	Vacuum wavenumber
K	Complete elliptical integral of the first kind
L	Length
L'	Differential inductance
$m(\omega_m)$	EO frequency response
n	Real part of the refractive index
n_i	Imaginary part of the refractive index
n_e	Effective refractive index
n_g	Group refractive index
n_D	Doping concentration of donor ions
Δn	Change in the real part of the refractive index
N_0	Power spectral density of amplified spontaneous emission
P	Power
$\vec{P}$	Electric polarization
q_i	Dielectric fill factor
r	Plasmonic rail width
r_{33}	Electro-optic coefficient
R_s	Symbol rate
$R_{1,0}$	Sideband-to-carrier power ratio
S_{ij}	Two-port scattering parameters
r_{ijk}	Electro-optic coefficient, the indices i,j,k denote the Cartesian components
R'	Differential resistance
t	Time
$\Delta t_{o,m}$	Temporal walk-off between optical and modulating signal

T	Transfer function
T_g	Glass transition temperature
$u(t)$	Time dependent voltage
U	Modulating/driving voltage
U_{pol}	Poling voltage
U_π	π-voltage
v_{g}	Group velocity
w	Width
Z	Characteristic impedance
Z_0	Impedance of free space

Acknowledgements

The doctoral work presented in this thesis would not have been possible without the support from many souls. Foremost, I extend my gratitude to Prof. Christian Koos for giving me an opportunity to work in this exciting field of research. I am grateful to him for his constant support all through the difficult times and the belief he entrusted in me in reaching the goals of the thesis. My deepest gratitude also goes to Prof. Wolfgang Freude for his invaluable teachings, attention to the details and the long hours spent together juggling through the manuscripts in the company of delicious 'Lindt' chocolates. I express my thanks also to Prof. Sebastian Randel for his comments on improving the quality of my manuscripts and for his help in the post-processing of data transmission experiments. Special thanks to Prof. Thomas Zwick, without whose support it would have been impossible to perform high-frequency measurements. I also appreciate his time for studying this work and for agreeing to co-refer my dissertation.

I would like to thank my co-workers and friends at the Institute of Photonics and Quantum Electronics (IPQ) as well as the Institute of Microstructure Technology (IMT) for their active and passive contribution to the work and the pleasant work environment. A special thanks to my longest office-mates – Daria Kohler, Sascha Mühlbrandt, Tobias Harter, Sentayahu Wondimu and Kira Köhnle for the liveliest workspace. I will cherish the pranks on one another and the many memorable moments in the years to come. I would also like to thank Matthias Lauermann, Simon Schneider, Claudius Weimann, Argishti Melikyan, Robert Palmer, Nicole Lindenmann, Philipp Schindler, Stefan Wolf, Salek Mahmud, Pascal Maier, Pablo Marin, Muhammad Billah, Matthias Blaicher, Philipp Dietrich, Carsten Eschenbaum, Dengyang Fang, Christoph Füllner, Denis Ganin, Tilahun Gutema, Wladislaw Hartmann, Tobias Hoose, Adib Hossain, Juned Kemal, Alexander Kotz, Yasar Kutuvantavida, Johannes Milvich, Aleksandar Nesic, Jörg Pfeifle, Norbert Schneider, Stefan Singer, Mareike Trappen, Philipp Trocha, Yilin Xu, Clemens Kieninger, Heiner Zwickel, Artem Kuzmin, and Alban Sherifaj for the great time that was spent together. A special thanks to Tobias and Mariann for their help with the German translation of the 'preface' of this thesis into a well-written 'Zusammenfassung'.

Many thanks also to Florian Rupp, Oswald Speck, David Guder, Steffen Herzog, Marco Hummel, Lisa Nolte, Steffen Pfeifer, Volker Bös, and Martin Winkeler for all the help behind-the-scenes. I would also thank Bernadette Lehmann, Tatiana Gassmann, Maria-Luise Koch, and Andrea Riemensperger for the administrative help and their great enthusiasm in organizing the fun trips.

Special to the E-beam team at IMT − Dr. Lothar Hahn, Andreas Bacher, Marie-Kristin Nees, Anja Eberhardt for the immense help that I received in processing my chips. I also express my thanks to the whole cleanroom team at IMT without whose help in maintaining the facilities, this work would not have been possible. Many thanks to Sanaz Rastjoo, Randy Fechner and Heike Fornasier for the many impromptu HF-dips that they accommodated.

Many thanks also to Jochen Schäfer for the help with the vector network analyser measurements. I would like to thank all the students I had the opportunity to supervise and to collaborate with in the last years – Fernando Negredo, Tobias Harter, Zheng Li, Anirudh Pammi, Ahmed Shariful Alam, Ahsan Uddin and Furkan Sahin.

I express my heartfelt thanks to all my friends – Sivaram Kannepalli, Harsha Nandam, Nivesh Mangal, Suresh Garlapati, Jhony Rusumdar and many others in Karlsruhe for constantly being by my side in both good and bad times. A special thanks to Suresh and Harsha whose contribution in my work resulted in turning our friendship into a fruitful collaboration. I would like to take this opportunity to thank Prof. Srinivas Talabattula, Prof. Murugesan Venkatapathi and Prof. Wolfram Pernice who nurtured my interests in field of optics and photonics.

Last but not the least; no words could express my gratitude to my parents (Raghavendra Rao & Sandhya), my brother (Dr. Raghunandan) and my sister-in-law (Dr. Suneetha). Without their unconditional love and constant support, I could not have been what I am today. I feel very fortunate to have found the love of my life and my lovely wife, Pooja during my PhD. She has been a constant motivation and deserves a lion’s share in this outcome. I cannot thank her enough for her patience, understanding and for always being by my side all through the rough times.

List of publications

Journal publications

[J1] **Ummethala**, **S.,** Kemal, J. N., Alam, A. S., Lauermann, M., Kutuavantavida, Y., Nandam, S. H., Hahn, L., Elder, D. L., Dalton, L. R., Zwick, T., Randel, S., Freude, W., Koos, C., "Hybrid Electro-Optic Modulator Combining Silicon Photonic Slot Waveguides with High-k Radio-Frequency Slotlines", *Optica*, **8**, 511–519 (2021)

[J2] Harter, T.; Füllner, C.; Kemal, J. N.; **Ummethala, S.**; Steinmann, J. L.; Brosi, J.-M.; Hesler, J. L.; Bruendermann, E.; Mueller, M.; Freude, W.; Randel, S.; Koos, C., "Generalized Kramers-Kronig Receiver for Coherent Terahertz Communications", *Nature Photonics* **14**, 601–606 (2020)

[J3] **Ummethala, S.**; Harter, T.; Koehnle, K.; Li, Z.; Muehlbrandt, S.; Kutuvantavida, Y.; Kemal, J. N.; Marin-Palomo, P.; Schaefer, J.; Tessmann, A.; Garlapati, S. K.; Bacher, A.; Hahn, L.; Walther, M.; Zwick, T.; Randel, S.; Freude, W.; Koos, C., "THz-to-optical conversion in wireless communications using an ultra-broadband plasmonic modulator", *Nature Photonics* **13**, 519–524 (2019)

[J4] Harter, T.; **Ummethala, S.**; Blaicher, M.; Muehlbrandt, S.; Wolf, S.; Weber, M.; Adib, M. M. H.; Kemal, J. N.; Merboldt, M.; Boes, F.; Nellen, S.; Tessmann, A.; Walther, M.; Globisch, B.; Zwick, T.; Freude, W.; Randel, S.; Koos, C., "Wireless THz link with optoelectronic transmitter and receiver", *Optica* **6**, 1063–1070 (2019)

[J5] Harter, T.; Muehlbrandt, S.; **Ummethala, S**.; Schmid, A.; Nellen, S.; Hahn, L.; Freude, W.; Koos, C., "Silicon–plasmonic integrated circuits for terahertz signal generation and coherent detection", *Nature Photonics* **12**, 625–633 (2018)

[J6] Koos, C.; Leuthold, J.; Freude, W.; Kohl, M.; Dalton, L. R.; Bogaerts, W.; Giesecke, A. L.; Lauermann, M.; Melikyan, A.; Koeber, S.; Wolf, S.; Weimann, C.; Muehlbrandt, S.; Koehnle, K.; Pfeifle, J.; Hartmann, W.; Kutuvantavida, Y.; **Ummethala, S.**; Palmer, R.; Korn, D.; Alloatti, L.; Schindler, P. C.; Elder, D. L.; Wahlbrink, T.; Bolten, J., "Silicon-Organic Hybrid (SOH) and Plasmonic-Organic Hybrid (POH) Integration", *J. Lightwave Technol.* **34**, 01–13 (2016)

Conference publications

[C1] **Ummethala, S.**; Pammi, Venkata A.; Uddin, Ahsan H. M.; Hahn, L.; Freude, W.; Koos, C., "Horizontal-Slot Plasmonic-Organic Hybrid (POH) Modulator", *Conf. on Lasers and Electro-Optics (CLEO'20), Virtual Confenerence, May 11–15* , paper SM2J.4 *Optical Society of America* (2020)

[C2] Harter, T.; Füllner, C.; Kemal, J. N.; **Ummethala, S.**; Steinmann, J. L.; Brosi, J.-M.; Hesler, J. L.; Bründermann, E.; Freude, W.; Randel, S.; Koos, C., "Generalized Kramers-Kronig Receiver for 16QAM Wireless THz Transmission at 110 Gbit/s", *45th European Conference on Optical Communication (ECOC'19), Dublin, Ireland, September 22-26* , paper Th.2.C.4 (2019)

[C3] Freude, W.; **Ummethala, S.**; Harter, T.; Koehnle, K.; Li, Z.; Muehlbrandt, S.; Kutuvantavida, Y.; Kemal, J. N.; Marin-Palomo, P.; Schaefer, J.; Tessmann, A.; Kumar Garlapati, S.; Bacher, A.; Hahn, L.; Walther, M.; Zwick, T.; Randel, S.; Koos, C., "Wireless THz-to-optical conversion with an electro-optic plasmonic modulator", *Light: Science & Applications, Light Conference (Light Conference'19), Changchun, China, July 16-18* (2019) (invited)

[C4] Freude, W.; Harter, T.; Muehlbrandt, S.; **Ummethala, S.**; Nellen, S.; Hahn, L.; Randel, S.; Koos, C., "Silicon photonics for coherent terahertz generation and detection", *21th Intern. Conf. on Transparent Optical Networks (ICTON'19), Angers, France, July 9-13* (2019) (invited)

[C5] Freude, W.; Harter, T.; **Ummethala, S.**; Muehlbrandt, S.; Blaicher, M.; Wolf, S.; Weber, M.; Boes, F.; Massler, H.; Tessmann, A.; Kutuvantavida, Y.; Kemal, J. N.; Nellen, S.; Hahn, L.; Globisch, B.; Walther, M.; Zwick, T.; Randel, S.; Koos, C., "Wireless terahertz communications", *Conf. on Lasers and Electro-Optics (CLEO/Europe-EQEC 2019), Munich, Germany, June 23-27* (2019)

[C6] **Ummethala, S.**; Kemal, J. N.; Lauermann, M.; Alam, A. S.; Zwickel, H.; Harter, T.; Kutuvantavida, Y.; Hahn, L.; Nandam, S. H.; Elder, D. L.; Dalton, L. R.; Freude, W.; Randel, S.; Koos, C., "Capacitively Coupled Silicon-Organic Hybrid Modulator for 200 Gbit/s PAM-4 Signaling", *Conf. on Lasers and Electro-Optics (CLEO'19), San Jose (CA), USA, May 5–10* , paper JTh5B.2 *Optical Society of America* (2019) (postdeadline)

[C7] Freude, W.; Harter, T.; **Ummethala, S.**; Muehlbrandt, S.; Blaicher, M.; Wolf, S.; Weber, M.; Boes, F.; Massler, H.; Tessmann, A.; Kutuvantavida, Y.; Kemal, J. N.; Nellen, S.; Hahn, L.; Goebel, T.; Walther, M.; Zwick, T.; Randel, S.; Koos, C., "Terahertz communications meets photonics", *14th Intern. Conf. on Fiber Optics & Photonics (Photonics'18), Indian Institute of Technology Delhi (IIT Delhi), Delhi, India, December 12–15* (2018) (invited)

[C8] **Ummethala, S.**; Harter, T.; Koehnle, K.; Li, Z.; Muehlbrandt, S.; Kutuvantavida, Y.; Kemal, J. N.; Schaefer, J.; Massler, H.; Tessmann, A.; Kumar Garlapati, S.; Bacher, A.; Hahn, L.; Walther, M.; Zwick, T.; Randel, S.; Freude, W.; Koos, C., "Wireless Transmission at 0.3 THz Using Direct THz-to-Optical Conversion at the Receiver", *44th European Conference on Optical Communication (ECOC'18), Rome, Italy, September 23-27* , paper We4H.3 (2018) (invited)

[C9] Harter, T.; Füllner, C.; Kemal, J. N.; **Ummethala, S.**; Brosi, J.-M.; Bründermann, E.; Freude, W.; Randel, S.; Koos, C., "110-m THz Wireless Transmission at 100 Gbit/s Using a Kramers-Kronig Schottky Barrier Diode Receiver", *44th European Conference on Optical Communication (ECOC'18), Rome, Italy, September 23-27* , paper Th3F.7 (2018) (postdeadline)

[C10] Harter, T.; **Ummethala, S.**; Muehlbrandt, S.; Blaicher, M.; Koehnle, K.; Adib, M. M. H.; Weber, M.; Wolf, S.; Kutuvantavida, Y.; Kemal, J. N.; Nellen, S.; Hahn, L.; Tessmann, A.; Walther, M.; Zwick, T.; Randel, S.; Freude, W.; Koos, C., "Wireless terahertz communications using optoelectronic techniques", *Progress in Electromagnetics Research Symposium 2018 (PIERS 2018), Toyama, Japan, August 1-4* (2018) (invited)

[C11] Koos, C.; Randel, S.; Freude, W.; Dalton, L. R.; Wolf, S.; Kieninger, C.; Kutuvantavida, Y.; Lauermann, M.; Elder, D. L.; Muehlbrandt, S.; Zwickel, H.; Melikyan, A.; Harter, T.; **Ummethala, S.**; Billah, M. R.; Blaicher, M.; Dietrich, P.-I.; Hoose, T., "Hybrid Photonic Integration and Plasmonic Devices: New Perspectives for High-Speed Communications and Ultra-Fast Signal Processing", *Pacific Rim Conference on Lasers and Electro-Optics (CLEO-PR 2018), Hong Kong, July 29 – August 3* (2018) (invited)

[C12] Freude, W.; Harter, T.; **Ummethala, S.**; Muehlbrandt, S.; Blaicher, M.; Wolf, S.; Weber, M.; Boes, F.; Massler, H.; Tessmann, A.; Kutuvantavida, Y.; Kemal, J. N.; Nellen, S.; Hahn, L.; Goebel, T.; Walther, M.; Zwick, T.; Randel, S.; Koos, C., "Wireless THz communications using optoelectronic techniques", *Light: Science & Applications, Light Conference (Light Conference'18), Changchun, China, July 16-18* (2018) (invited)

[C13] **Ummethala, S.**; Harter, T.; Koehnle, K.; Muehlbrandt, S.; Kutuvantavida, Y.; Kemal, J. N.; Schaefer, J.; Massler, H.; Tessmann, A.; Kumar Garlapati, S.; Bacher, A.; Hahn, L.; Walther, M.; Zwick, T.; Randel, S.; Freude, W.; Koos, C., "Terahertz-to-Optical Conversion Using a Plasmonic Modulator", *Conf. on Lasers and Electro-Optics (CLEO'18), San Jose (CA), USA, May 13–18* , paper STu3D.4 (2018)

[C14] Harter, T.; Muehlbrandt, S.; **Ummethala, S.**; Schmid, A.; Bacher, A.; Hahn, L.; Kohl, M.; Freude, W.; Koos, C., "Silicon-Plasmonic Photomixer for Generation and Homodyne Reception of Continuous-Wave THz Radiation", *Conf. on Lasers and Electro-Optics (CLEO'16), San Jose (CA), USA, June 5 – 10* , paper SM4E.5. (2016)